Investigation of Semiconductor Opening Switch for Pulsed Power Applications with Output Voltage of up to 500 kV

Mawuena Degnon

THÈSE

Présentée à

L'Université de Pau et des Pays de l'Adour

École Doctorale des Sciences Exactes et de leurs Applications – ED SEA 211

Laboratoire des Sciences pour l'Ingénieur Appliquées à la Mécanique et au génie Électrique – SIAME

Par

Mawuena Rémi DEGNON

Pour obtenir le grade de

DOCTEUR

Spécialité : Génie Électrique

INVESTIGATION OF OFF-THE-SHELF DIODES AS HIGH-VOLTAGE OPENING SWITCH FOR PULSED POWER APPLICATIONS WITH OUTPUT VOLTAGE OF UP TO 500 KV

Soutenue le 24 mai 2024

Devant le jury composé de :

Président :	P. E. VIDAL	Professeur – Université de Technologie Tarbes Occitanie Pyrénées
Rapporteurs :	G. MÜLLER	Professeur – Karlsruhe Institute of Technology
	H. PIQUET	Professeur – Université de Toulouse
Examinateurs :	F. BAYOL	Directeur Technique – ITOPP
	E. MEISSNER	Directrice de Recherche – Fraunhofer IISB
	B. M. NOVAC	Professeur – Loughborough University
Directeurs de thèse :	A . GUSEV	Enseignant-Chercheur – Université de Pau et des Pays de l'Adour
	L. PECASTAING	Professeur – Université de Pau et des Pays de l'Adour
Membre invité :	C. DUCHESNE	Directeur Général – DEEP CONCEPT

Remerciements

Cette thèse a été réalisée à l'Université de Pau et des Pays de l'Adour (UPPA), dans le cadre d'une convention CIFRE, mise en œuvre par l'Association Nationale de la Recherche et de la Technologie (ANRT), et établie entre la société ITOPP et le laboratoire SIAME de l'UPPA.

Je tiens à remercier Messieurs Gauthier DEMOL et Stéphane CHEZE qui se sont succédé à la présidence de la société ITOPP, ainsi que Monsieur Sébastien BOISNE, Directeur de BETA BEAMS, pour la confiance qu'ils m'ont accordée en la réalisation de ce projet de thèse.

Je suis très honoré par le soutien de Laurent PECASTAING, Professeur à l'UPPA et Directeur du Laboratoire SIAME, qui m'a accueilli et m'a donné les moyens nécessaires pour accomplir ce travail, pour ses conseils et pour son implication dans la direction de cette thèse. Qu'il trouve ici l'expression de ma sincère reconnaissance.

Je ne remercierai jamais assez Anton GUSEV, Enseignant-Chercheur au SIAME, pour la qualité de son encadrement, son énorme investissement, sa disponibilité et ses encouragements pendant ces trois années. Qu'il trouve ici la marque de ma plus profonde reconnaissance.

J'adresse mes sincères remerciements à Monsieur Georg MÜLLER, Professeur au Karlsruhe Institute of Technology, et Monsieur Hubert PIQUET, Professeur à l'Université de Toulouse, pour avoir accepté d'être les rapporteurs scientifiques de ce travail et pour m'avoir autorisé à soutenir cette thèse.

Je suis très sensible à l'honneur que m'a fait Monsieur Paul-Etienne VIDAL, Professeur à l'Université de Technologie Tarbes Occitanie Pyrénées, en acceptant de présider ma soutenance de thèse.

J'adresse mes plus vifs remerciements à Bucur Mircea NOVAC, Professeur à Loughborough University, pour l'intérêt manifeste qu'il a porté à mes travaux de recherche tout au long de ces trois années, pour son partage d'expérience et pour avoir accepté de faire partie de mon jury de thèse. J'exprime également ma gratitude à Frédéric BAYOL, Directeur technique d'ITOPP, pour ses relectures et pour avoir accepté de faire partie de mon jury de thèse.

J'associe mes sincères remerciements à Madame Elke MEISSNER, Directrice de recherche à Fraunhofer Institute for Integrated Systems and Device Technology IISB, et à Monsieur Cyril DUCHESNE, Directeur général de DEEP CONCEPT, pour avoir accepté d'évaluer cette thèse et pour leurs remarques constructives qui ont grandement enrichi ce travail.

Remerciement

Mes remerciements vont à l'endroit de mes proches, amis et toutes celles et ceux qui m'ont fait l'honneur d'assister à ma soutenance, particulièrement à Messieurs Efoevi Angelo KOUDOU et Cyril SAINT-CRICQ.

Mes chaleureux remerciements vont également à mes collègues et amis du laboratoire SIAME pour leur soutien quotidien, nos discussions passionnantes et leur bonne humeur. Je pense notamment à la superbe équipe PHT, à ses membres de droit et de cœur dont l'amitié et la collaboration ont été inestimables : Estelle, Laurent P., Marc, Thierry, Antoine, Veronika, Robert, Jean-Marc, Anton, Ejlal, Njomza, Roman, Abdellatif, Laurent A., Alexandre, Éric, Steven, Jean-Marie, Nicolas C., Charly, Thomas, Ivan, Alexey, Sylvain, Viviane, Robin, Natacha, Guillaume, Nelly ; mais aussi à mes stagiaires Menad, Nicolas G., Yann, qui m'ont apporté une aide précieuse.

Je tiens à remercier tous mes collègues et amis, passés et présents, d'ITOPP, pour l'accueil chaleureux qu'ils m'ont réservé lors de mes multiples visites à Thégra et avec qui j'ai eu de nombreux échanges enrichissants. Une pensée particulière à Camille, Gaëtan, Yoan, Tony, Philippe K., Frédérique J., Baptiste G., Rémi T., Marius, Aleksandr, Simon, Patrice, Olivier.

Enfin, je remercie ma famille et mes amis, trop nombreux pour les citer, pour leur soutien inconditionnel, leur patience et leur compréhension durant ces années de travail intensif. À mes parents, Dovi et Yao, à mon frère Joël et ma sœur Laura, à tonton Émile et à Irène, ma très chère et tendre, pour leur amour et leur encouragement constant. Vous avez été ma source de force et de motivation.

*Pour avoir contribué, de près ou de loin, à la réalisation de cette thèse, je vous dis à tous, Merci, Thank you, "**Akpe**".*

À ceux qui nous sont chers,
Qui nous ont, hélas, quittés trop tôt,
Et à ceux qui nous donnent la force de continuer.

Résumé

Cette thèse se propose de répondre aux besoins croissants en systèmes de génération de haute tension impulsionnelle, fiables, répétitifs et durables, pour des applications industrielles telles que la stérilisation par faisceaux d'électrons. Pour ces applications, des impulsions hautes tensions rapides d'une durée de quelques dizaines de nanosecondes sont nécessaires. Ces impulsions peuvent être générées par des systèmes de Hautes Puissances Pulsées (HPP) basés sur un stockage d'énergie inductive (*IES – Inductive Energy Storage*), qui offre une forte densité d'énergie comparé au stockage capacitif. Cependant, l'implémentation du stockage inductif nécessite l'utilisation de commutateurs capables d'interrompre des courants de l'ordre du kiloampère, de supporter des tensions de plusieurs centaines de kilovolts et de fonctionner à des fréquences de répétition de plusieurs dizaines de Hertz.

La diode SOS (*Semiconductor Opening Switch*– commutateur semi-conducteur à ouverture) se présente comme le choix optimal pour les générateurs HPP basés sur le stockage inductif, grâce à sa capacité à commuter de manière répétitive des densités de courant supérieures à 1 kA/cm^2 et des puissances instantanées de plusieurs gigawatts, tout en assurant un fonctionnement fiable et durable. Cependant, l'accès aux diodes SOS est limité en raison du nombre restreint de fabricants, résultant de la faible demande de ce composant et de ses spécificités de fabrications. Pour pallier cette difficulté, cette recherche se concentre sur l'étude de diodes de puissance disponibles dans le commerce (OTS – Off-The-Shelf), capables de commuter rapidement des courants inverses importants et de générer des impulsions hautes tensions de plusieurs centaines de kilovolts en quelques nanosecondes.

Le manuscrit est organisé en quatre chapitres, comprenant une revue de la littérature et trois autres basés sur des articles publiés dans le cadre de cette thèse.

Le **Chapitre 1** présente une revue exhaustive de la littérature sur la commutation état solide à ouverture dans les systèmes de HPP. Il introduit les principes fondamentaux de la technologie des HPP et situe l'étude dans son contexte. L'état de l'art des différents commutateurs état solide à ouverture dans les générateurs impulsionnels aborde à la fois les composants semi-conducteurs contrôlés (Thyristors, IGBT, MOSFET) et non contrôlés comme la diode SOS. La structure de ces composants, leurs principes de fonctionnement ainsi que leurs paramètres et caractéristiques de courant, tension et puissance sont présentés et comparés, mettant en évidence que la technologie des diodes SOS est particulièrement adaptée pour l'objectif visé. Les propriétés spécifiques des diodes SOS sont décrites, notamment leur capacité à distribuer automatiquement la tension sur l'ensemble des diodes élémentaires dans un empilement, assurant ainsi une commutation rapide et fiable. Le chapitre met également en lumière quelques-unes des nombreuses applications industrielles des générateurs SOS. Il explore différentes architectures de circuits de générateurs SOS, telles que celles basées

sur des générateurs de Marx, des générateurs spirales, la compression magnétique et les transformateurs impulsionnels, en présentant leurs avantages et inconvénients respectifs. En outre, une approche spécifique de conception d'un circuit de générateur SOS basé sur un élément magnétique unique, à savoir le transformateur impulsionnel saturable, est détaillée. Le choix de ce circuit est motivé par son efficacité énergétique élevée, pouvant atteindre 70%. L'approche inclut le dimensionnement des différents composants des circuits primaire et secondaire, ainsi que du transformateur impulsionnel saturable. Elle décrit également les propriétés du noyau magnétique nécessaires pour un fonctionnement optimal et une efficacité énergétique maximale du générateur.

Dans le **Chapitre 2** de cette thèse, l'accent est mis sur l'étude des diodes disponibles dans le commerce (ou OTS) en tant qu'interrupteurs haute tension à ouverture. Cette étude analyse le fonctionnement de ces diodes sur des bancs d'essais spécifiquement développés en suivant la méthodologie établie au Chapitre 1. Les détails de ces développements sont précisés dans le Chapitre 3. Les bancs d'essais utilisés comprennent des systèmes de basse et moyenne énergie, respectivement 25 mJ et 10 J, sur lesquels plus de 25 types de diodes OTS sont testés en comparaison avec des diodes SOS dans une configuration expérimentale identique. Le choix des diodes est basé sur des paramètres typiques extraits de leurs fiches techniques, tels que le courant direct (∼0,2–1 kA), la tension inverse maximale (∼0,2–10 kV) et la durée de recouvrement (∼0,1–20 µs). En se basant sur ces critères, différentes catégories de diodes, incluant les diodes de redressement, à avalanche, à recouvrement rapide et de suppression de tension transitoire (*TVS – Transient Voltage Suppression*), sont sélectionnées et évaluées en mode SOS sur le banc d'énergie de 25 mJ. Sur une charge résistive de 30 Ω, des impulsions de tension d'amplitude 1,8–2,5 kV et de temps de montée 13–27 ns sont obtenues. Les diodes TVS se distinguent particulièrement en démontrant des performances de temps de commutation optimales. La tension nominale relativement basse des diodes élémentaires est augmentée par une association série. Notamment, un assemblage de 64 diodes TVS de 400 V chacune (8 en série et 8 en parallèle), a permis de générer avec succès une impulsion de tension de 3 kV avec un temps de montée de 10 ns sur une charge résistive d'environ 100 Ω. L'étude se poursuit sur le banc d'énergie de 10 J où des diodes de redressement OTS montrent également des capacités intéressantes dans la commutation de courants inverses de plusieurs centaines d'ampères. Par exemple, une tension impulsionnelle d'amplitude atteignant 90 kV et de temps de montée de 20 ns est obtenue sur une charge de 1 kΩ, illustrant ainsi les performances notables de ces diodes dans des conditions de charge variées.

Le **Chapitre 3** est dédié à l'étude des matériaux magnétiques adaptés au transformateur impulsionnel du circuit choisi. Cette étude est réalisée sur le banc de 10 J présenté au Chapitre 2. Le développement de ce banc y est illustré, fournissant une démonstration concrète de la méthodologie de dimensionnement proposée au Chapitre 1. Le chapitre introduit également un circuit additionnel de pré-magnétisation du transformateur, conçu pour une efficacité optimale de fonctionnement en régime de saturation. L'étude met en évidence les propriétés magnétiques des noyaux nanocristallins et l'influence de l'hystérésis du noyau sur le fonctionnement du

transformateur saturable. Dans un premier temps, deux transformateurs sont caractérisés, utilisant des matériaux nanocristallins ayant des boucles d'hystérésis aplatie et rectangulaire, ce qui présente des avantages distincts pour le développement de générateurs SOS. Ces transformateurs sont employés pour créer deux configurations de générateurs : l'une avec une tension de sortie linéairement ajustable et l'autre avec une tension fixe. Par la suite, trois noyaux nanocristallins différents, tant au niveau de leur géométrie que de leur matériau, sont évalués dans trois transformateurs distincts afin de déterminer leurs performances respectives. Grâce au circuit de pré-magnétisation, la tension en sortie du générateur peut être réglée en fonction de l'énergie d'entrée, tout en maintenant une bonne efficacité énergétique du transformateur (∼70%). Ainsi, le générateur délivre une tension réglable de 10 à 200 kV, avec un temps de montée minimum de 16 ns, sur une charge résistive de 50–1000 Ω. Le chapitre se concentre également sur l'analyse du rendement énergétique du générateur en exposant les pertes globales aux différents étages.

Le **Chapitre** 4 de cette thèse est consacré au développement et à la caractérisation d'un prototype de générateur 500 kV, nommé GO-SSOS (*Generator based on an Off-the-shelf Solid State Opening Switch*), basé sur des diodes OTS. Ce prototype est dimensionné pour fonctionner avec une énergie d'entrée pouvant atteindre 40 J et utilise un transformateur impulsionnel de 300 kV. Ce dernier, basé sur un des noyaux nanocristallins étudiés au Chapitre 3, est conçu et bobiné en interne. Le GO-SSOS intègre un thyratron comme commutateur au primaire permettant le transfert de l'énergie du primaire vers le secondaire du transformateur. Ce chapitre présente une vue d'ensemble détaillée du système et décrit son fonctionnement à travers un chronogramme précis. Le contrôle et la commande du système sont assurés par des cartes électroniques Arduino équipées de microcontrôleurs programmables. La caractérisation des shunts résistifs (CVR – Current Viewing Resistors), dédiés aux mesures de courants rapides, est également abordée. Le commutateur à ouverture est composé d'un arrangement de diodes à recouvrement rapide connectées en série, capable de générer une tension maximale théorique de 600 kV. Le rendement énergétique du système varie entre 35% et 70% selon la charge (50–1000 Ω) et la puissance crête obtenue à la charge atteint 335 MW. Sur une charge résistive de 1 kΩ, le générateur produit une impulsion de tension de 515 kV avec un temps de montée de 35 ns et une largeur à mi-hauteur d'environ 80 ns. La reproductibilité des impulsions à une fréquence de répétition de 60 Hz est démontrée, ainsi qu'une application de génération de décharges couronnes. La fréquence de fonctionnement du système est limitée par les caractéristiques du thyratron et de l'alimentation du primaire. Les résultats confirment l'efficacité des diodes OTS comme interrupteurs à ouverture dans des applications de HPP, soulignant leur capacité à générer des milliers d'impulsions sans dégradation notable.

Les résultats de cette thèse montrent qu'avec une sélection minutieuse des diodes OTS, la commutation fiable de courants élevés et la production d'impulsions hautes tensions extrêmement reproductibles peuvent être assurées. De plus, leur capacité à être mises à l'échelle pour répondre à diverses exigences de puissance tout en maintenant leur efficacité est démontrée. Pour optimiser leur fonctionnement, il est essentiel de mener des recherches visant

à mieux comprendre le mécanisme d'interruption du courant dans ces diodes. Ces avancées ouvrent de nouvelles perspectives pour l'utilisation des commutateurs état solide dans des applications de HPP, couvrant divers domaines de la physique et de la technologie moderne.

Contents

List of Figures

List of Tables

Glossary

CES	Capacitive Energy Storage.
CVR	Current Viewing Resistor.
DB	Driver Board.
DBV	Diode Blocking Voltage.
DSRD	Drift Step Recovery Diode.
e-beam	electron beam.
ETO	Emitter Turn-Off.
FWHM	Full Width at Half Maximum.
GO-SSOS	Generator based on an Off-the-shelf Solid-State Opening Switch.
GTO	Gate Turn-Off.
HFR	High-Field Region.
ICCOS	Inverse Current Commutation Characterized by Semiconductor Devices.
IES	Inductive Energy Storage.
IGBT	Insulated-Gate Bipolar Transistor.
IGCT	Integrated Gate Commutated Thyristor.
LTD	Linear Transformer Drive.
MOSFET	Metal-Oxide-Semiconductor Field-Effect Transistor.
MPC	Magnetic Pulse Compressor.
NanoSIMS	Nanometric scale Second Ion Mass Spectrometry.
OTS	Off-The-Shelf.
PRF	Pulse Repetition Frequency.
PTCR	Positive Temperature Coefficient of Resistivity.

SCR	Silicon Controlled Rectifier.
SIMS	Second Ion Mass Spectrometry.
SOS	Semiconductor Opening Switch.
SPT	Saturable Pulse transformer.
SRD	Step Recovery Diode.
TCU	Thyristor or Transistor-based Charging Unit.
TDS	Thyratron Driving System.
TG	Trigger Generator.
TVS	Transient Voltage Suppression.
UPPA	Université de Pau et des Pays de l'Adour.

Introduction

Introduction

The progressive development of man
is vitally dependent on invention

Nikola Tesla

Welcome to the exciting world of solid-state switching in pulsed power, where cutting-edge electronics and high-power applications are converging. Since its discovery in the 1920s by Erwin Marx, the interest in "pulsed power technology", has grown steadily over the years. Initially focused on the military sector, pulsed power systems have gradually found their way into civilian sectors, thanks to the wide range of their applications in various fields. A case in point is electron beam (e-beam) sterilization, offering a method to eliminate viable microorganisms from products while preserving their integrity.

In the food and medical domains, sterilization techniques fall into three main groups: thermal, chemical, and ionizing radiation. Although there is no universal sterilization technique, increasing attention is being drawn to ionizing technologies including the pulsed e-beam accelerator. In this beta-ionizing source, electrons are emitted from a cathode terminal electrode forming a beam, under the influence of applied high-voltage pulses. This beam is then accelerated towards an anode metallic foil in a dedicated diode chamber. The e-beam subsequently passes through the anode foil and reaches the target, depositing a controlled amount of energy per mass unit for sterilization known as a "dose". The energy of the e-beam can be tailored based on the type of product, the required dose, and the penetration depth.

ITOPP, leading company in the pulsed power domain, develops pulsed power generators for e-beam sterilization of agro-food and pharmaceutical product packages. Though far from being the only sterilization technique, this method offers a cost-effective solution, does not require the use of chemicals, and can be integrated into a production line. Moreover, the generator's unique parameters allow for high dose rates, low energy consumption, and efficient treatment. However, the current solutions rely on gas-filled switches, limiting pulse repetition rates and often requiring maintenance due to electrode erosion.

This thesis, funded by ITOPP under a CIFRE (*Conventions industrielles de formation par la recherche*) agreement and carried out within the High-Voltage Processes group of the SIAME Laboratory at the "Université de Pau et des Pays de l'Adour (UPPA)", arose from the need to develop a pulse generator based on solid-state components for e-beam sterilization. The desired system should feature an output voltage of several hundred kilovolts and a peak power of hundreds of megawatts, with nanoseconds pulse duration. The advantages of solid-state pulsed power generators include high reliability, high Pulse Repetition Frequency (PRF), scalability, long lifetime, and sustainability. A promising solution for this system is

the Semiconductor Opening Switch (SOS) generator capable of generating megavolt voltage pulses and operating at a PRF of several kilohertz, producing gigawatt peak powers.

However, the lack of the SOS diodes, which are crucial components of SOS generators, prevents the adoption of this solution. Therefore, this thesis focuses on exploring the use of Off-The-Shelf (OTS) diodes as a high-voltage opening switch for pulsed power generators in general and for pulsed electron beam sterilization in particular. The main objectives are to investigate the OTS diodes and their potential to switch kiloampere currents and generate voltage pulses with an amplitude of up to 500 kV. A pulsed power generator prototype based on an OTS opening switch is developed and tested to fulfill these objectives.

The thesis consists of four chapters, an introduction, a conclusion with perspectives, and appendices. It includes 84 figures, 12 tables, and 124 references, and is structured as follows.

- **Chapter 1** provides an overview of state-of-the-art solid-state opening switches used in pulsed power systems, their structure, and operating principles. It compares opening switch characteristics and contextualizes the study. In addition, it presents circuit architectures of opening switch-based high-voltage generators together with some pulsed power applications using SOS generators. An approach for designing an SOS generator is also proposed.

  The subsequent chapters (2, 3, and 4) are based on articles published within the framework of this thesis.

- **Chapter 2** describes research on OTS diodes as potential high-voltage opening switches on low- and medium-energy test benches of respectively 25 mJ and 10 J energy. It outlines the chosen diodes and their selection criteria. It further provides details of OTS diodes' performance in comparison with reference SOS diodes.

- **Chapter 3** covers a study on nanocrystalline magnetic cores for a Saturable Pulse transformer (SPT). The exceptional properties of nanocrystalline materials, making them suitable for the SPT, are outlined. The chapter includes the SPT design considerations and presents two SOS generators based on a single magnetic element. It discusses a novel method of output voltage adjustment that has been proposed.

- **Chapter 4** presents the proof of concept of the 500 kV nanosecond high-voltage generator based on an OTS diode. It details the design of a high-energy test bench for investigating an OTS diode. Auxiliary components and associated diagnostic equipment used to control and monitor the system operation are covered. Furthermore, the characterization of the generator prototype and a corona discharge application are reported.

Join the journey as we explore the details of solid-state switching and discover how it makes pulsed power systems more efficient and reliable.

Chapter 1

Solid-state switching in pulsed power

Chapter 1

Solid-state switching in pulsed power

This chapter provides a brief overview of pulsed power technology, with a focus on opening switches. A review of state-of-the-art solid-state opening switches and their applications is presented. The discussion also includes solid-state pulsed power generators' circuit approach and design considerations.

1.1 General overview of pulsed power technology

This section presents an introduction to pulsed power technology. The crucial role of the switch is discussed.

1.1.1 Introduction to pulsed power

The principle of pulsed power relies on the long-term storage of electrical energy, and its subsequent rapid release into a load to increase the peak electrical power [1]. The basic concept in pulsed power engineering is time compression, leading to an amplification of the voltage, current, or both, and therefore a substantial power multiplication is achieved. One can considerably increase the peak power by significantly reducing the energy release time, as illustrated in Figure 1.1.

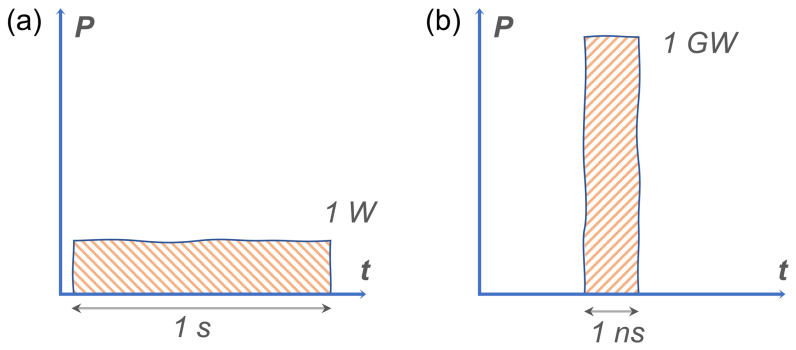

Figure 1.1: Pulsed power concept of energy compression in time: (a) long storage of 1 J and (b) fast discharge of the same energy.

The basic structure of pulsed power systems comprises four essential components according to [2]: the primary energy source, the energy storage unit, the pulse forming section, and the load, as shown in Figure 1.2. The primary energy source, which can be a dc power supply or a charger, draws power from the mains (e.g., 230 V single-phase or 400 V three-phase in France). It raises the voltage, often to a range of a few kilovolts or even tens of kilovolts, and delivers the energy to the storage unit within a time frame of seconds or milliseconds. This energy is generally stored in capacitors or inductors, representing electrical or magnetic forms, respectively [3]. Furthermore, the energy undergoes discharge within microsecond to nanosecond time range by activating a switch, generating a high-voltage pulse typically ranging from kilovolts up to megavolts at the load.

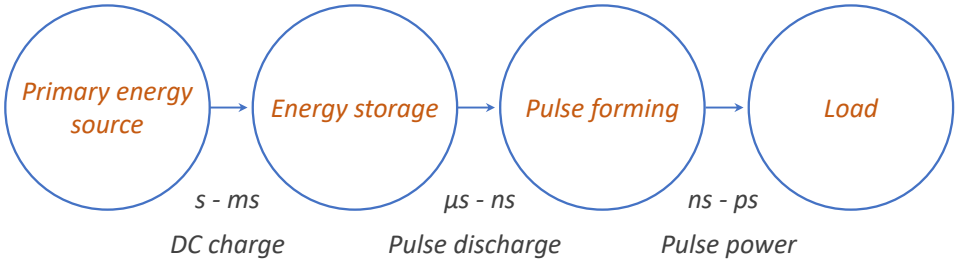

Figure 1.2: Block diagram of a typical pulsed power system.

The switch is the key element in pulsed power systems, leading to pulse energy compression and power amplification. Its crucial role can be illustrated by the Marx generator, one of the most widely used pulsed power generators [1]. The Marx generator (Figure 1.3) is a voltage-multiplying circuit in which multiple capacitors are initially charged in parallel and subsequently discharged in series, through the process of sequential closing switches. The result is the cumulative and amplified output voltage at the load.

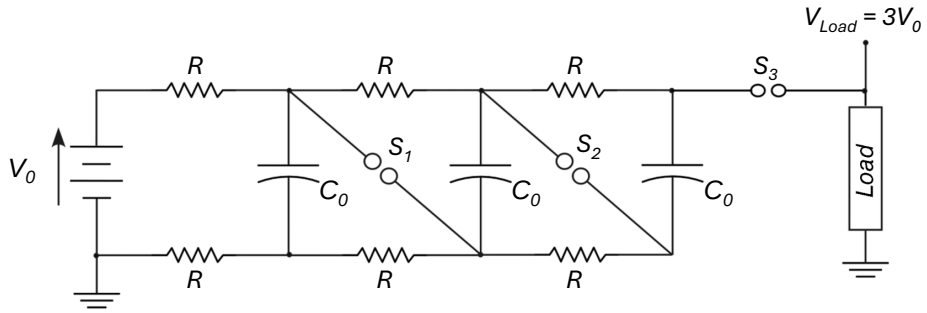

Figure 1.3: Architecture of a 3-stage Marx generator [1].

The switches (S_1, S_2, and S_3) in the example presented in Figure 1.3 are gas-insulated spark gaps consisting of two electrodes, one at high voltage and the other connected to ground. The spark gap switch remains open as long as the potential difference between the two electrodes is less than the gas breakdown voltage. It can self-ignite when the differential voltage across its electrodes exceeds the breakdown threshold, or it can be triggered by a trigger electrode which pre-ionizes the inter-electrode gap, facilitating the triggering process. The output pulse parameters of the Marx generator are highly dependent on the characteristics of each switch, such as switching time, current/voltage capability, time jitter, etc.

Depending on the requirements of a Marx generator, solid-state switches can be employed, offering advantages, in terms of compactness, PRF, and stability. However, connecting multiple switches in series and/or parallel is often necessary to maintain high voltage and high current levels. Synchronized switch triggering techniques are thus essential to minimize jitter. An example can be found in [4], where two Marx generators based on 120 thyristors, one consisting of 120 stages and the other with 6 stages, were developed to generate a voltage pulse of 120 kV.

The important role of switches in pulsed power systems can also be highlighted by the Tesla generator shown in Figure 1.4. This generator is based on a Tesla transformer, that steps up the primary low voltage to high voltage in the secondary. The voltage multiplication factor corresponds to the square root of the ratio of secondary and primary inductances which are coupled.

Tesla generator basically uses two switches: a low-voltage switch in the primary circuit (S) and a high-voltage switch in the secondary circuit (GS) (Figure 1.4). The low-voltage switch allows energy to be transferred from the primary to the secondary circuit via the transformer. Due to the inductive coupling, the primary and secondary circuits oscillate at equal oscillation frequencies ($L_1C_1 = L_2C_{FL}$). The high-voltage switch enables the shaping and forming of the output load (R_D) pulse dedicated to specific applications [5].

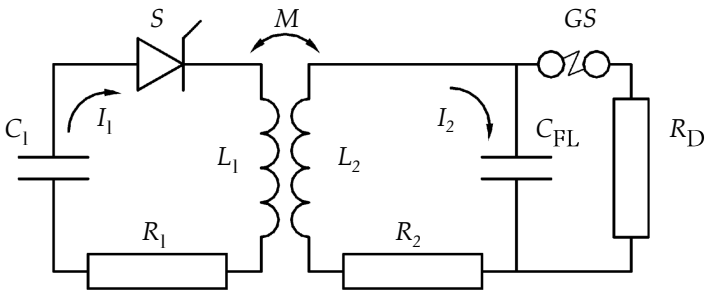

Figure 1.4: Circuit diagram of a pulsed power generator based on a Tesla transformer of mutual inductance M, with a pulsed forming line represented by the line capacitor C_{FL} and the gas switch GS [6].

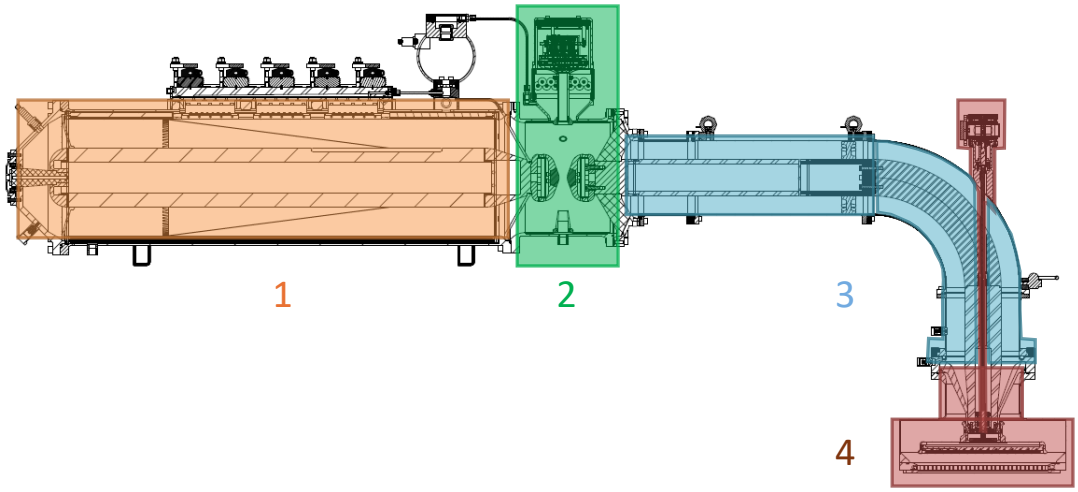

Figure 1.5: An example of ITOPP electron accelerator based on SINUS, showing the Tesla transformer–1, the spark gap switch–2, the transmission line–3, and the vacuum diode–4.

The development of pulsed electron accelerators in ITOPP had essentially been focused on generators based on Tesla transformers called SINUS [7], [8]. These generators provide

high e-beam current with an amplitude of 2–20 kA, cathode voltage of 0.2–2 MV, duration of 4–130 ns, and pulse repetition rate of up to 1 kHz [6]. The SINUS systems employ a coaxial pulse forming line, integrating a spark gap high-voltage switch, to shape the pulse as depicted in Figure 1.4. The reliability of the system largely depends on the reliable operation of the switch and its reproducibility. A picture of a pulsed electron accelerator is presented in Figure 1.5.

However, a gas switch presents several disadvantages for industrial use. First, the inter-electrode gas of the spark gap requires time to recover its insulating properties after switching. For example, the PRF of the SINUS generators described in [6] is limited to 400 Hz for voltages over 200 kV even though a three-electrode spark gap is used for stability of the triggering and forced circulation of the gas is conducted to accelerate the switch recovery. In addition, the lifetime of the switch is limited due to erosion of the electrodes caused by the high switched current, thus frequent maintenance is required, which is unsuitable for industrial use.

The need for a more reliable and sustainable system with high PRF operation led to the elaboration of the thesis subject, which focuses on solid-state switches for the high-voltage generation of several hundred kilovolts. Before diving into the heart of the matter, the upcoming section looks at the distinctive features of closing and opening switches.

1.1.2 Closing and opening switches

The concept of time compression may seem straightforward, yet it lies at the heart of the complexity of pulsed power systems. This function is ensured by the switch, which controls the discharge and conditioning of the energy from the storage unit. There are fundamentally two types of switches depending on the energy storage, the two most used being capacitive and inductive storage [9]. Closing switches are applied in Capacitive Energy Storage (CES) systems, like in the Marx generator presented in Section 1.1.1, while opening switches are required in Inductive Energy Storage (IES) systems (Figure 1.6).

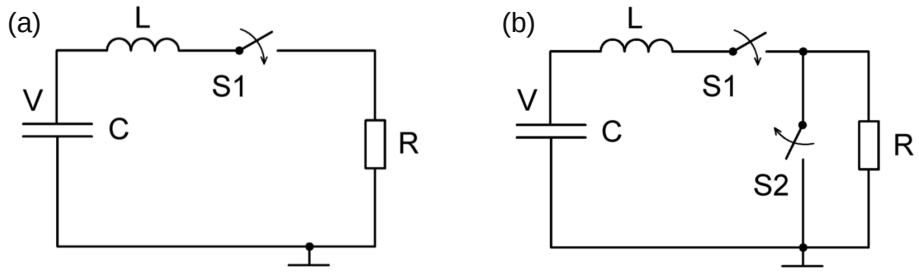

Figure 1.6: Simplified discharge circuit for (a) CES and (b) IES [10].

In the case of CES, as shown in Figure 1.6 (a), the capacitor C, initially charged to a voltage V, is discharged through the inductance of the circuit L and the load R, when the closing switch S1 is activated. As for the IES system in Figure 1.6 (b), when all switches

are closed, the stored energy is transferred from the capacitor to the inductance L, which becomes an active inductive storage. Then, at the opening of S2, ideally at maximum current, the energy is transferred from the inductance L to the load R.

This circuit comparison of the IES and CES highlights two main advantages of the IES [10]. First, the active inductive storage allows the energy from the capacitor to be transmitted in a shorter time, leading to an increase in the peak power. Second, when the opening switch interrupts the current, the load voltage amplitude is amplified in comparison with the initial voltage stored in the capacitor. In addition, IES offers up to two orders of magnitude higher energy density than CES, according to [9]. Moreover, as stated in [11], only inductive storage presents both high energy density and high electrical power capability. Thus, inductive storage is preferable for compact systems with substantial peak power.

Nevertheless, switching off a high current of several kiloamperes in nanoseconds duration remains particularly challenging. Electrically exploded conductors and plasma opening switches have demonstrated the ability to cut off tens of kiloamperes, generating megavolt voltages of nanosecond duration [3]. However, these technologies are constrained by limitations such as low PRF and short lifetime [3], [10]. These drawbacks can be overcome by solid-state switches offering unlimited lifetime and high PRF. Therefore, solid-state opening switches with blocking voltages up to hundreds of kilovolts, switching powers up to hundreds of megawatts, low losses, and nanosecond switching times are of interest in this work.

1.2 Solid-state opening switches

Solid-state switches in power electronics have evolved significantly due to advances in semiconductor technology. Traditionally, these switches have been made primarily from silicon (Si), benefiting from its wide availability, well-established manufacturing processes, and mature technology [12]. However, modern research and development efforts are increasingly focusing on wide and ultra-wide bandgap materials, such as silicon carbide (SiC), gallium nitride (GaN), and aluminum nitride (AlN). These materials are attracting attention for their superior performances at higher temperatures, voltages, and operating frequencies [13], [14].

Despite the current interest in advanced semiconductor materials, the use of semiconductor devices to interrupt current in IES is far from being recent. Back in the 1970s, semiconductor materials offering a Positive Temperature Coefficient of Resistivity (PTCR) effect were of interest in pulsed power switching. For instance, in [11], PTCR devices made from some specific materials, like barium titanate or carbon film polymer, were applied as opening switches. When these materials experience joule heating, their resistance increases, effectively creating a self-limiting mechanism for current flow. From the early experiments reported in [11], the voltage amplitude remained below 1 kV and the current interruption time was approximately 1 ms. In addition, the process requires control of the temperature, representing a deterrent constraint to using such a technique.

Over the years, semiconductor technology development has led to the emergence of more advanced solid-state opening switches in pulsed power systems, which fall into two categories: controlled and uncontrolled switches.

1.2.1 Opening switch based on controlled semiconductor components

The controlled switches used in pulsed power systems include thyristors, Metal-Oxide-Semiconductor Field-Effect Transistors (MOSFETs), and Insulated-Gate Bipolar Transistors (IGBTs).

1.2.1.1 Thyristor opening switches

The thyristor is a three-terminal device known as the anode (A), the gate (G), and the cathode (K) as depicted in Figure 1.7. Structurally, it consists of four layers in a "$p-n-p-n$" arrangement, with three $p-n$ junctions (J1, J2, and J3). In its initial state, the thyristor effectively blocks forward and reverse voltage applied to its anode, provided the voltage is within its specified limits. When the applied voltage exceeds these limits, the thyristor enters avalanche mode due to the excessive carrier multiplication.

Operating as a normally open switch, the thyristor initiates conduction when it receives a trigger pulse at its gate. Once switched on, the gate signal can be removed, and the thyristor will remain conducting until the anode-cathode current falls below the device holding current. Detailed information on the structure, characteristics, and operation of thyristors can be found in [4], [13], [15]–[17].

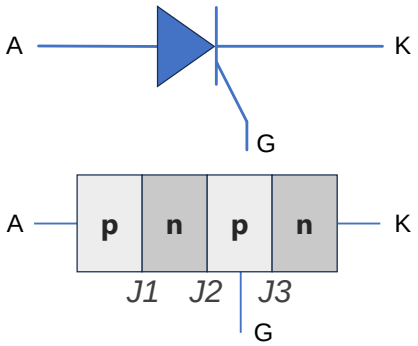

Figure 1.7: Electrical symbol of a thyristor and its basic structure.

Another method for triggering thyristors is the impact-ionization wave mode, as detailed in [18]. This mechanism consists of applying a steep positive overvoltage directly to the thyristor anode, bypassing the gate that remains open. A fast rate of rise of the voltage (dV/dt) is necessary, though. In [19], it was established that a minimum dV/dt of 2–3 kV/ns is required to effectively trigger a thyristor in the impact-ionization wave mode. Under these conditions, the device switching characteristics surpass the specifications given in the datasheet [18].

Switching on the thyristor can also be achieved through optical signals using a method known as light or laser activation [3], [17]. In this approach, the thyristor is exposed to a light source through an optical fiber. The absorption of photons generates electron-hole pairs within the device structure, thereby producing the triggering current. This method offers the advantage of isolating the trigger circuit from the power circuit and facilitating the simultaneous switching of several devices connected in series [15].

Regardless of the switching-on method, employing the thyristor as an opening switch depends on its ability to quickly zero or reverse the anode current. This can be achieved either by forcing a zero current using an external counter-current circuit, or, in the case of specific types of thyristors, by applying a negative pulse signal to the thyristor gate. The types of thyristors that particularly suit the high-power opening switch application are the Silicon Controlled Rectifier (SCR), the Gate Turn-Off (GTO) thyristor, and its variants [11]. The utilization of these types of thyristors as opening switches is discussed in the following.

Silicon Controlled Rectifier (SCR) as an opening switch

The SCR functions like a typical thyristor, remaining closed until the anode-cathode current reaches zero. During the zero-current period, carriers are swept out of the two outer junctions (J1 and J3 in Figure 1.7), while the junction J2 recovers through carrier recombination [11]. Hence, the operation of the SCR as an opening switch involves the application of a counter pulse current to zero the current for a sufficient duration allowing for recombination. Typically, this counter pulse current is supplied by an external circuit [11].

In the study detailed in [20], two thyristors were employed as opening switches on the principle of Inverse Current Commutation Characterized by Semiconductor Devices (ICCOS). The circuit is depicted in Figure 1.8 and operates as follows. Once the capacitor (energy source) is fully charged, the main switch THYm is closed, transferring energy to the storage coil. When the current in the coil has reached its maximum, the THYc switch closes and the counter-capacitor Cc discharges through THYm, supplying a reverse current and forcing the main current to zero. Thereafter, THYm opens, interrupting the main current, and then the coil discharges through the load.

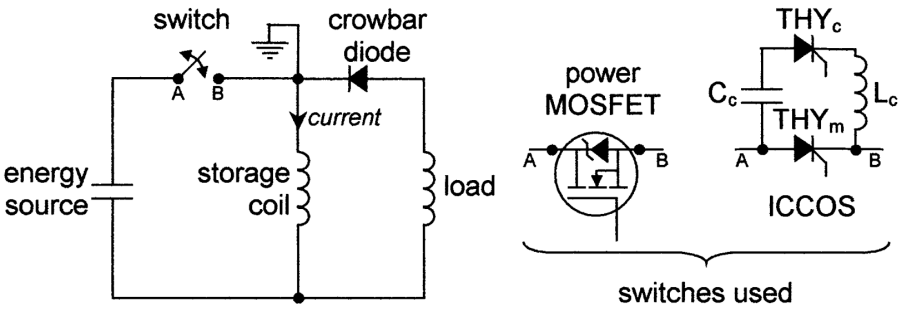

Figure 1.8: Circuit arrangement for SCR switches investigation in the ICCOS principle [20].

In the experiment detailed in [20], the SCR interrupted a total current of nearly 20 kA in almost 25 µs when the source voltage was 2.4 kV. This counter-current method was also used to switch off twenty SCRs in the 20-stage XRAM generator described in [21]. The XRAM (Marx spelled backwards) is an IES system in which several stages of inductors are charged in series when the SCR switches are closed, and discharged simultaneously in parallel when the SCRs open, thus multiplying the charging current by the number of stages. In [21], a current amplitude of 3 kA was interrupted by each of the twenty SCRs, resulting in a 60 kA peak current of 2 ms duration at the load, when the charging voltage of the generator was 430 V.

Gate Turn-Off (GTO) thyristor as an opening switch

The GTO thyristor is a type of SCR that can be turned off by applying a reverse current to its gate. The reverse current must be high enough to remove the stored charge from the $p-$gate region and disrupt the regeneration process of carriers. In [22] a reverse gate pulse signal was applied to switch off a 2.5 kV GTO in a long-charge inductive-store circuit. The result demonstrated an interrupted total current of about 5 kA in nearly 3 µs switching time while the voltage was 1.5 kV. A faster switching time of less than 100 ns was achieved in [23] using an n-type GTO with a blocking voltage of 8 kV. The switched current amplitude was about 100 A. One should note that the complexity of the circuit increases, especially when several GTOs are series-connected, due to the necessity of snubber circuits to protect the devices, along with electronic control requirements for synchronous switching [24], [25].

Additionally, GTO-like devices such as the Integrated Gate Commutated Thyristor (IGCT), MOS Controlled thyristors, MOS turn-off thyristors, Emitter Turn-Off (ETO) thyristor, and static inductor thyristor [1], [26] can be considered. The main improvements to these derived devices are the inductance minimization to speed up the switching process and reduce losses, as well as the circuit integration for higher reliability and improved gate drive [26]. Although extensively studied, these systems have lower switching speeds compared to transistor-based switches discussed further.

1.2.1.2 Transistor-based opening switches

The main transistor-based switches are MOSFETs and IGBTs. Their underlying physics is well described in [13], [15], [17].

The MOSFET is a three-terminal device consisting of a drain, a gate, and a source. It is controlled by a voltage applied to its gate terminal and exhibits a switching-off time in the nanosecond range due to the absence of carrier recombination [15]. However, its power capacities are limited compared to thyristors. An example of MOSFET use as an opening switch in pulsed power systems is described in [27]. The switches were studied in an inductive adder system for obtaining a flat top pulse with fast rise and fall times required for an injection kicker. Rise time and particularly fall time of about 100 ns were obtained when the SiC MOSFETs of the ten-layer inductive adder system were switched on and off. The built

prototype generates a voltage of 10 kV amplitude with 2 µs flat top on a 50 Ω resistive load.

The IGBT is also a three-terminal device featuring a collector, a gate, and an emitter. It is turned on by applying a voltage to the gate terminal and turned off by removing the voltage from the gate. The IGBT combines the high-power capability of a thyristor with the fast switching ability of a MOSFET. An application of IGBT as an opening switch for an XRAM generator is discussed in [28], where the IGBT stack interrupts a current of up to 5 kA in 9 µs. The blocking voltage of the two switches in the stack was 4 kV.

In a nutshell, controlled semiconductor components have come a long way over the years and offer significant advantages in power switching. However, as high-power opening switches, they are limited to switching times of hundreds of nanoseconds to a few microseconds, voltage withstand values of tens of kilovolts, and peak power of a few tens of megawatts. Moreover, the combination of several components in series is necessary to withstand the high voltages needed in pulsed power applications. This requires the use of power distribution circuits to evenly spread the voltage across the components, not to mention the necessary protection circuits. In addition, synchronized switching remains a challenge. All this contributes to the increased cost of these switches. Hence, the controlled semiconductor opening devices appear to be unsuitable for generating high voltages of several hundred kilovolts in the nanosecond range.

Over the last decades, one of the simplest semiconductor devices containing a single $p-n$ junction – the diode – demonstrated its ability to reliably interrupt high-density currents in the nanosecond range, surpassing the performance of its pairs. The advantages of this component are explored in the next section, where we delve into uncontrolled solid-state switches.

1.2.2 Uncontrolled solid-state opening switches in pulsed power systems

The introduction of the Step Recovery Diode (SRD) or the storage diode [29] may be considered as the beginning of the nanosecond solid-state opening switches history. These diodes feature a built-in retarding electric field that limits the propagation of minority carriers inside the device during the forward current phase and accelerates the removal of the charges during the reverse conduction phase. Although these devices exhibit a rapid current cut-off of a few nanoseconds or less, their limitations include operating voltages of tens of volts and current ratings in the milliampere range [30]. Later, the discovery of the Drift Step Recovery Diode (DSRD) [31] and the SOS diode [32] marked a significant advancement in solid-state opening switches, enabling switching powers to reach megawatt and even gigawatt levels. This development put a spotlight on the nanosecond high-voltage semiconductor switches.

1.2.2.1 Drift Step Recovery Diode (DSRD)

The DSRD is a $p^+ - p - n - n^+$ device based on a fast recovery process termed junction recovery [33]. In this process, the current interruption occurs due to the recovery of the $p-n$ junction blocking capability. The operation consists of a short current pulse passing through the diode in a forward direction, followed by a reverse current pulse. Figure 1.9 (a) illustrates the doping profile

of the diode and the electron-hole plasma distribution at the end of the forward pumping stage.

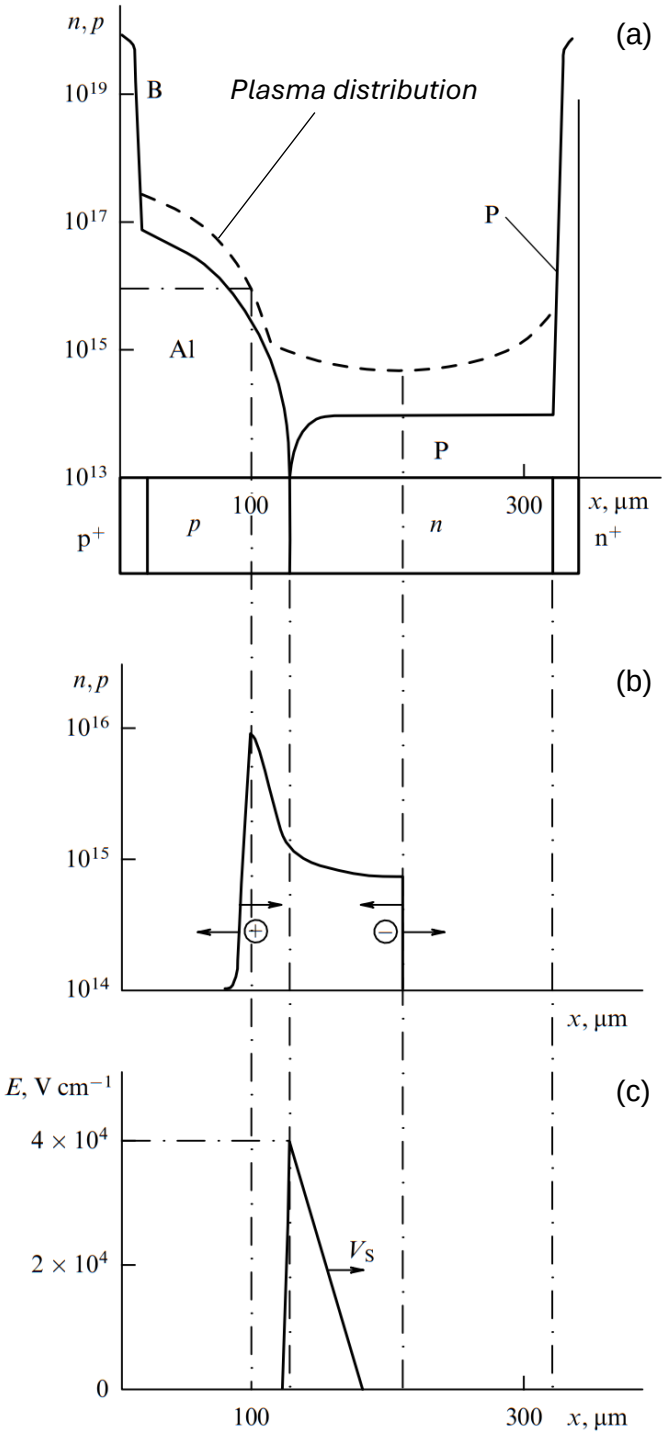

Figure 1.9: (a) $p^+ - p - n - n^+$ DSRD structure with plasma distribution at the stage of the forward current pulse. (b) Motion of plasma fronts during the reverse current stage. (c) Space charge region formation [34].

As reported in [33], due to a very short forward current pulse of 100-200 ns, a non-uniform

distribution of the electron-hole plasma is observed in the diode structure near the $p-n$ junction during the reverse current flow. This plasma comprises two fronts: a high-density thin layer in the $p-$region and a low-density thick layer in the $n-$region [Figure 1.9 (b)]. Eventually, the two plasma fronts collide precisely at the $p-n$ junction, resulting in the recovery of the space charge region [Figure 1.9 (c)]. According to this principle, the charge introduced in the structure during forward pumping is equal to the charge removed from the structure during reverse pumping [35]. As the $p-n$ junction recovers, a rapid interruption of the reverse current occurs within a cut-off time of about 1 ns.

A powerful semiconductor nanosecond pulser based on DSRD is described in [36]. The generator loaded on a resistance of 100 Ω delivers a voltage pulse of up to 80 kV with a rise time of 0.9 ns and a duration of approximately 2 ns. With a peak power of around 60 MW, this generator is compact, occupying a volume of 150 x 150 x 100 mm^3, and can operate at a repetition rate of up to 1 kHz.

The main drawback of the DSRD lies in its low cut-off current density limited to 200 A/cm^2, as there is no residual plasma in the base of the structure at the current cut-off stage [10]. Consequently, the peak power that can be switched by the DSRD is in the order of hundreds of megawatts [32].

1.2.2.2 Semiconductor Opening Switch (SOS)

In contrast to the DSRDs and other opening switches described above, SOS diodes can interrupt high-density currents of up to 100 kA/cm^2, having equal voltage distribution among series-connected diodes, which allows generating pulses with gigawatt peak power [10]. As reported in [32], the SOS effect was discovered in 1992-1993 at the Institute of Electrophysics of the Ural Branch of the Russian Academy of Sciences. This effect, defined as the interruption of superdense currents in semiconductors, was observed in silicon diodes having the $p^+-p-n-n^+$ structure. Although the physics of operation differs from DSRD, the circuitry of SOS is similar to DSRD. It is based on providing a forward pumping current to the diode followed by a reverse pumping current that is rapidly cut off within the nanosecond duration range. The current interruption eventually leads to a nanosecond high-voltage pulse at the load.

SOS structure and doping profile

The structure and doping profile of the SOS diodes are elaborated in [37] and illustrated in Figure 1.10. In this representation, the structure comprises a $p^+-p-n-n^+$ profile characterized by a deep $p-n$ junction of about 180 µm, which is about twice the typical depth of the $p-n$ junction in DSRDs of about 100 µm as shown in Figure 1.9 (a). The $n-$base consists of $n-$type silicon, while the p^+, p, and n^+ regions are doped by diffusion of boron (B), aluminum (Al), and phosphorus (P) respectively.

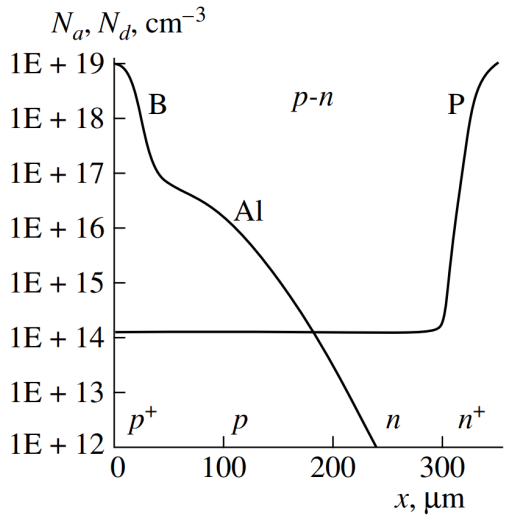

Figure 1.10: Doping profile of an SOS diode [37].

Operating principle of SOS diodes

The operating principle of SOS diodes can be explained using the circuit shown in Figure 1.11. This circuit, taken from [10], schematizes the experiment that led to the discovery of the SOS effect [38]. In this experimental setup, the capacitive storage represents a Marx generator storing energy ranging from 10 J to 2 kJ, with an output voltage of 50-150 kV. The purpose was to investigate the capability of a semiconductor diode to conduct high reverse currents.

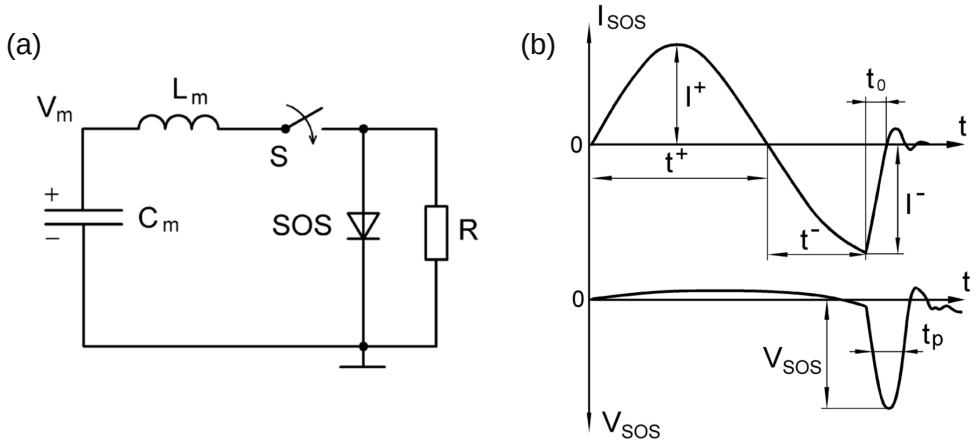

Figure 1.11: (a) Experimental circuit of an SOS diode. (b) Waveforms of the current through and voltage across the SOS [10].

The circuit operates as follows. When the switch S is closed, the Marx generator discharges through the inductance L_m and the SOS. The discharge current flows through the SOS in the forward direction. Through a suitable combination of the forward pumping current magnitude, I^+, with the duration of the forward current, t^+, the diode conducts the reverse current

up to its maximum amplitude I^-, for the duration t^-. Subsequently, the reverse current is rapidly cut off by the diode within the time t_0 shorter than t^-, generating a voltage pulse of amplitude V_{SOS} and duration t_p across the resistive load R. The principal parameters of current and voltage amplitudes and durations are indicated in Figure 1.11 (b).

Numerous experimental and theoretical studies have examined the process of current interruption by the SOS diode [35], [37], [39], [40], establishing the mechanism that is described as follows. In the time of the forward pumping, a double injection of the carriers occurs under the influence of the applied electric field. Electrons drift from the $n-$region toward the $p-$region, while holes move in the opposite direction from the $p-$region and progressively fill the $n-$base. As a result, two plasma waves propagate in opposite directions from the $p-n$ junction. Since electron velocity is greater than hole velocity, and due to the diode's particular doping profile, the plasma is non-uniform at the end of forward pumping. The greater part of the accumulated charge is concentrated in the heavily doped regions [Figure 1.12 (a)].

The reverse pumping is initiated when the reverse current starts flowing through the switch. The plasma reverses its direction of motion, moving back toward the $p-n$ junction. Figure 1.12 (b) depicts the plasma front motion. As the velocity of the plasma is inversely proportional to the density of dopants, the plasma left and right fronts are sharpened. The regions behind the plasma front are virtually free of injected charge carriers. In these regions, the current is carried only by majority carriers whose concentration is minimal on the outer side of the plasma front.

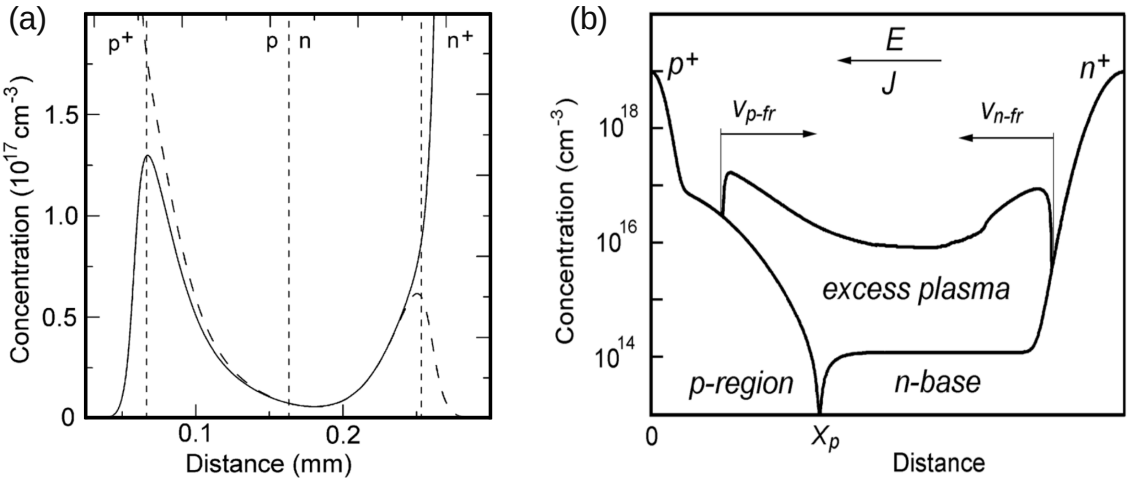

Figure 1.12: (a) Electron (solid line) and hole (dashed line) plasma distribution at the end of forward pumping stage. (b) Plasma front motion at the reverse pumping stage [10].

As the plasma continues its motion, space charge regions with a high electric field (High-Field Region (HFR) [10]) appear on either side of the $p-n$ junction. It is important to note that the electric field in the $p-$region is greater in amplitude and expands faster than in

the $n-$region due to the higher velocity of electrons (Figure 1.13). As a result, the current interruption takes place in the highly doped $p-$region of the diode while the $p-n$ junction and the base of the device remain filled with dense excess plasma. This distinguishes the SOS effect from the DSRD in which the current interruption occurs at the $p-n$ junction. Thanks to the high concentration of acceptors in the $p-$region, the SOS combines a high density of interrupted current (more than 1 kA/cm^2 [32]) and a nanosecond current interruption time [41].

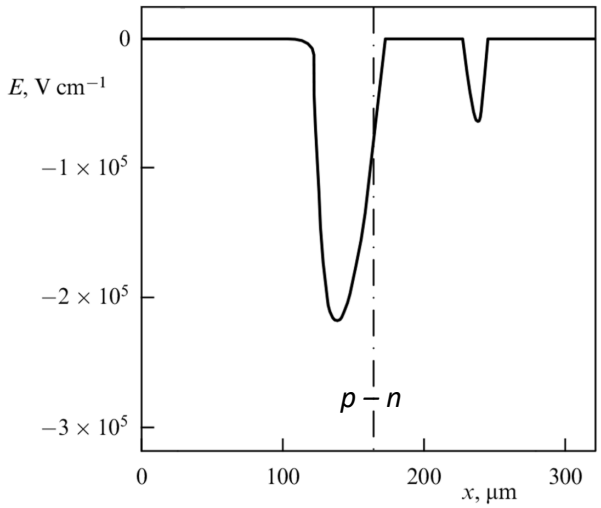

Figure 1.13: Electric field in the SOS diode structure at the moment of highest voltage across the diodes [34].

Another noteworthy feature of the SOS diodes is their automatic voltage distribution over series-connected diodes during the current interruption phase [10]. This feature was investigated in [42] where a stack of ten series connected SOS diodes was studied using the theoretical model described in [35]. The diodes in the stack have different $p-n$ junction depths from 170 to 188 µm, as this depth is the main characteristic determining the process of the HFR that occurs during the current interruption phase [42]. The outcomes indicate that the HFR emerges later but expands more rapidly in diodes with deeper $p-n$ junctions, in contrast to devices with shallow $p-n$ junctions, at the current interruption stage. As a result, the width of the HFR is almost identical for all the diodes in the stack (less than 5 µm difference). This ultimately leads to an even voltage distribution across the series-connected diodes, with a voltage deviation of 4% in [42], when the current is interrupted. Thus, a large number of diodes, over a thousand, can be connected in series to achieve a megavolt pulse level without requiring a voltage distribution circuit [10], [43], [44].

In [45], the SOS switch used as the final stage power amplifier of the nanosecond repetitive generator producing voltage pulses of 1 MV was presented. The switch consists of eight parallel branches of ten diodes connected in series, giving a total of eighty SOS diodes each capable of blocking a voltage of 120 kV. A typical waveform of the reverse current through an SOS diode of 1 cm^2 area is presented in Figure 1.14. The graph shows a reverse current

with an amplitude of 5.5 kA and a cut-off time of approximately 4.5 ns resulting in a current switching rate of about 1.2 kA/ns.

Figure 1.15 (a) illustrates a typical SOS diode design. The device comprises a stack of elementary diodes connected in series, fixed by dielectric rods between two output electrode flanges. Each elementary diode is mounted on a heat sink and consists of four soldered dies connected in series, terminated by copper and molybdenum disks. The heat sink helps to cool the device, particularly during a repetitive mode of operation. For single-mode or burst-mode operation, the elementary diodes [Figure 1.15 (b) and (c)] can directly be stacked on top of each other [10].

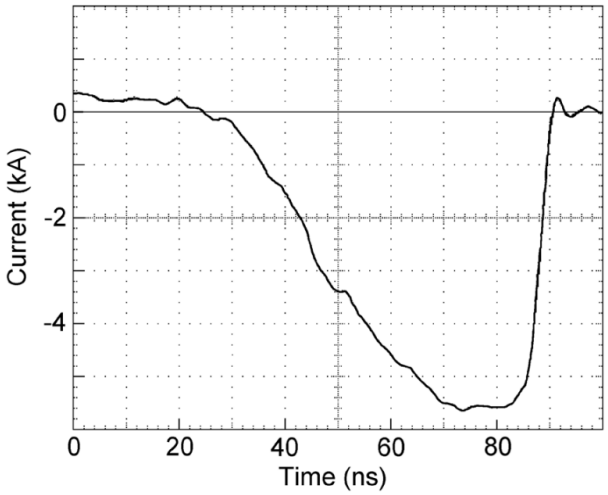

Figure 1.14: Reverse current waveform through an SOS diode [10].

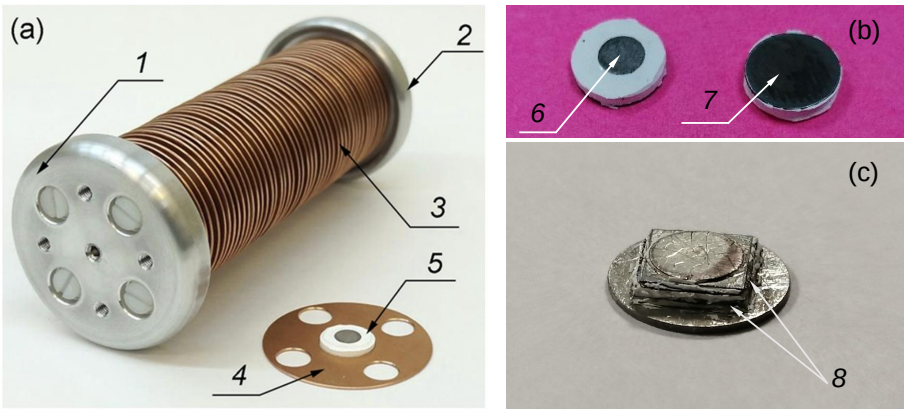

Figure 1.15: (a) The SOS-200-8 stack [10] (blocking voltage: 200 kV, cut-off current: 8 kA, diameter: 64 mm, length: 156 mm, and mass: 760 g): 1–cathode electrode, 2–anode electrode, 3–stack of series-connected diodes and coolers, 4–heat sink, 5–elementary SOS diode. (b) and (c) Elementary SOS diode of 10 mm diameter: 6–cathode in copper, 7–anode in molybdenum, 8–four dies in series.

Particularity of deep p-n junctions

A deep $p-n$ junction from 150 µm to 200 µm is typical for SOS diodes, one can see an example of 180 µm depth in Figure 1.10. Research in [37] highlights the importance of the $p-$region width in the nanosecond interruption time regime. In this study, the $p-$region depth was varied from 100 µm to 200 µm in 20 µm increments. The findings indicate that a wider $p-$region causes a reduction in energy dissipation during the forward pumping phase, due to the shortening of the lightly doped $n-$region. In addition, as the $p-$region widens, the average carrier density decreases, resulting in a higher plasma front velocity. Hence, an increase in the width of the $p-$region (and the depth of the $p-n$ junction) ultimately leads to faster current cut-off and higher voltage at the load.

Achieving such deep $p-n$ junctions is made possible through aluminum diffusion, as aluminum has one of the highest diffusion coefficients in silicon [46], [47]. However, it is also a major constraint in the manufacture of SOS diodes due to the tremendous requirement for temperatures of up to 1200°C and processing times of forty hours or more [46]. These challenges contribute to the limited availability of SOS diodes on the market.

1.2.3 Summary of solid-state opening switch characteristics and development options

The various parameters and characteristics of the opening switches described above are listed in Table 1.1. Controlled switches do not appear suitable for generating high-voltage nanosecond pulses, although widely used in pulsed power systems. Their shortest switching times are in the order of hundreds of nanoseconds, and their switching power does not exceed a few tens of megawatts. On the other hand, DSRD and, particularly, SOS diodes demonstrate switching times of a few nanoseconds, producing megavolt voltage impulses with peak power of gigawatt level.

Table 1.1: Characteristics of solid-state opening switches

Opening switch	Blocking voltage (kV)	Current rate of rise ($kA/\mu s$)	Current density (kA/cm^2)	Switching time (ns)	Switching power (GW)
Thyristor/MOSFET/IGBT	∼10	∼1	-	>100	<0.1
DSRD	<100	∼100	0.1-0.2	∼1	<1
SOS diodes	∼1000	∼1000	>1	∼10	∼10

In light of the comparison in Table 1.1, SOS diodes appear to be the best solution for generating nanosecond pulses with a voltage in the order of hundreds of kilovolts. However, as mentioned previously, the deep $p-n$ junction requirement makes them difficult to manufacture. Furthermore, the low demand for SOS diodes in the market contributes to their limited availability. Since the SOS effect was originally discovered in power rectifier diodes, one can assume the possibility of using power diodes as opening switches, as evidenced in a few studies.

For instance, in [38], ninety high-power diodes of 160 kV each were used to switch up to 45 kA reverse current in less than 70 ns and generate a 500 kV nanosecond pulse into a vacuum diode of an electron accelerator. Moreover, the article discusses the development of megavolt generators, using the power diodes. However, it should be pointed out that the KC and SDL power diodes (KC105D, 10 kV; SDL-1600, 160 kV [10]) referred to in this article are difficult to source.

In addition, as described in [48], less than 20 ns current interruption is observed in commercial fast recovery diodes, which generate voltage pulses of 53 kV amplitude with a duration of less than 20 ns across a 200 Ω load. Moreover, the use of fast recovery surface mount diodes as an opening switch is reported in [49], where pulses of 3 ns duration and 600 V amplitude across a 50 Ω load were obtained. However, the energy levels, in these two studies, do not exceed 2.5 J, and the generated voltages are below 60 kV. On the other hand, the diodes used present a risk of discontinuity, and therefore cannot be relied upon.

Thus, our study covers a wide energy range, from 25 mJ to 40 J, utilizing modern components. Furthermore, the work aims to achieve high voltage generation with a target of up to 500 kV using standard diodes readily available. OTS diodes that can operate as nanosecond high-voltage opening switches are investigated in comparison with reference SOS diodes, whose circuit parameters and applications are described in the following section.

1.3 Typical schematics of SOS generators

The development of SOS technology has advanced the solid-state pulsed power field as the SOS generators have demonstrated the ability to generate voltage pulses with a megavolt peak amplitude [43] and gigawatt peak power [50]. Typical parameters of some of the SOS generators developed at the Institute of Electrophysics are presented in Table 1.2.

Table 1.2: Parameter of state-of-the-art SOS generators [10], [45], [50], [51]

Parameter	SOS gen.	SM-2N	SM-3NS	S-5N	S-500
Output peak voltage (kV)	40–100	100–200	200–400	500–1100	500–900
Pulse current (kA)	0.2–0.8	0.2–0.4	1–3	1–4	7–12
Peak power (GW)	0.02–0.03	0.03–0.05	0.4–0.6	1–2	5–6
Pulse duration (FWHM*) (ns)	10–14	25–40	5–8	35–60	6–8
Continuous PRF (kHz)	20	1	0.3	0.3	0.2
Burst PRF (kHz)	100	5	3	1	1
Output average power, cont. (kW)	5	0.8	0.7	30	-
Output average power, burst (kW)	-	4	4	-	-
Case length (m)	1.5	0.62	1.4	3.5	6
Mass with transformer oil (kg)	∼200	∼50	∼300	∼2,800	∼3,400

* Full Width at Half Maximum (FWHM).

These generators find their use in many fields of applications, including streamer discharge in gases and liquids, the study of electrophysical properties of semiconductors and dielectrics, e-beams and X-ray radiation pulses, etc. [45].

In [52], an IES generator based on an SOS diode was explored for water treatment using pulsed streamer discharge. The innovative method of spraying water waste droplets into a pulsed discharge reactor was investigated. The generator provides a short voltage pulse width of 41 ns, a fast rise time of 24 ns, and a high repetition rate of 100 Hz required for the treatment. According to the authors, the advantage of the SOS-based system in water treatment remains in the high energy efficiency of up to 22% despite being an energy-consuming process. Additionally, streamer discharge produced by an SOS generator has been used for ozone synthesis in [53].

The sharp voltage pulse generated by the SOS generator is interesting for triggering applications. For instance, in [54] an SOS generator capable of generating up to 100 kV voltage on a 50 Ω load with a rise time of 1 ns and a duration of 4 ns was employed to trigger GTO thyristors in impact-ionization mode. The generator was powerful enough to provide the required dV/dt of up to 6 kV/ns. In this condition, the triggering of the series connected thyristors with a switching time of less than 300 ps was achieved using the SOS generator. Consequently, the thyristor stack has successfully conducted a discharge current of 43 kA peak amplitude and dI/dt of 120 kA/µs provided by the discharge circuit.

SOS generators have found applications in irradiation, particularly in the food industry, for preserving products over a long time. In [55], chicken meat samples were irradiated by the electron accelerator URT-1M-300 based on SOS diodes [44]. The effectiveness of the surface radiation disinfection process for bacterial insemination on chicken meat has been demonstrated. The low-energy e-beam used has the advantage of reducing the microorganisms on the surface without affecting the nutritional qualities of the overall product. This surface radiation disinfection method has further been used in [56], [57] to treat hen eggs. A reduction in chicken morbidity and hatching time was observed.

In engineering and medical applications, SOS-based X-ray imaging apparatus has gained significant interest due to their long lifetime, multi-kilohertz PRF, and the high reproducibility of their output parameters [10]. In particular, the pulsed X-ray diagnostics presented in [58] demonstrate a considerable reduction in radiation absorption while maintaining good image quality. More applications of SOS generators including pumping of gas lasers and high-power microwaves are discussed in [10].

To achieve this variety of applications, different methods are employed in the design of SOS systems. As outlined in Section 1.2.2, the SOS diode operation relies on a sequence of forward and reverse current pumping phases, leading to current interruption. The magnitude of the interrupted current and the diode switching speed determine the output voltage. Consequently, the key challenge lies in designing circuits capable of producing a forward current pulse ($<$1 µs, $\sim$100 A) followed by a short and high-amplitude reverse current ($\sim$100 ns, $\sim$1 kA). The upcoming sections explore various approaches to designing SOS circuits.

1.3.1 SOS pumped by a Marx generator

Incorporating a Marx generator as a current pumping source for SOS diodes has proven effective, as demonstrated in the pioneering experiment of the SOS effect [59] outlined in Section 1.2.2.2. The forward and reverse currents were provided by the discharge of the 150 kV Marx through the stray inductance and the diode [Figure 1.11 (a)]. The typical reverse current of duration 100–800 ns was interrupted by the diode in 50–80 ns, generating an output voltage of up to 450 kV (three times the Marx output) across the 100 Ω load.

However, in this configuration of the Marx generator, the diode faces very high current density in the forward pumping stage, as the amplitude of the forward current reaches 25 kA. Hence, significant energy loss may occur during this stage. To address this, multiple diodes are connected in parallel, up to 16 parallel branches, to handle the high current [10]. Moreover, the reverse current is slightly damped, leading to a 20% reduction compared to the forward current, resulting in an energy loss.

Further improvement of this approach consists in using a double pumping circuit based on a Marx generator proposed in [59]. In this configuration, the forward and reverse pumping currents are independently provided by the forward pumping capacitor C^+ and the Marx generator as illustrated in Figure 1.16. This approach aims to minimize losses and improve the control of circuit parameters. For instance, in the work described in [59], the reverse current amplitude is five times higher than the forward current amplitude. The author further mentions the importance of C^+ in this circuit, which determines the duration and amplitude of the forward current, as well as the timing of the Marx generator triggering which requires particular attention.

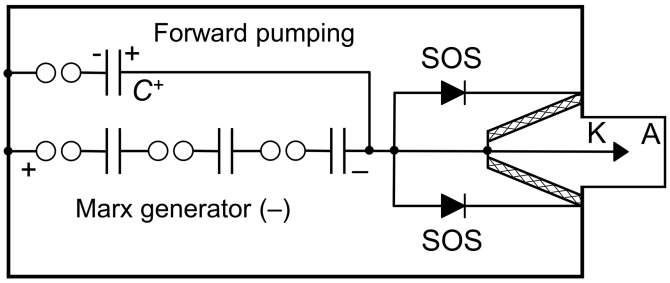

Figure 1.16: Circuit diagram of SOS diodes pumped by a Marx generator (Reproduced from [38]).

1.3.2 Circuits based on magnetic compression and pulse transformers

This second approach, employing Magnetic Pulse Compressors (MPCs), is widely used in all-solid-state SOS generators [10]. The typical circuit comprises a primary Thyristor or Transistor-based Charging Unit (TCU), which operates at a relatively low voltage, facilitating the use of semiconductor closing switches. TCU is followed by single or multiple MPCs stages,

which increase the voltage level a hundredfold. Finally, the SOS plays the role of the output power amplifier, switching current into the load. A diagram of such a generator with voltage and time ranges is presented in Figure 1.17.

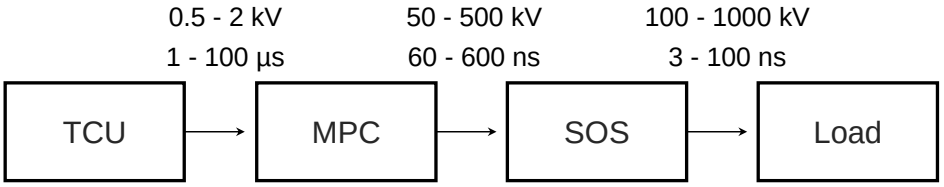

Figure 1.17: Diagram of solid-state SOS generator using a TCU and MPC stages [10].

1.3.2.1 Multi-stage magnetic pulse compressor (MPC) circuits

The most convenient circuit implementation [10] is shown in Figure 1.18. It can be visualized as a Fitch circuit to which a final compression and diode switching stage has been added [60]. The primary charging unit consists of the capacitor C1 and a solid-state closing switch T (e.g. thyristor). In the operation, when the switch T is closed, the energy from C1 is transferred, via the pulse transformer PT, to the secondary charging capacitors C2 and C3. One should note that C3 is charged to the opposite polarity of C2 through the winding of the magnetic switches MS^- and MS^+. The pulse transformer PT also operates as a magnetic switch and saturates once C2 and C3 are fully charged. When PT saturates, the voltage on C2 reverses, and both capacitors (C2 and C3) discharge together into capacitor C4, supplying the forward pumping current to the SOS. MS^+ saturates on this occasion as its applied voltage has doubled ($V_{C2} + V_{C3}$). When C4 is charged, the magnetic switch MS^- saturates in its turn and short circuits C2 and C3. Next, C4 discharges through the diode, providing the reverse pumping current which is ultimately switched off by the diode into the load R. A simplified chronogram of the circuit operation, with only one magnetic switch (MS^+) in the secondary is described in [60].

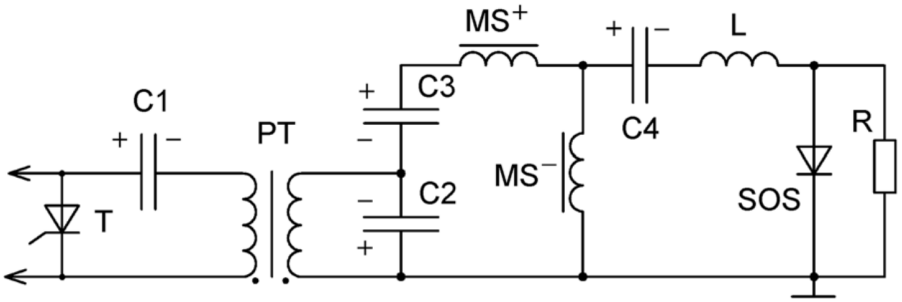

Figure 1.18: SOS generator circuit based on multistage compression [10].

This circuit approach was used in [48] to generate a voltage amplitude reaching 150 kV across a resistive load of 300 Ω. The forward, reverse, and cut-off current durations were

350 ns, 100 ns, and 30 ns respectively. The SM-3N generator [10] capable of producing up to 400 kV pulse amplitude with a duration of tens of nanoseconds is likewise based on this circuit.

Furthermore, in this circuit configuration, subsequent compression stages can be added before the SOS diode, to shorten the load current and voltage pulses. This principle makes it possible to achieve sub-nanosecond current interruption [10]. In addition, this circuit approach particularly fits generators with the primary C1 energy of tens to hundreds of joules, allowing the development of all-solid-state generators with megavolt output voltage [10]. However, the use of multiple magnetic compression stages reduces the overall energy efficiency of the system, which typically ranges between 20% and 40% according to the same author.

1.3.2.2 Circuit based on a single magnetic element

As described in [19], the simplest SOS pumping circuit is based on a single magnetic element combining the functions of a step-up pulse transformer and a magnetic switch. The circuit is depicted in Figure 1.19. In this arrangement, the energy stored in the capacitor C1 is transferred to the secondary capacitor C2 when the primary switch S1 is closed. The charging current of C2 corresponds to the forward pumping current of the SOS diode. Then, when the transformer saturates, the current reverses, and C2 discharges through the SOS while charging the intermediate inductive storage L. On completion of the reverse pumping phase, the diodes interrupt the current which is then directed to the load.

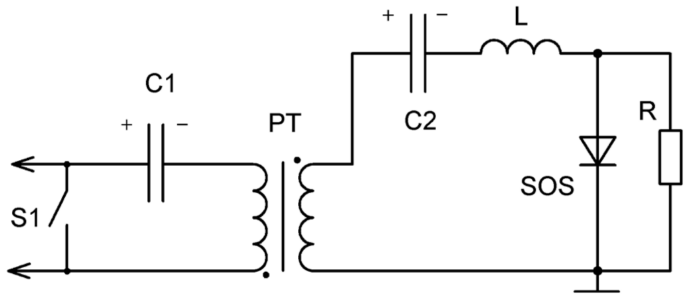

Figure 1.19: SOS pumping circuit with a single magnetic element [19].

This circuit has the advantage of being simple and compact. In addition, the use of a single MPC increases the overall energy efficiency reaching 70% as reported in [19] for a stored energy of about 15 J. Examples of numerous compact all-solid-state generators using this circuit architecture are outlined in [61], [62], with output voltages in the range of 1–50 kV and pulsed energy less than 1 J.

In generators with low primary voltage, the implementation of the all-solid-state using this circuit is possible [63]. However, in more powerful generators with pulse energy exceeding 10 J, the use of this simple circuit is severely limited by the primary closing switch. For

example, when the capacitor C1 of 1 µF with a stored energy of 20 J is being discharged for a duration of 350 ns (SOS forward pumping time), the switch S1 must conduct a current of amplitude 15 kA with a dI/dt of ∼150 kA/µs.

These requirements are tough for solid-state switches but can be met by spark gaps or pseudo-spark switches, enabling the use of such a simple SOS circuit at high energy. The URT accelerators [44] are mostly based on this circuit architecture, using a cold cathode thyratron primary switch to deliver voltages with amplitudes ranging from 200 kV to 1 MV. Even though the primary switch requirements are challenging for a high-energy all-solid-state approach, the promising results of single, series, and parallel thyristors triggered in the impact-ionization mode [19], [54], [64]–[67] open the prospect of such a possibility.

1.3.2.3 Linear Transformer Drive (LTD) SOS generator

The architecture of an LTD SOS generator is described in [68]. The author proposes a modular approach using low-inductive LTD (Figure 1.20) to produce nanosecond pulses. Each module uses a single magnetic element. The modules can be associated in parallel to increase the output voltage. Hence, the LTD circuit can be categorized as a multistage MPC circuit.

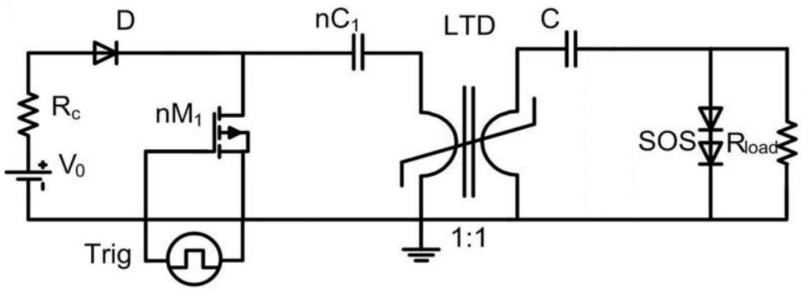

Figure 1.20: LTD SOS generator consisting of one module [68].

The operation of the circuit shown in Figure 1.20 is the same as described in Section 1.3.2.2 for the single magnetic element circuit. In the experiment described in [68], MOSFETs (nM_1) were used as the primary switch in the LTD. The forward and reverse pumping durations were recorded as 54 ns and 20 ns respectively. After the reverse current was cut off by the diode (430 A in 2 ns), the output voltage measured across a 106 Ω load showed an amplitude of 3.8 kV and a duration of 2 ns. The generator demonstrated its operational efficiency at a PRF of 4 MHz using a single module. However, the need for a substantial number of modules for high-voltage applications and the synchronous switching of the primary closing switches represent significant challenges.

1.3.3 SOS generator based on spiral generator

Also known as a vector inversion generator [69], the spiral generator is a very compact pulsed power generator capable of generating a megavolt voltage pulse of a triangular shape. The generator consists of a strip line wound on itself and insulated after each turn by a dielectric

of identical thickness to the line. A passive layer and an active layer are obtained, resulting in a twin spiral line with a common conductor terminated on an open circuit. The generator operation principle, based on wave propagation along the lines leading to voltage amplification, is developed in [70]–[72].

In [73], the authors introduce an SOS generator incorporating a spiral generator as its pumping circuit, supplying the forward and reverse currents of respectively 60–70 ns and 35–40 ns to the diode. Multiple SOS diodes were investigated. But particularly with the SOS-60-4, a 62 kV voltage pulse with 11 ns rise time and 30 ns duration was obtained on a 100 MΩ load with a diode switching current of 90 A. The generator circuit, built with all-solid-state components, exhibits impressive compactness, as depicted in Figure 1.21. However, this method is still in its early stages of study and the energy efficiency of the system is below 30 %.

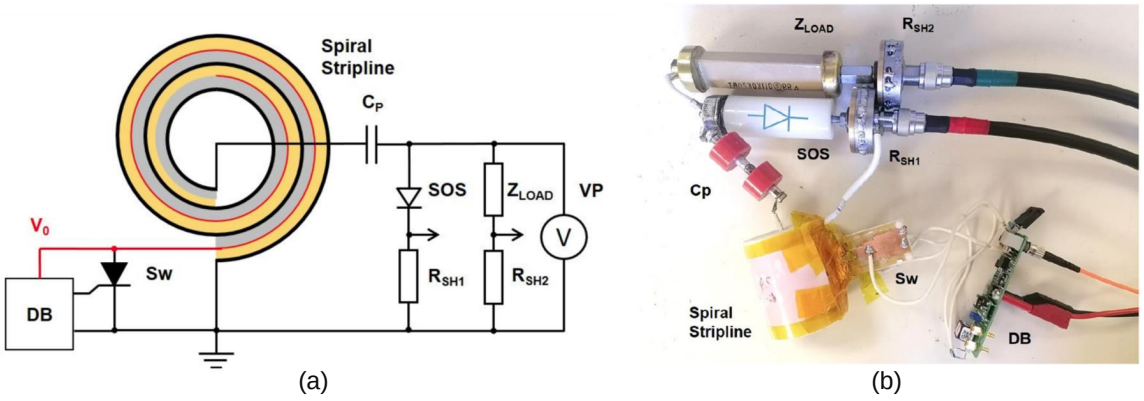

Figure 1.21: Spiral generator as pumping generator for SOS diodes: (a) circuit and (b) picture of the setup [73].

To summarize, several SOS generator configurations are possible, each having its advantages and drawbacks. For this thesis development, we have adopted the circuit featuring a single magnetic element (Figure 1.19), not only for its simplicity of implementation but, most importantly, for its greater energy efficiency. In this approach, a gas switch is used to meet the requirements of the primary closing switch, with a primary stored energy ranging from a few millijoules to tens of joules. A method for estimating the circuit element parameters is introduced in the next section.

1.4 Circuit design approach for an SOS generator

A methodology is proposed in this section for designing an SOS generator using the single-element circuit described in Section 1.3.2.2. For a better understanding, this design approach should be read in conjunction with Section 3.2.2 of Chapter 3 in which typical waveforms of the voltages across the load and the capacitive storage, as well as the current through the diode, are depicted and described.

The design starts with the definition of the generator output specifications and proceeds back towards the input. The specifications include the expected load voltage, the load current, and the pulse duration (FWHM). Taking these parameters as initial data, the required output and input energies are calculated, thereby enabling the generator components to be designed.

1.4.1 Energy estimation

The required energy at the load based on the output specifications is estimated as:

$$E_{Out} \approx V_{Out} \times I_{Out} \times t_p \times k_s \tag{1.1}$$

where V_{Out} and I_{Out} are the peak output voltage and current amplitudes, respectively, t_p is the pulse duration, and k_s is the pulse shape factor which is about 0.8 for bell-shape pulses. In the case of a resistive load R, this energy can be calculated as:

$$E_R \approx \frac{V_R^2}{R} \times t_p \times k_s \tag{1.2}$$

where V_R is the voltage across the load.

From the output energy, the required energy in the primary and secondary capacitors can be estimated by approximating the energy losses at the compression and switching stages. Considering the energy losses E_{L2} from capacitor C2 to the load R to be about 30%, the energy stored in C2 is estimated using:

$$E_R \approx 0.7 \times E_{C2} \tag{1.3}$$

E_{L2} represents the energy lost during the reverse pumping stage and, more importantly, during the diode switching phase. According to [10], the main energy loss (80% - 90%) in the diode occurs at the current cut-off stage. This loss depends on the number of elementary diodes in the stack, their surface area, the diode pumping condition, the load, the PRF, the cooling condition of the diodes, etc. Given the numerous variables involved, it is challenging to precisely predict the power loss of a diode at the designing stage. An E_{L2} value of between 20% and 60% can be used as a reasonable estimation to estimate the energy required in C2.

The energy losses in the primary switch and the transformer are estimated considering the energy transmitted from the primary to the secondary capacitor. For a spark gap primary switch, these losses can rise to 30%. Hence, the energy stored in C1 can be found using:

$$E_{C2} \approx 0.7 \times E_{C1} \tag{1.4}$$

The charging voltage of C2 (V_{C2}) is further estimated considering the overvoltage capability of the circuit using the opening switch. This overvoltage results from the fast switching of the current by the diode, since the voltage generated is proportional to the rate of change of the current ($V \sim L\frac{dI}{dt}$). The overvoltage coefficient k_{ov} defined in [10] is used to evaluate the

ratio of the secondary and load voltages:

$$V_{C2} \approx \frac{V_R}{k_{ov}} \tag{1.5}$$

A typical overvoltage coefficient of SOS diodes is $k_{ov} = 3$ according to [37]. However, one should note that the power loss in the diode at the current switching stage increases with the overvoltage coefficient [10]. Moreover, the actual output voltage is difficult to predict, as it is highly dependent on the load and the circuit's stray capacitances and inductances. For these reasons, a $k_{ov} \leq 2$ should be considered in practice.

Knowing the charging voltage of C2, its capacitance can be further determined using:

$$E_{C2} = \frac{1}{2} \times C2 \times V_{C2}^2 \tag{1.6}$$

With the voltage, capacitance, and energy required at the secondary of the transformer calculated, the parameters of the primary and pulse transformers can be further determined.

1.4.2 Primary circuit and pulse transformer design

Before going into the details of the transformer and primary circuit parameters, it is necessary to point out a few important considerations. As reported in [10], to achieve a current switching time of 0.5–20 ns, the forward pumping duration t^+ should be in the range of 40–600 ns, and the reverse pumping duration in the range of 10–150 ns. The equivalent inductance of the primary circuit must be minimized in order to provide such a short time of t^+. Therefore, a single-turn primary winding is typically used in SOS generators featuring a single magnetic element.

When the primary winding is fixed, the number of turns of the secondary winding is tuned to obtain a proper transformation ratio, taking into account the charging voltage of the primary capacitor and the maximum voltage across C2. In addition, the two capacitors C1 and C2 should be matched for an efficient energy transfer through the transformer:

$$C1 = k_{PT}^2 \times C2 \tag{1.7}$$

where k_{PT} corresponds to the ratio of the number of turns of the secondary and primary windings of the transformer. Under these conditions, the relation between the two voltages (V_{C1} and V_{C2}) can be expressed using:

$$V_{C1} = \frac{V_{C2}}{k_{PT}} \times \sqrt{\frac{E_{C1}}{E_{C2}}} \tag{1.8}$$

Once the primary capacitance C1 and voltage V_{C1} are defined, the next step is to calculate the parameters of the equivalent circuit of the pulse transformer.

1.4.2.1 Parameters of the equivalent circuit when referring to the primary side of the transformer

The equivalent circuit diagram when referring to the primary side of the transformer shown in Figure 1.22 represents the operation during the transfer of energy from the primary to the secondary circuit. A detailed description of the circuit with its analytical expressions can be found in [74].

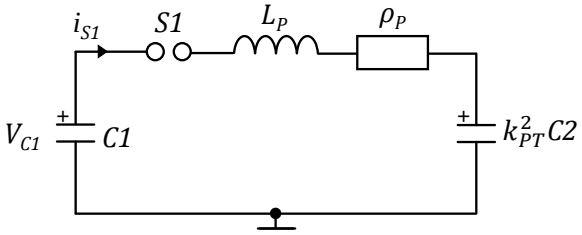

Figure 1.22: Simplified circuit while referring to the primary side of the transformer.

The equivalent capacitor C_p, inductance L_p and resistance ρ_p shown in Figure 1.22 are determined using the following equations:

$$C_p = \frac{C1}{2} \tag{1.9}$$

$$L_p = \frac{t^{+2}}{\pi^2 \times C_p} \tag{1.10}$$

$$\rho_p = \sqrt{\frac{L_p}{C_p}} \tag{1.11}$$

The equivalent capacitance C_p expressed in Equation 1.9, is the result of the two capacitors $C1$ and $k_{PT}^2 \times C2 = C1$ in series.

Next, the specifications of the primary closing switch are determined using the primary side parameters:

- maximum current amplitude:

$$I_{S1} = \frac{V_{C1}}{\rho_p} \tag{1.12}$$

- rate of rise of current:

$$\frac{dI_{S1}}{dt} = \frac{V_{C1}}{L_p} \tag{1.13}$$

In addition to these current parameters, the switch must withstand the charging voltage of C1 which can rise to several tens of kilovolts. However, this is not critical for the primary gas switches used in this work, which are based on spark gaps and thyratron.

1.4.2.2 Saturable pulse transformer (SPT)

An important element of the circuit is SPT, which is used not only to step up the primary capacitor voltage but also as a magnetic switch when its cores become saturated. A detailed study of the transformer based on different magnetic cores is presented in Chapter 3. The main characteristics of the core material, including the hysteresis loop, the relative permeability, and the size, are of great importance for the transformer design.

The hysteresis loop of a magnetic material is presented in Figure 1.23, indicating the saturation flux density B_{sat}, the residual magnetic flux density B_r, the maximum induction swing ΔB_{max}, and the coercive force H_c. A description of a magnetic core hysteresis and its related parameters can be found in [75].

Assuming the core is reset ($B_0 = 0$), when the discharge of the primary energy occurs, the flow of the primary current through the transformer winding generates a magnetic flux through the cross-sectional area S_c of the transformer core. The expression of the magnetic flux is:

$$\Phi_B = \int_{S_c} \vec{B}\,\vec{ds} \approx \Delta B \times S_c \tag{1.14}$$

where ΔB is the induction swing, corresponding to the change in the magnetic flux density of the magnetic material. For a reversely pre-magnetized material ($B_0 = -B_{sat}$), the maximum induction swing is $\Delta B_{max} = 2B_{sat}$.

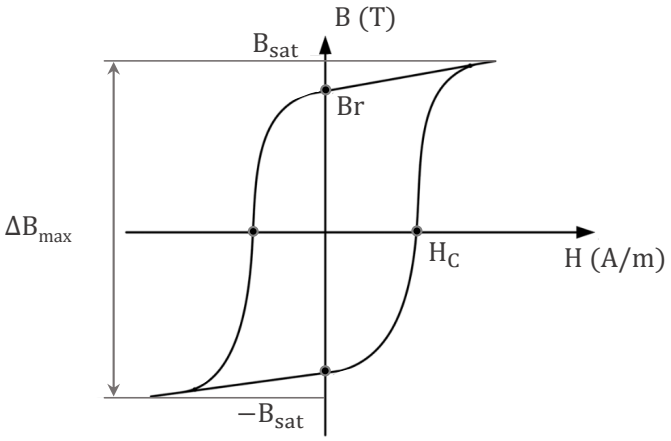

Figure 1.23: Hysteresis loop of a magnetic core.

On the other hand, the time-varying magnetic flux in the material, according to Faraday's law, produces an electromotive force across the secondary winding of the transformer:

$$N \times \frac{\partial \phi_B}{\partial t} = -V(t) \tag{1.15}$$

where N corresponds to the number of turns of the transformer secondary winding. Integrating Equation 1.15, from the primary capacitor discharge ($t = 0$) to the saturation time of the

core ($t = T_{sat}$), the magnetic flux is expressed as:

$$\Phi_B = -\frac{1}{N}\int_0^{T_{sat}} V(t)\,dt \tag{1.16}$$

Assuming the maximum voltage on C2 (V_{max}) is reached when the core saturates at $t = T_{sat}$, and considering the typical shape of the capacitor charging voltage as depicted in Figure 1.24, Equation 1.16 becomes:

$$\Phi_B = -\frac{1}{N}\int_0^{t_{sat}} V(t)\,dt = -\frac{V_{max} \times T_{sat}}{2 \times N} \tag{1.17}$$

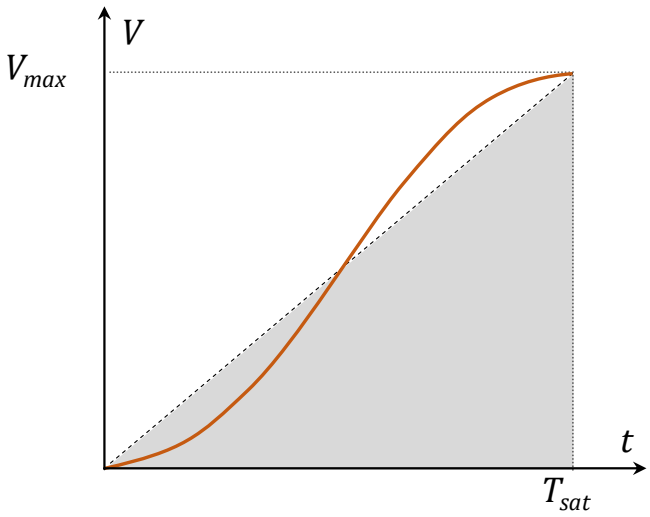

Figure 1.24: Voltage-time product (Reproduced from [76]).

Equating the two Equations 1.14 and 1.17, without regard to the voltage polarity, the voltage-time product required for the saturation of the transformer core is:

$$V_{max} \times T_{sat} = 2 \times N \times S_c \times \Delta B \tag{1.18}$$

From Equation 1.18, the core material cross-sectional area S_c can be determined. It should be noted that the material cross-section is usually less than the geometrical cross-section due to the interlaminar insulation of the core. In fact, the cores are generally made up of ribbons of thin metal sheets stacked in layers to reduce eddy current losses. The stacking factor or packing factor k_c represents the ratio of the effective cross-sectional area of the core to its geometrical cross-section.

$$k_c = \frac{S_c}{S_g} \tag{1.19}$$

For better cooling, several cores should be used instead of a bulky single core. Figure 1.25

depicts a toroidal magnetic core whose geometrical cross-section can be determined using:

$$S_g = h \times \frac{OD - ID}{2} \tag{1.20}$$

where OD is the outer diameter, ID is the inner diameter, and h is the height of the core.

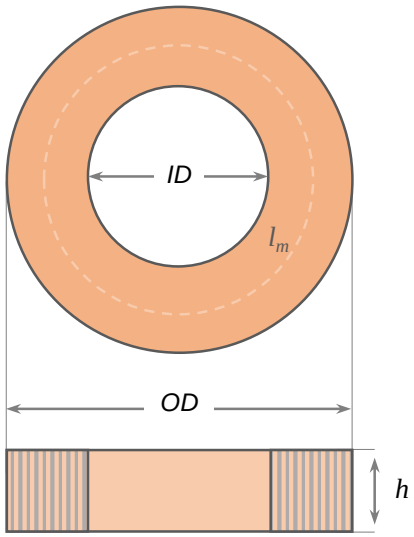

Figure 1.25: Schematic of a toroidal core showing the outer diameter OD, inner diameter ID, height h, and mean magnetic path length l_m of the core.

1.4.3 Magnetic switch property and secondary circuit parameters after core saturation

As mentioned earlier, the transformer operates as a magnetic switch when it saturates. Equation 1.20 describes the winding inductance of the unsaturated transformer.

$$L_w = \frac{\mu_0 \times \mu_r \times S_w \times N^2}{l_m} \tag{1.21}$$

where μ_0 and μ_r are the vacuum permeability and the material relative permeability, respectively, S_w is the geometrical cross-sectional area of the winding around the core, and l_m is the mean magnetic field path length of the core which can be calculated for a toroidal core (Figure 1.25) using:

$$l_m = \pi \times \frac{OD + ID}{2} \tag{1.22}$$

The switching property of the magnetic material is achieved through the change of the relative magnetic permeability over time, under the action of the applied magnetic field H. The change in the magnetic permeability leads to a change in inductance (Equation 1.21). Before the core saturation, the increase in the magnetic field H leads to a significant increase

in the induction B (Figure 1.23). When the core saturates, the increase in the magnetic field does not affect the induction. The relative permeability $\mu_{r\,sat}$ of the saturated core is close to 1. The ratio of unsaturated to saturated inductances can be calculated when the material permeability is given, as:

$$\frac{L_w}{L_{w\,sat}} = \frac{\mu_r}{\mu_{r\,sat}} \tag{1.23}$$

where $L_{w\,sat}$ is the saturated inductance of the winding. As expressed in Equation 1.23, the magnetic switch takes advantage of the change in permeability, hence, the difference between μ_r and $\mu_{r\,sat}$ must be as large as possible for the SPT cores.

At saturation, the magnetic switch decouples the primary and secondary circuits. Therefore, the duration and amplitude of the C2 discharge current are mainly defined by the secondary circuit parameters. The duration of the reverse current can be estimated using:

$$t^- = \frac{\pi}{2} \times \sqrt{L_{sec} \times C2} \tag{1.24}$$

where L_{sec} corresponds to the saturated inductance of the transformer's secondary winding along with the parasitic inductance of the circuit.

The equivalent resistance ρ_s of the secondary discharge circuit and the peak reverse current I_s are estimated using Equations 1.25 and 1.26:

$$\rho_s = \sqrt{\frac{L_{sec}}{C2}} \tag{1.25}$$

$$I_s = \frac{V_{C2}}{\rho_s} \tag{1.26}$$

As described in Section 1.2.2.2, during the reverse current conduction phase, a high electric field develops in the $p-$region of the SOS diode leading to the current cut-off. However, it is hard to predict the exact moment when the current switching occurs. This depends on several parameters, including forward and reverse pumping charges, the current density, the diode type and its doping profile, etc. Based on experimental data, the peak current cut off by the SOS diode can be estimated as:

$$I^- = 0.8 \times I_s \tag{1.27}$$

Furthermore, the peak load current depends on the load. In the case of a resistive load R, for example, the output current (I_R) will be maximum, in the order of I^- for low load values (R of about ten times the on-state resistance of the diode, which is of the order of a few Ohms depending on the number of elementary diodes in the stack), whereas for high load values (open circuit), I_R would be minimal. Nevertheless, one can approximate the load current to half the I^- for design considerations:

$$I_R = 0.5 \times I^- \tag{1.28}$$

To summarize, the design method proposed is by no means complete, but it provides an essential basis for an SOS generator design. The design often requires several iterations to reach a compromise on the specifications and the available components. Although additional calculations and simulations are necessary to optimize the design, a few recommendations could be taken into account. A secondary short circuit experiment should be performed to validate the circuit parameters such as forward and reverse current durations, transformer saturation time, induction swing of the magnetic material, transformer efficiency, etc., before inserting the diodes into the circuit. This experiment is described in Chapter 3 and Chapter 4 for the test benches of 10 J and 40 J, respectively. To optimize transformer operation in saturation, a pre-magnetizing circuit can be used. This circuit is also covered in the two above-mentioned chapters. The choice of the diode and the number of components to be assembled in series/parallel must be carried out considering the peak diode current and the expected load voltage. Chapter 2 provides diode selection criteria and discusses the necessity of diode arrays for high-current and high-voltage applications. Particular attention must also be paid to diode and transformer cooling, especially for frequency and continuous operation.

1.5 Conclusion

This first chapter highlights semiconductor opening switches and their advantages for high-power nanosecond switching. Controlled semiconductor switches are widely used in pulsed power generators, though their switching time and power are in the range of hundreds of nanoseconds and a few megawatts, respectively. The SOS diode, with its particular doping profile characterized by a deep aluminum diffusion, appears to be the most suitable solid-state opening switch for generating gigawatt-level nanosecond high-voltage pulses. Their use in numerous generators for pulsed power applications is discussed, and the efficiency of such generators no longer needs to be demonstrated. However, given the lack of SOS diode manufacturers, this thesis aims to investigate alternative OTS diodes. Therefore, dedicated experimental test benches are required for the study. Additionally, this chapter discusses the circuit approach, highlighting the advantages and limitations of each of the main SOS generator circuit architectures. For the development within the framework of this thesis, a circuit based on a single magnetic element is adopted because of its higher energy efficiency. A design method for the circuit is proposed. This method will be applied in the following chapters to develop low, medium, and high-energy test benches dedicated to power diode investigation. The research methodology starts with the evaluation of various types of diodes at low energies to refine the selection criteria for diodes to be tested on higher-energy benches. The selected promising OTS opening switches will be implemented in a 500 kV pulsed power generator prototype for e-beam sterilization application.

1.6 References

[1] J. Lehr and P. Ron, *Foundations of Pulsed Power Technology*. 2017, ISBN: 9781118628393. DOI: 10.1002/9781118886502.

[2] S. T. Pai and Q. Zhang, *Introduction to High Power Pulse Technology*, 1995. DOI: 10.1142/2311.

[3] G. A. Mesyats, *Pulsed Power*. Boston, MA: Springer US, 2005, ISBN: 978-0-306-48653-1. DOI: 10.1007/b116932.

[4] J. Bac, "Contribution à l'étude et à la réalisation de commutateurs et de générateurs haute tension transitoires.," Physique [physics]. Université de Pau et des Pays de l'Adour, Français. NNT : . tel-00009770v2, Ph.D. dissertation, 2005. [Online]. Available: https://theses.hal.science/tel-00009770v2.

[5] I. Boscolo, G. Brautti, R. Coisson, M. Leo, and A. Luches, "Tesla transformer accelerator for the production of intense relativistic electron beams," *Review of Scientific Instruments*, vol. 46, no. 11, pp. 1535–1538, 1975, ISSN: 00346748. DOI: 10.1063/1.1134098.

[6] G. A. Mesyats, S. D. Korovin, A. V. Gunin, *et al.*, "Repetitively pulsed high-current accelerators with transformer charging of forming lines," *Laser and Particle Beams*, vol. 21, no. 2, pp. 197–209, 2003, ISSN: 02630346. DOI: 10.1017/S0263034603212076.

[7] S. D. Korovin, V. V. Rostov, S. D. Polevin, *et al.*, "Pulsed power-driven high-power microwave sources," *Proceedings of the IEEE*, vol. 92, no. 7, pp. 1082–1094, 2004, ISSN: 00189219. DOI: 10.1109/JPROC.2004.829020.

[8] C. Lamarche, "Compréhension de l'efficacité bactéricide de différentes technologies de haute puissance pulsée.," 2019, Microbiologie, Université de Toulouse 3. [Online]. Available: http://www.theses.fr/2019TOU30117/document.

[9] H. Bluhm, *Pulsed Power Systems*. 2003, pp. 277–285, ISBN: 9783540261377. DOI: 10.1007/3-540-34662-7.

[10] S. N. Rukin, "Pulsed power technology based on semiconductor opening switches: A review," *Review of Scientific Instruments*, vol. 91, no. 1, p. 011 501, Jan. 2020, ISSN: 0034-6748. DOI: 10.1063/1.5128297.

[11] A. Guenther and M. Kristiansen, *Opening Switches*, 1st ed., A. H. Guenther, M. Kristiansen, and T. Martin, Eds. Boston, MA: Springer New York, NY, 1987, ISBN: 978-1-4613-1929-0. DOI: 10.1007/978-1-4613-1929-0. [Online]. Available: https://link.springer.com/10.1007/978-1-4613-1929-0.

[12] J. D. Plummer, D. M. Deal, and P. B. Griffin, *Silicon VLSI TECHNOLOGY Fundamentals, Practice and Modeling*. Prentice Hall, 2000, ISBN: 0-13-085037-3.

[13] J. Lutz, H. Schlangenotto, U. Scheuermann, and R. De Doncker, *Semiconductor Power Devices*. Berlin, Heidelberg: Springer Berlin Heidelberg, 2011, ISBN: 978-3-642-11124-2. DOI: 10.1007/978-3-642-11125-9.

[14] J. D. Plummer and P. B. Griffin, *Integrated Circuit Fabrication*. Cambridge University Press, Nov. 2023, ISBN: 9781009303606. DOI: 10.1017/9781009303606.

[15] B. J. Baliga, *Fundamentals of power semiconductor devices, Second edition*. 2018, pp. 1–1086, ISBN: 9783319939889. DOI: 10.1007/978-3-319-93988-9.

[16] A. Bryant, E. Santi, J. Hudgins, and P. Palmer, "Thyristors," in *Power Electronics Handbook*, Elsevier, 2011, pp. 91–116, ISBN: 9780123820365. DOI: 10.1016/B978-0-12-382036-5.00006-9.

[17] S. M. Sze and K. K. Ng, *Physics of Semiconductor Devices*. Wiley, Oct. 2006, ISBN: 9780471143239. DOI: 10.1002/0470068329.

[18] A. I. Gusev, S. K. Lyubutin, S. N. Rukin, B. G. Slovikovsky, and S. N. Tsyranov, "High-current pulse switching by thyristors triggered in the impact-ionization wave mode," *Instruments and Experimental Techniques*, vol. 60, no. 4, pp. 545–550, 2017, ISSN: 00204412. DOI: 10.1134/S0020441217030204.

[19] A. I. Gusev, S. K. Lyubutin, A. V. Ponomarev, S. N. Rukin, and B. G. Slovikovsky, "Semiconductor opening switch generator with a primary thyristor switch triggered in impact-ionization wave mode," *Review of Scientific Instruments*, vol. 89, no. 11, p. 114 702, Nov. 2018, ISSN: 0034-6748. DOI: 10.1063/1.5052530.

[20] S. Scharnholz, V. Brommer, G. Buderer, and E. Spahn, "High-power MOSFETs and fast-switching thyristors utilized as opening switches for inductive storage systems," *IEEE Transactions on Magnetics*, vol. 39, no. 1, pp. 437–441, Jan. 2003, ISSN: 0018-9464. DOI: 10.1109/TMAG.2002.806395.

[21] P. Dedié, V. Brommer, and S. Scharnholz, "Twenty-stage toroidal XRAM generator switched by countercurrent thyristors," *IEEE Transactions on Plasma Science*, vol. 39, no. 1 PART 1, pp. 263–267, 2011, ISSN: 00933813. DOI: 10.1109/TPS.2010.2055168.

[22] A. Sitzman, D. Surls, J. Mallick, and E. Dierks, "Operational limits of a commercial gate turn-off thyristor for inductive-store systems," *IEEE Transactions on Plasma Science*, vol. 39, no. 1 PART 1, pp. 316–321, 2011, ISSN: 00933813. DOI: 10.1109/TPS.2010.2087774.

[23] Q. Liu, H. B. Pu, and X. Wang, "Ultra-high voltage 4H-SiC gate turn-off thyristor for low switching time," *Chinese Physics B*, vol. 28, no. 12, p. 127 201, Nov. 2019, ISSN: 1674-1056. DOI: 10.1088/1674-1056/ab4e89.

[24] P. Dedié, V. Brommer, and S. Scharnholz, "Experimental realization of an eight-stage XRAM generator based on ICCOS Semiconductor opening switches, fed by a magneto-dynamic storage system," *IEEE Transactions on Magnetics*, vol. 45, no. 1, pp. 266–269, 2009, ISSN: 00189464. DOI: 10.1109/TMAG.2008.2008418.

[25] T. F. Podlesak, J. A. McMurray, and J. L. Carter, "Solid state switch utilizing GTOs in series," *Proceedings of the Intersociety Energy Conversion Engineering Conference*, vol. 1, pp. 651–655, 1989, ISSN: 0146955X. DOI: 10.1109/iecec.1989.74535.

[26] L. Redondo and J. F. Silva, *Solid state pulsed power electronics*, Third Edit. Elsevier Inc., 2011, pp. 669–707, ISBN: 9780123820365. DOI: 10.1016/B978-0-12-382036-5.00026-4.

[27] M. J. Barnes, W. Bartmann, F. Burkart, *et al.*, "Future circular collider injection and extraction kicker topologies and solid state generators," *Physical Review Accelerators and Beams*, vol. 22, no. 7, p. 071 001, Jul. 2019, ISSN: 2469-9888. DOI: 10.1103/PhysRevAccelBeams.22.071001. [Online]. Available: https://link.aps.org/doi/10.1103/PhysRevAccelBeams.22.071001.

[28] O. Liebfried, V. Brommer, and S. Scharnholz, "Development of XRAM generators as inductive power sources for very high current pulses," *Digest of Technical Papers-IEEE International Pulsed Power Conference*, pp. 2–7, 2013. DOI: 10.1109/PPC.2013.6627504.

[29] J. L. Moll, S. Krakauer, and R. Shen, "P-N Junction Charge-Storage Diodes," *Proceedings of the IRE*, vol. 50, no. 1, pp. 43–53, 1962, ISSN: 00968390. DOI: 10.1109/JRPROC.1962.288273.

[30] J. L. Moll and S. A. Hamilton, "Physical Modeling of the Step Recovery Diode for Pulse and Harmonic Generation Circuits," *Proceedings of the IEEE*, vol. 57, no. 7, pp. 1250–1259, 1969, ISSN: 15582256. DOI: 10.1109/PROC.1969.7229.

[31] I. V. Grekhov, V. M. Efanov, A. F. Kardo-Sysoev, and S. V. Shenderey, "Power drift step recovery diodes (DSRD)," *Solid State Electronics*, vol. 28, no. 6, pp. 597–599, 1985, ISSN: 00381101. DOI: 10.1016/0038-1101(85)90130-3.

[32] S. K. Lyubutin, G. Mesyats, S. Rukin, B. Slovikovskii, and A. Turov, "New solid state opening switches for repetitive pulsed power technology," in *11th International Conference on High-Power Particle Beams*, 1996, pp. 135–138.

[33] I. V. Grekhov and G. A. Mesyats, "Physical basis for high-power semiconductor nanosecond opening switches," *IEEE Transactions on Plasma Science*, vol. 28, no. 5, pp. 1540–1544, 2000, ISSN: 00933813. DOI: 10.1109/27.901229.

[34] I. V. Grekhov and G. A. Mesyats, "Nanosecond semiconductor diodes for pulsed power switching," *Physics-Uspekhi*, vol. 48, no. 7, pp. 703–712, Jul. 2005, ISSN: 1063-7869. DOI: 10.1070/PU2005v048n07ABEH002471.

[35] S. A. Darznek, G. A. Mesyats, S. N. Rukin, and S. N. Tsiranov, "Theoretical model of the SOS effect," *1996 11th International Conference on High-Power Particle Beams*, pp. 1241–1244, 1996.

[36] V. M. Efanov, A. Kardo-Sysoev, M. Larionov, I. Tchashnikov, P. Yarin, and A. Kriklenko, "Powerful semiconductor 80 kV nanosecond pulser," in *Digest of Technical Papers. 11th IEEE International Pulsed Power Conference (Cat. No.97CH36127)*, vol. 2, 1997, 985–987 vol.2. DOI: 10.1109/PPC.1997.674522.

[37] S. A. Darznek, S. N. Rukin, and S. N. Tsiranov, "Effect of structure doping profile on the current switching-off process in power semiconductor opening switches," *Technical Physics*, vol. 45, no. 4, pp. 436–442, 2000, ISSN: 10637842. DOI: 10.1134/1.1259650.

[38] Y. A. Kotov, G. A. Mesyats, S. N. Rukin, A. L. Filatov, and S. K. Lyubutin, "Novel nanosecond semiconductor opening switch for megavolt repetitive pulsed power technology: Experiment and applications," *IEEE International Pulsed Power Conference - Digest of Technical Papers*, vol. 1, pp. 134–139, 1993, ISSN: 1996756X. DOI: 10.1117/12.204997.

[39] A. Engelko and H. Bluhm, "Optimal design of semiconductor opening switches for use in the inductive stage of high power pulse generators," *Journal of Applied Physics*, vol. 95, no. 10, pp. 5828–5836, 2004, ISSN: 00218979. DOI: 10.1063/1.1707207.

[40] I. V. Grekhov and A. S. Kyuregyan, "Formation of the space charge region in diffusion p-n junctions under high-density current interruption," *Technical Physics*, vol. 50, no. 7, pp. 904–913, Jul. 2005, ISSN: 1063-7842. DOI: 10.1134/1.1994972.

[41] W. Jiang, K. Yatsui, K. Takayama, *et al.*, "Compact solid-state switched pulsed power and its applications," *Proceedings of the IEEE*, vol. 92, no. 7, pp. 1180–1195, 2004, ISSN: 00189219. DOI: 10.1109/JPROC.2004.829003.

[42] A. V. Ponomarev, S. N. Rukin, and S. N. Tsyranov, "Investigation of the process of voltage distribution over elements of a high-power semiconductor current interrupter," *Technical Physics Letters*, vol. 27, no. 10, pp. 857–859, 2001, ISSN: 10637850. DOI: 10.1134/1.1414555.

[43] A. I. Bushlyakov, A. V. Ponomarev, S. N. Rukin, B. G. Slovikovsky, and S. P. Timoshenkov, "A Megavolt Nanosecond Generator with a Semiconductor Opening Switch," *Instruments and Experimental Techniques*, vol. 45, no. 2, pp. 213–219, 2002, ISSN: 00204412. DOI: 10.1023/A:1015364617814.

[44] S. Y. Sokovnin and M. E. Balezin, "Repetitive nanosecond electron accelerators type URT-1 for radiation technology," *Radiation Physics and Chemistry*, vol. 144, no. August 2017, pp. 265–270, Mar. 2018, ISSN: 0969806X. DOI: 10.1016/j.radphyschem.2017.08.023.

[45] S. N. Rukin, G. Mesyats, S. Darznek, *et al.*, "SOS-based pulsed power: development and applications," in *Digest of Technical Papers. 12th IEEE International Pulsed Power Conference. (Cat. No.99CH36358)*, vol. 1, IEEE, 1999, pp. 153–156, ISBN: 0-7803-5498-2. DOI: 10.1109/PPC.1999.825435.

[46] O. Krause, H. Ryssel, and P. Pichler, "Determination of aluminum diffusion parameters in silicon," *Journal of Applied Physics*, vol. 91, no. 9, pp. 5645–5649, 2002, ISSN: 00218979. DOI: 10.1063/1.1465501.

[47] G. Rattmann, P. Pichler, and T. Erlbacher, "On a Novel Source Technology for Deep Aluminum Diffusion for Silicon Power Electronics," *Physica Status Solidi (A) Applications and Materials Science*, vol. 216, no. 17, pp. 7–12, 2019, ISSN: 18626319. DOI: 10.1002/pssa.201900167.

[48] Y. Teramoto, H. Urakami, S. Katsuki, T. Namihira, and H. Akiyama, "Semiconductor opening switch based repetitive pulsed power generator," in *Conference Record of the Twenty-Fifth International Power Modulator Symposium, 2002 and 2002 High-Voltage Workshop.*, IEEE, 2002, pp. 210–213, ISBN: 0-7803-7540-8. DOI: 10.1109/MODSYM.2002.1189453.

[49] M. Gundersen, A. Kuthi, P. Gabrielsson, and M. Behrendand, "Nanosecond pulse generator using a fast recovery diode," in *Conference Record of the Twenty-Sixth International Power Modulator Symposium, 2004 and 2004 High-Voltage Workshop.*, IEEE, 2004, pp. 603–606, ISBN: 0-7803-8586-1. DOI: 10.1109/MODSYM.2004.1433649.

[50] A. I. Gusev, M. S. Pedos, S. N. Rukin, S. P. Timoshenkov, and S. N. Tsyranov, "A 6 GW nanosecond solid-state generator based on semiconductor opening switch," *Review of Scientific Instruments*, vol. 86, no. 11, 2015, ISSN: 10897623. DOI: 10.1063/1.4936295.

[51] P. V. Vasil'ev, S. K. Lyubutin, M. S. Pedos, *et al.*, "A nanosecond SOS-generator with a 20-kHz pulse repetition rate," *Instruments and Experimental Techniques*, vol. 53, no. 6, pp. 830–835, Nov. 2010, ISSN: 0020-4412. DOI: 10.1134/S0020441210060114.

[52] T. Sugai, W. Liu, A. Tokuchi, W. Jiang, and Y. Minamitani, "Influence of a Circuit Parameter for Plasma Water Treatment by an Inductive Energy Storage Circuit Using Semiconductor Opening Switch," *IEEE Transactions on Plasma Science*, vol. 41, no. 4, pp. 967–974, Apr. 2013, ISSN: 0093-3813. DOI: 10.1109/TPS.2013.2251359.

[53] K. Takaki, I. Yagi, S. Mukaigawa, T. Fujiwara, and T. Go, "Ozone synthesis using streamer discharge produced by nanoseconds pulse voltage under atmospheric pressure," *PPC2009 - 17th IEEE International Pulsed Power Conference*, no. December 2015, pp. 989–993, 2009. DOI: 10.1109/PPC.2009.5386169.

[54] A. I. Gusev, S. K. Lyubutin, V. Patrakov, *et al.*, "GTO Like Thyristors Triggered in Impact-Ionization Wave Mode," in *2019 IEEE Pulsed Power & Plasma Science (PPPS)*, vol. 2019-June, IEEE, Jun. 2019, pp. 1–4, ISBN: 978-1-5386-7969-2. DOI: 10.1109/PPPS34859.2019.9009695.

[55] R. A. Vazirov, S. Y. Sokovnin, A. S. Krivonogova, and A. G. Isaeva, "Radiation surface antimicrobial processing of poultry meat and by-products using the nanosecond low-energy electron beam," *Radiation Physics and Chemistry*, vol. 217, p. 111 528, Apr. 2024, ISSN: 0969-806X. DOI: 10.1016/j.radphyschem.2024.111528.

[56] S. Y. Sokovnin, "An electron beam technology of surface disinfection of the packed egg," *Food and Bioproducts Processing*, vol. 127, pp. 276–281, May 2021, ISSN: 09603085. DOI: 10.1016/j.fbp.2021.03.009.

[57] S. Y. Sokovnin and M. E. Balezin, "Surface irradiation installation for eggs based on URT-0,5M accelerator," *Radiation Physics and Chemistry*, vol. 196, p. 110 137, Apr. 2022, ISSN: 0969806X. DOI: 10.1016/j.radphyschem.2022.110137.

[58] A. A. Komarskiy, A. S. Chepusov, V. L. Kuznetsov, S. R. Korzhenevskiy, S. P. Niculin, and S. O. Cholakh, "Reducing Radiation Dose by Using Pulse X-Ray Apparatus," *Journal of Biosciences and Medicines*, vol. 02, no. 02, pp. 17–21, 2014, ISSN: 2327-5081. DOI: 10.4236/jbm.2014.22003.

[59] Y. A. Kotov, G. A. Mesyats, S. N. Rukin, *et al.*, "Megavolt nanosecond 50 kW average power all solid state driver for commercial applications," *Digest of Technical Papers-IEEE International Pulsed Power Conference*, vol. 2, pp. 1227–1230, 1995. DOI: 10.1109/ppc.1995.599782.

[60] A. B. J. M. Driessen, F. J. Beckers, T. Huiskamp, and A. J. Pemen, "Design and Implementation of a Compact 20-kHz Nanosecond Magnetic Pulse Compression Generator," *IEEE Transactions on Plasma Science*, vol. 45, no. 12, pp. 3288–3299, 2017, ISSN: 00933813. DOI: 10.1109/TPS.2017.2771275.

[61] A. B. J. M. Driessen, E. J. M. van Heesch, T. Huiskamp, F. J. C. M. Beckers, and A. J. M. Pemen, "Compact Pulse Topology for Adjustable High-Voltage Pulse Generation Using an SOS Diode," *IEEE Transactions on Plasma Science*, vol. 42, no. 10, pp. 3083–3088, Oct. 2014, ISSN: 0093-3813. DOI: 10.1109/TPS.2014.2314686.

[62] T. Sugai, W. Jiang, and A. Tokuchi, "Influence of forward pumping current on current interruption by semiconductor opening switch," *IEEE Transactions on Dielectrics and Electrical Insulation*, vol. 22, no. 4, pp. 1971–1975, 2015, ISSN: 10709878. DOI: 10.1109/TDEI.2015.004989.

[63] T. Sugai, A. Tokuchi, and W. Jiang, "Experimental characteristics of semiconductor opening switch diode," *Proceedings of the 2014 IEEE International Power Modulator and High Voltage Conference, IPMHVC 2014*, pp. 105–107, 2015. DOI: 10.1109/IPMHVC.2014.7287218.

[64] I. Lavrinovich, A. I. Gusev, S. Bland, *et al.*, "2-kV Thyristor Triggered in Impact-Ionization Wave Mode by a Solid-State Spiral Generator," *IEEE Transactions on Plasma Science*, vol. 50, no. 10, pp. 3443–3451, Oct. 2022, ISSN: 0093-3813. DOI: 10.1109/TPS.2022.3187213.

[65] E. Shahriari, T. Maysonnave, A. I. Gusev, A. S. de Ferron, and L. Pecastaing, "A Study of a 5.2-kV/100-mm Thyristor Triggered in Impact-Ionization Mode Toward Fast High-Current Applications," *IEEE Transactions on Plasma Science*, vol. 50, no. 10, pp. 3452–3458, Oct. 2022, ISSN: 0093-3813. DOI: 10.1109/TPS.2022.3192561.

[66] E. Shahriari, T. Maysonnave, A. I. Gusev, A. S. de Ferron, L. Pecastaing, and B. M. Novac, "Impact-Ionization Switching of High-Voltage Thyristors Connected in Parallel," *IEEE Transactions on Plasma Science*, vol. 51, no. 10, pp. 2878–2884, Oct. 2023, ISSN: 0093-3813. DOI: 10.1109/TPS.2023.3275315.

[67] E. Shahriari, T. Maysonnave, A. I. Gusev, A. S. de Ferron, and L. Pecastaing, "Series–Parallel Connection of Thyristors Triggered in Impact-Ionization Wave Mode," *IEEE Transactions on Plasma Science*, vol. PP, pp. 1–8, 2024, ISSN: 0093-3813. DOI: 10.1109/TPS.2024.3377898.

[68] G. Wang, J. Su, Z. Ding, X. Yuan, and Y. Pan, "A semiconductor opening switch based generator with pulse repetitive frequency of 4 MHz," *Review of Scientific Instruments*, vol. 84, no. 12, p. 125 102, Dec. 2013, ISSN: 0034-6748. DOI: 10.1063/1.4833683.

[69] R. A. Fitch and V. T. S. Howell, "Novel principle of transient high-voltage generation," *The Institution of Electrical Engineer*, vol. 111, pp. 849–855, Apr. 1964, ISSN: 2053-7891. DOI: 10.1049/piee.1964.0139.

[70] M. Rivaletto, "Conception de générateurs de fortes puissances pulsées : mise en forme et caractérisation de l'impulsion haute tension," Génie Électrique. Université de Pau et des Pays de l'Adour, Français., Ph.D. dissertation, 1997, 220 p.

[71] Z. Shotts, Z. Roberts, and M. F. Rose, "Design principles for vector inversion generators," pp. 556–559, 2008. DOI: 10.1109/ppps.2007.4651904.

[72] J. Yan, S. Parker, and S. Bland, "An Investigation into High-Voltage Spiral Generators Utilizing Thyristor Input Switches," *IEEE Transactions on Power Electronics*, vol. 36, no. 9, pp. 10 005–10 019, 2021, ISSN: 19410107. DOI: 10.1109/TPEL.2021.3063499.

[73] A. I. Gusev, I. Lavrinovich, S. Bland, *et al.*, "New SOS Diode Pumping Circuit Based on an All-Solid-State Spiral Generator for High-Voltage Nanosecond Applications," *IEEE Transactions on Plasma Science*, vol. 51, no. 10, pp. 2858–2865, 2023, ISSN: 19399375. DOI: 10.1109/TPS.2023.3273813.

[74] L. Li, C. Bao, X. Feng, Y. Liu, and L. Fochan, "Fast switching thyristor applied in nanosecond-pulse high-voltage generator with closed transformer core," *Review of Scientific Instruments*, vol. 84, no. 2, 2013, ISSN: 00346748. DOI: 10.1063/1.4792593.

[75] Colonel Wm. T. McLyman, *Design Handbook Transformer and Inductor Design Handbook Fourth Edition*. 2011, p. xi, ISBN: 9781439836880.

[76] J. Choi, "Introduction of the Magnetic Pulse Compressor (MPC) - Fundamental Review and Practical Application," *Journal of Electrical Engineering and Technology*, vol. 5, no. 3, pp. 484–492, Sep. 2010, ISSN: 1975-0102. DOI: 10.5370/JEET.2010.5.3.484.

Chapter 2

Study of OTS diodes as high-voltage opening switches

Chapter 2

Study of OTS diodes as high-voltage opening switches

This chapter is devoted to the study of power diodes operating as opening switches. The primary objective of the research is to investigate the ability of standard diodes to rapidly switch off a high reverse current and generate nanosecond high-voltage pulses. To achieve this, various OTS diodes are studied in two test benches with a primary storage energy of 25 mJ and 10 J, which are built according to the methodology outlined in Chapter 1 using an SPT. The current chapter contains information on diode types and selection criteria, which complements the methodology and results presented in the article on which this chapter is based:

M. R. Degnon, A. I. Gusev, A. Silvestre de Ferron, L. Pécastaing, G. Daulhac, A. Baranov, S. Boisne, and B. M. Novac, *"Off-the-Shelf Diodes as High-Voltage Opening Switches,"* in IEEE Transactions on Plasma Science, vol. 50, no. 10, pp. 3384-3392, Oct. 2022, DOI: 10.1109/TPS.2022.3177702.

2.1 Diode type and selection criteria

Rectifying diodes are designed to minimize reverse current and recovery time, essential for power rectification, thus avoiding conducting a high reverse current. Surprisingly, in the context of pulsed power opening switches studied in this work, the opposite effect is sought. In other words, the research endeavors to find OTS diodes capable of passing a high reverse current before interrupting it rapidly. Consequently, for the opening switch application which is contrary to their usual design, the OTS diode selection criteria are far from straightforward.

2.1.1 Diode selection criteria

The literature on SOS diodes outlined in Chapter 1 provides information about their deep $p-n$ junction, particular doping profile, and structure. However, this information is unavailable for OTS diodes and therefore cannot be selection criteria. In addition, the SOS effect suggests a switched current density over 1 kA/cm^2, yet the chip cross-section of encapsulated OTS diodes is not disclosed. Because of these limitations, we have established diode selection criteria based on specifications readily available in the data sheet, such as forward and surge current ratings, blocking voltage, and recovery time.

Diodes of average maximum forward current higher than 0.2 A and forward surge current from a few amperes to hundreds of amperes are included in this research. The current values provided in data sheets generally reflect power electronics requirements, and therefore durations of several microseconds at most. At sub-microsecond pulse durations, components can typically handle higher currents. In addition, the current value can give an indication of the die surface area inside the encapsulated diodes, as a larger cross-section of the die is generally associated with high currents.

As the die size is often not disclosed for packaged diodes, various types of packages including axial lead, through hole, surface mount, terminal bold mount, panel mount, stud mount, etc. are considered in this study. For all the diodes selected, the die dimensions are measured

after removing the protective package. These measurements allow us to estimate the current density switched by the diodes.

In terms of voltage criteria, we have set the minimum blocking voltage of the diode at 200 V. Such a low value is justified by the possibility of connecting several diodes in series, since in SOS mode, the voltage is automatically distributed across the series-connected diodes. In addition, to allow a high reverse current in the switch, diodes with a long recovery time reaching several microseconds are included in this work. It should be noted, that this duration was not available for all diodes.

2.1.2 Selected diode types

Avalanche and power diodes are the main categories of diodes examined in this study since these types of diodes have been used in the literature as opening switches [1], [2]. A short description of the diode types is given in the following.

Power diodes, also known as pin diodes, are generally classified as rectifiers and fast recovery diodes [3]. These silicon devices feature a $p^+ - n - n^+$ structure, characterized by a low resistance to forward current, due to the action of minority carriers, and a high resistance to reverse current when the space charge region extends [4], [5]. Hence, the reverse current is normally blocked at a negative voltage applied to the anode, resulting in a small reverse current (a few µA) flowing through the diode in this state. This current is negligible compared with the forward current. However, if the negative voltage is suddenly applied to the anode, right after the flow of a direct current, a brief period is required for the charge stored during the forward conduction state to be removed and the space charge region to recover [3]. During this period, the diode conducts the full reverse current until its recovery. According to [4], three main types of recovery characteristics can be distinguished (Figure 2.1): (a) conventional rectifier recovery, (b) snappy or abrupt fast recovery, and (c) soft fast recovery. The type of recovery depends on the doping profile of the diode and the reverse recovery technique applied [3] which are generally manufacturer-specific.

Whereas the characteristics shown in Figure 2.1 are observed after relatively long forward current durations (milliseconds and longer), the diode recovery characteristic in the pulsed regime is not generally clarified in the data sheet. In this study, we assume that the rectifier diodes may exhibit nanosecond high reverse current conduction, with a pulsed forward current of duration in hundreds of nanoseconds. Moreover, for a snappy fast recovery diode, the abrupt current cut-off [Figure 2.1 (b)] suggests that a fast current interruption can be observed in these diodes, making them potentially relevant to our work.

The avalanche diode is a type of diode engineered to operate in the reverse-biased mode. They have a well-controlled breakdown voltage, characterized by a sharp transition from high resistance to low resistance at avalanche breakdown [5]. As described in [6], the avalanche breakdown occurs when a reverse voltage exceeding the device specification is applied to its anode, causing a rapid increase in the reverse current.

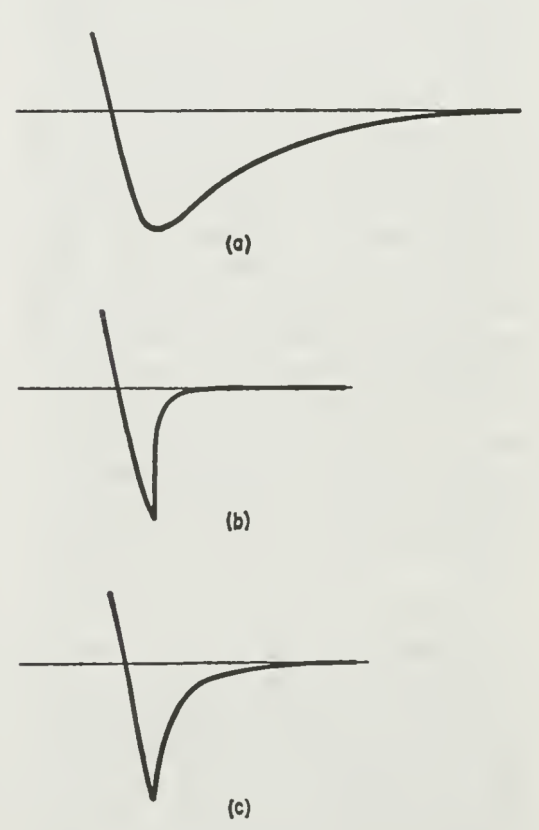

Figure 2.1: Characteristics (current versus time) of rectifier diodes reverse recovery: (a) conventional recovery, (b) snappy fast recovery, and (c) soft fast recovery [4].

The applied voltage induces a high electric field across the depletion region, which accelerates charge carriers until they acquire sufficient kinetic energy to generate further carriers through collision with atoms in the crystal lattice. These newly generated carriers contribute to an exponential increase in the current. Avalanche breakdown is also characteristic of Zener and Transient Voltage Suppression (TVS) diodes, which are designed to operate in this breakdown regime. According to [4], uniform breakdown across the entire junction area is crucial to avoid damaging the device. Therefore, a uniform doping distribution around the device junction and a specific shaping of the $p-n$ junction edges is required to attenuate intense localized electric fields at the junction surface [4].

Avalanche diodes are used in applications such as voltage regulation, surge protection, and in circuits requiring stable reference voltages. One of their applications in pulsed power is high-voltage pulse sharpening, as described in [7]. Besides, their ability to conduct high reverse currents without degradation led to our interest in their investigation as an opening switch.

The description of the experiment and discussion of the results are given in the following article, which is provided in its accepted version without the publisher's formatting. In accordance with our industrial partner's requirements, the diode references are not included in this document.

2.2 Off-the-shelf diodes as high-voltage opening switches

Abstract: An SOS diode is a solid-state nanosecond switch of gigawatt power level. Due to its high pulse repetition rate, long lifetime, and maintenance-free capability, the SOS diodes are becoming increasingly attractive for use in solid-state pulsed power generators. However, the lack of SOS diode manufacturers prevents the widespread use of this technology. This work demonstrates the ability of OTS diodes to operate in the SOS mode. A wide range of OTS diodes including rectifier, fast recovery, avalanche, and transient-voltage-suppression (TVS) diodes have been tested as high-voltage opening switches. An experimental arrangement based on an SPT was developed to test OTS diodes in the SOS mode. The results obtained were compared with the existent top-of-the-range SOS diodes, used as reference. Two versions of the experimental setup with the initially stored energy of 25 mJ and 10 J were used. The following pulse parameters were obtained using OTS diodes: 1) peak voltage impulse of 3 kV and rise time of 10 ns with a 110 Ω load (for the 25 mJ setup) and 2) peak voltage impulse of 80 kV and rise time of 20 ns with a 1 kΩ load (for the 10 J setup). Based on the parameters obtained, the door is opened for a future use of OTS diodes as opening switches in a wide range of solid-state-based pulsed power systems.

2.2.1 Introduction

The switch is one of the fundamental components of all pulsed power systems and can be either a closing or an opening type. The type of switch used depends on the way the energy is stored. Closing switches are used in CES systems, such as Marx generators and pulse forming lines. Opening switches are used in circuits based on IES, which have a higher energy density than CES [8]. According to [9], there are several fundamental differences between these two types of switches, which put the opening switch in a more attractive position for nanosecond pulsed power technology. An opening switch allows faster energy transfer, with the current cutting-off process increasing the output voltage, which results in a pulsed power gain.

However, while it is simpler to switch the energy stored in CES through conventional spark gap closing switches, the requirements on opening switches used in IES are usually challenging, particularly when it is required to switch off, rapidly and repetitively, several kiloamperes to generate hundreds of kilovolts or even a few megavolts pulses [10]. Solid-state devices are widely used in power electronics, such as IGBTs, GTO thyristors, and MOSFETs. All these are potentially usable as opening switches; however, they are currently limited either by a maximum current or by their switching characteristic speed [11]–[13]. With very few exceptions, the plasma opening switch or the exploding wire is unsuitable for high PRF operation and has a limited lifetime [8], [9].

Toward the end of the 20^{th} century, the SOS effect was discovered in $p^+ - p - n - n^+$ silicon diode structure by Rukin *et al.* [14]. The SOS effect is the nanosecond cut-off of high-density reverse currents in semiconductor diodes, for which a theoretical model was proposed in [15].

Based on this effect, SOS diodes were developed over three decades ago [16]. That sparked a breakthrough in the development of solid-state pulsed power systems based on IES, since it allows the improvement of their important characteristics such as current density, pulsed power, voltage, energy, and PRF [17], [18]. Due to high PRF of operation, long lifetime, and high average power, the SOS generators are currently used not only in research but also in modern biological, medical, and industrial applications, such as X-ray pulsed sources, particle accelerators, non-thermal plasma purification of water and gas, e-beam sterilization, laser pumping sources, and many other [7], [19]–[24].

However, the interest in the benefits of SOS for improving the performance of pulsed power systems sharply contrasts with a lack of SOS diode manufacturers. Hence, demonstrating the possibility of using OTS diodes as SOS diodes represents the main aim of the research presented in this article. A wide range of OTS diodes have been tested as high-voltage opening switches at switching energies of up to 10 J. The results are presented in Sections 2.2.2 and 2.2.3, devoted to the 25 mJ and 10 J experimental arrangements, respectively. Sections 2.2.4 is devoted to conclusions.

2.2.2 25 mJ experimental arrangement

2.2.2.1 Circuit description

A simplified circuit of the low-energy test bench is shown in Figure 2.2. The circuit is designed with a single magnetic element to ensure high energy efficiency, which can be up to 70% [25]. For convenience, a self-breakdown spark gap SG is used as a primary switch. The ceramic capacitors C1 and C2 have a capacitance of 50 nF and 12.5 nF, respectively. The magnetic core of the pulse transformer PT consists of a single nanocrystalline ring (100 mm × 80 mm × 20 mm) obtained from Vacuumschmelze, with the saturation induction being 1.2 T [26]. PT ensures two main functions. The first is to transfer the energy from the primary to the secondary circuit, stepping up the voltage. The second is to have a very low inductance of the secondary winding when the magnetic core is driven to saturation. The primary and secondary windings of the transformer have $w_1 = 1$ and $w_2 = 2$ turns, respectively.

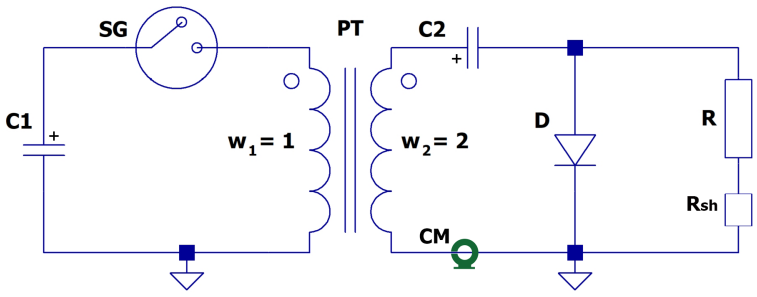

Figure 2.2: Circuit diagram of the 25 mJ experimental arrangement. Explanations are provided in the text.

A bias winding of two turns (not shown) with a maximum current amplitude of 3 A is used to reset the core before the next pulse. The low-inductance resistive load R is connected in parallel to the diode D under test.

The circuit of Figure 2.2 operates as follows. First, C1 is charged to its initial voltage V_{C1} by an external dc power supply (not shown). When SG closes, C1 releases its energy via PT into C2, while the current flows through the diode D in the forward direction. For an SOS diode, this is the forward pumping stage, which lasts for t^+ while the current reaches its maximum amplitude I^+ [Figure 2.3 (a)].

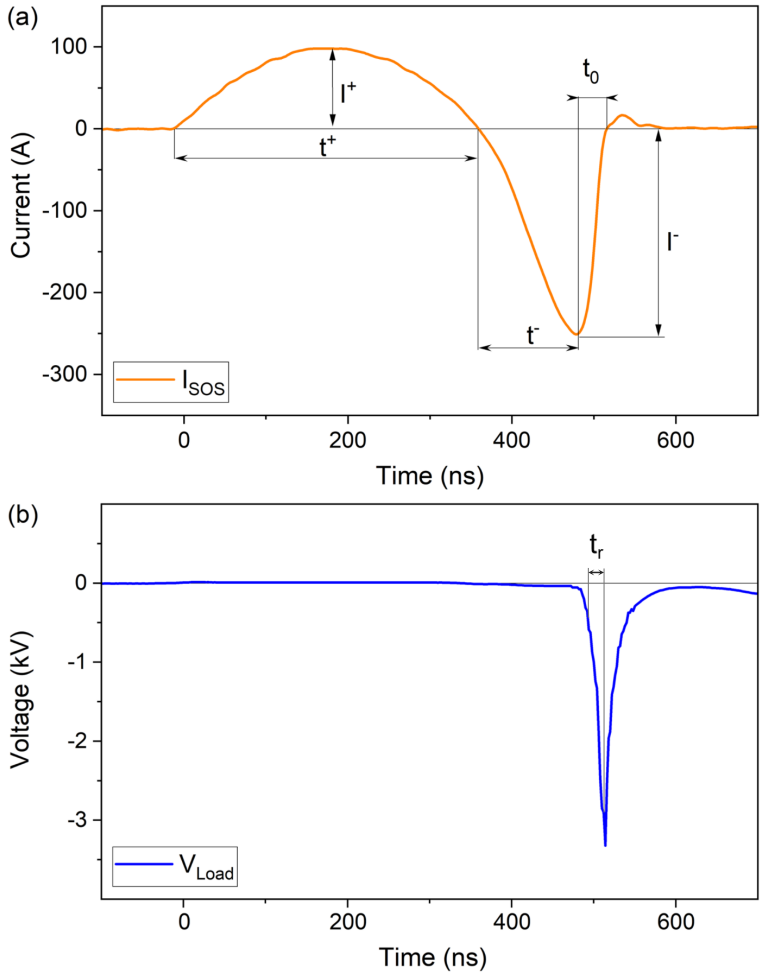

Figure 2.3: Typical waveforms of the current flowing through (a) SOS-R diode, and (b) voltage across the load R = 28 Ω, for V_{C1} = 1 kV.

The circuit is designed using the voltage-time product [27] to reach the maximum voltage across C2 at the moment when the magnetic core of the pulse transformer saturates. At this moment, C2 starts discharging through the secondary winding w_2 of the saturated transformer, generating the reverse current through the diode. This represents the reverse pumping stage for the SOS diode, where the current reaches the maximum amplitude I^- after a duration

t^- [Figure 2.3 (a)]. The magnitude of the reverse current, and thus the reverse current density, is greater than the forward current due to the much lower self-inductance of the saturated pulse transformer. Finally, this reverse current is cut off within the switching time t_0 [Figure 2.3 (a)] by the SOS diode and the energy is transferred to the load R, generating a very short nanosecond high-voltage pulse [Figure 2.3 (b)] with its characteristic rise time t_r.

A reverse current with a density of more than 1 kA/cm^2 leads to a high electric field region, which is formed in the $p-$region of the SOS diode structure ($p^+ - p - n - n^+$) due to the electron-hole plasma motion. Hence, in the SOS diode, the current interruption occurs in the $p-$region rather than in the $p-n$ junction. Details of the SOS diode physics are described in [9].

All rise times (t_r) in the present article are defined as the time interval from 10% to 90% of the peak impulse. The charging voltage of C1 is measured using the Tektronix probe P6015A. The voltage across the load and the current through the diodes are obtained using the current measurements of the Pearson current monitor (CM in Figure 2.2) model 410 and the resistive shunt $R_{sh} = 0.9\ \Omega$ (Figure 2.2). The waveforms are captured using a Rigol DS1204B real-time oscilloscope.

2.2.2.2 Low-voltage diodes

A total of 25 types of OTS diodes were selected and tested as opening switches including rectifying, avalanche, Schottky, TVS, and Zener diodes. The specifications of the studied diodes are as follows: blocking voltage ranging from 0.2 kV to 10 kV, die area from 0.01 cm^2 to 0.81 cm^2 and a recovery time from 0.1 µs to 20 µs. The die area of each diode was measured to calculate the cutting current density which, according to [14], must be more than 1 kA/cm^2 in the SOS mode of operation. SOS diodes manufactured in Russia and kindly provided by the Institute of Electrophysics having 0.25 cm^2 die area and 3 kV rated voltage, and here termed SOS-R, are used as a reference to which the characteristics of all the OTS units are compared to.

2.2.2.3 Results and discussion

First, the reference SOS-R diode is tested in the circuit shown in Figure 2.2 with the charging voltage V_{C1} fixed at 1 kV. The results obtained using SOS-R with a load resistance $R = 28\ \Omega$ are presented in Figure 2.3. A forward pumping current $I^+ = 100$ A flows through the single SOS diode within $t^+ = 380$ ns. After saturation of the transformer magnetic core, a reverse current $I^- = 260$ A flows through the diode for a duration $t^- = 120$ ns. After that, the current is cut off by the SOS-R diode within a time $t_0 = 34$ ns. A voltage pulse with an amplitude of 3.4 kV and a rise time of 20 ns is obtained at the load. The voltage amplitude V_{C2} measured at the capacitor C2 is 1.7 kV, which gives an SOS-R overvoltage coefficient of 2, which is defined as $k_{ov} = V_R/V_{C2}$.

Second, after testing the SOS-R, all the 25 selected OTS diodes were tested one by one, in the same configuration as the SOS-R diode. Figure 2.4 shows all the current and voltage waveforms obtained during these tests in comparison to the results obtained from the SOS-R diode.

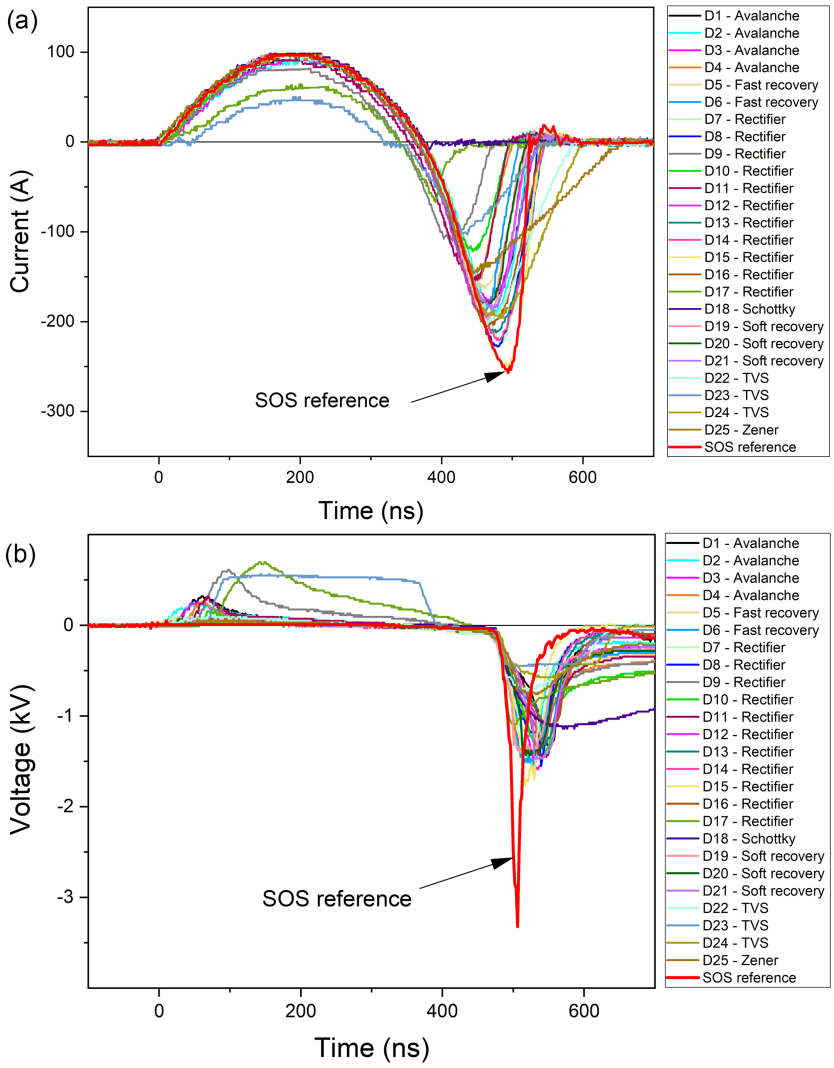

Figure 2.4: (a) Current and (b) voltage waveforms of the tested OTS diodes in comparison to the SOS reference diode.

As a general observation, it is clear that not all diodes can operate in the SOS mode. Rectifier, avalanche, Zener, and TVS diodes are able to open and transfer the current to the load. However, the switching time greatly varies. At the same time, the Schottky diodes, due to their structure and physics of operation, are not capable of reaching and interrupting the high reverse current. Small-area high-voltage diodes demonstrate a voltage drop during the forward current, which leads to additional energy losses and reduces the efficiency of the switch. Moreover, for most of the tested OTS diodes, the output voltage was limited to the level of the rated voltage for a switch consisting of a single diode.

To overcome the voltage limitation and to reduce the voltage drop during the forward current, a series-parallel connection of the diodes has also been studied. The parallel connection aims at reducing the voltage drop, while the series connection increases the blocking voltage capability. The even distribution of the voltage across the series connected SOS diodes [28] makes it possible to assemble the diodes without any voltage distribution circuit consideration. The best results obtained from the different types of single diodes are shown in Figure 2.5 (a) and (b); the improvement of the series-parallel connections can be seen in Figure 2.5 (c) and (d). The voltage capability of the OTS diodes is thus improved and, as a result, nanosecond voltages ranging from 1.8 kV to 2.5 kV were obtained on the resistive load of 28 Ω instead of 0.5 kV to 1.4 kV for single diodes. However, the highest corresponding overvoltage coefficient of the OTS diodes is 1.5, which is less than the coefficient obtained for the reference SOS-R diode which equals 2.

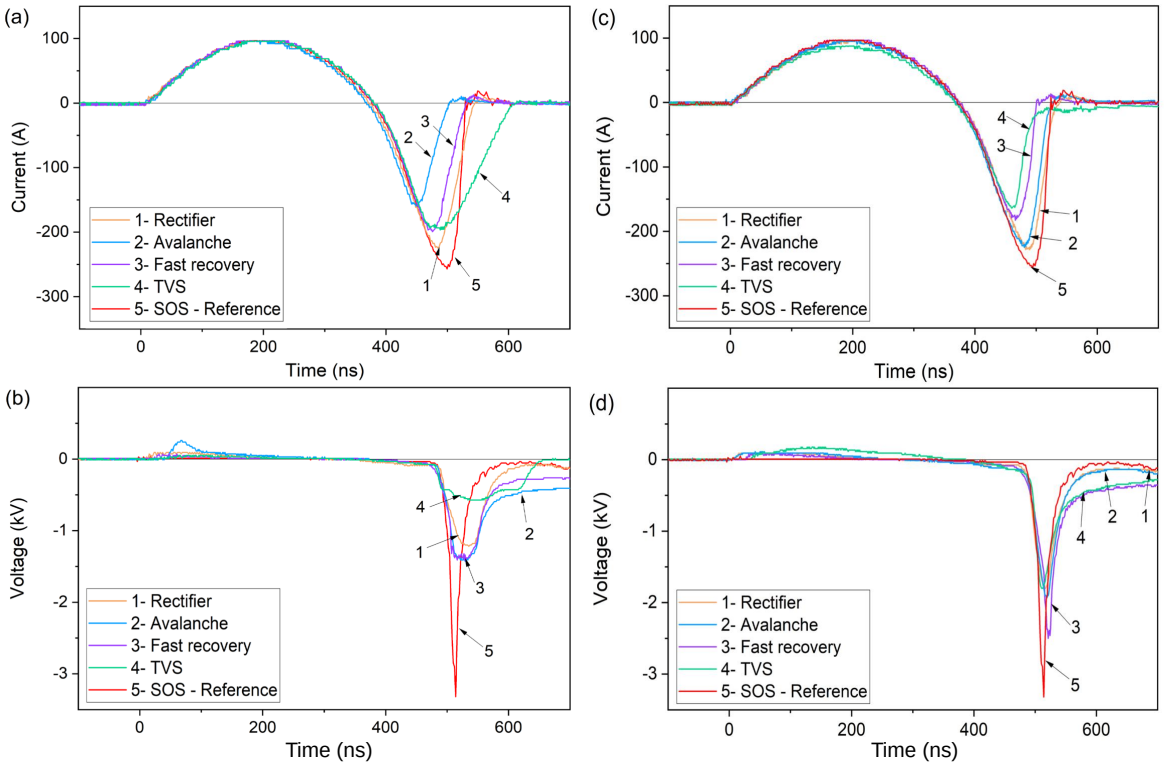

Figure 2.5: Current and voltage curves of the best pulse of each type of (a) and (b) single diode, and (c) and (d) diodes connected in series-parallel (1–Rectifier: 2 series x 2 parallels; 2–Avalanche: 2 series x 20 parallels; 3–Fast recovery: 2 series; 4–TVS: 7 series x 3 parallels), at the load of 28 Ω.

Even though the OTS diodes produce pulses with a voltage amplitude of about 25% less than the SOS diode, the obtained results confirm the possibility of using the OTS diodes as opening switches for IES circuits at the low energy level of 25 mJ. From a summary of the relevant parameters presented in Table 2.1, one can see that the TVS diodes, in particular, have the fastest switching time of 13 ns compared to the other types of tested

diodes. In addition, the FWHM of the OTS diodes' voltages are 1.6 to 3 times longer than the SOS-R.

Table 2.1: Voltage pulse parameters of the best tested OTS opening switches (V_{C1} = 1 kV and R = 28 Ω)

Diode type	Connections		V_R	t_r (ns)	FWHM
	Series	Parallel	(kV)	(10–90%)	(ns)
Rectifier	2	2	1.85	21.2	40
Avalanche	2	20	1.96	22.4	38
Fast recovery	2	1	2.54	27.1	28
TVS	7	3	1.83	13.2	45
SOS (Ref.)	1	1	3.35	19.5	16

Furthermore, a 3.15 kV output voltage with a rise time of 10 ns and an FWHM of 40 ns was obtained across a 110 Ω load using an assembly of 64 (8 series x 8 parallel) TVS diodes at a charging voltage across C1 of V_{C1} = 1.9 kV (Figure 2.6). In this configuration, the forward current of duration t^+ = 360 ns reached an amplitude I^+ of 170 A while the reverse current after flowing for t^- = 100 ns reached the amplitude I^- of 375 A with the diode having a current cut-off time of 30 ns.

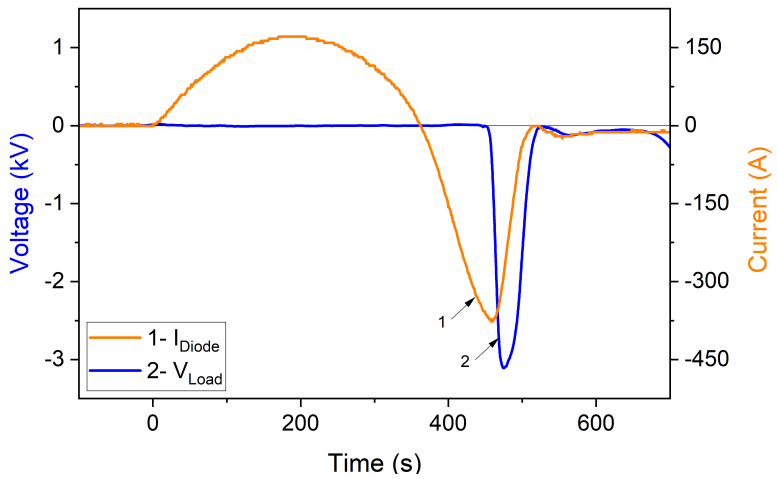

Figure 2.6: Waveforms of current flowing through the 64 (8 series x 8 parallel) TVS diodes assembly (1), and voltage pulse across the 110 Ω load (2), at V_{C1} = 1.9 kV.

2.2.3 High energy 10 J experimental arrangement

2.2.3.1 Circuit description

The equivalent electrical circuit of the high-energy test bench is presented in Figure 2.7. This circuit is similar to the one presented in Figure 2.2. A modification of the components was, however, implemented in order to increase the initially stored energy and, thereby, voltage amplitude across the load. Here, the transformer PT is based on a nanocrystalline magnetic core obtained from Finemet FT-3L, with the magnetic core parameters provided in [29]. The primary winding circuit consists of a film capacitor C1 = 200 nF, a triggered spark gap switch SG, and a single turn primary winding w_1. The secondary winding circuit consists of a ceramic capacitor C2 = 2 nF, a 10-turn secondary winding w_2, a diode D, and a resistive load R. To prevent any breakdown, the diode and the load are mounted under oil. Since the charging voltage of the primary capacitor is limited to 10 kV, the maximum initial electrostatic energy that can be stored is 10 J. The additional inductors L1 and L2 are further installed in order to vary the parameters of the forward and reverse pumping. The resetting circuit (not shown) consists of a five-turn bias winding driven by a dc source with an amplitude of up to 3 A. A choke (not shown) decouples the resetting circuit from the main circuit, preventing energy losses and protecting the current source. The operation of the circuit is similar to the one previously described in Section 2.2.2.

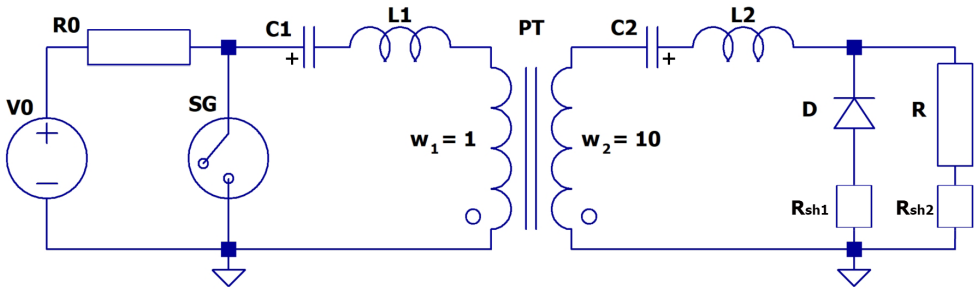

Figure 2.7: Circuit diagram of the 10 J experimental arrangement. Explanations are provided in the text.

The voltages V_{C1} and V_{C2} are measured using Tektronix P6015A and Northstar PVM100 probes, respectively. The waveforms are recorded by a DS1204B Rigol oscilloscope. The currents through the diode and the load are measured by two homemade resistive shunts (0.5 Ω and 0.15 Ω) with a usable rise time of about 0.5 ns. The voltage across the load is found using Ohm's law. A 7 GHz Tektronix TDS7704B oscilloscope is used to capture the extremely fast signals generated by the diode and the load circuits. Wide bandwidth attenuators by Barth (26 dB, 30 GHz) and RF-Lambda (6 dB and 20 dB, 4 GHz) are used to attenuate the high-voltage signals obtained from the resistive shunts.

2.2.3.2 High-voltage diodes

Several elementary OTS rectifier diodes were connected in series to build a high-voltage diode assembly having an overall blocking voltage of about 100 kV. This diode is termed OTS-100. The characteristics obtained for OTS-100 on the 10 J test bench are compared with those of the SOS-180-4 diode [25], rated for 180 kV which serves as a reference.

2.2.3.3 Results and discussion

First, the SOS-180-4 diode was tested on the 10 J test bench. The charging voltage of C1 (Figure 2.7) was fixed at 6 kV. A tubular non-inductive ceramic resistor R = 70 Ω was used as a load. For the SOS-180-4 diode, the following parameters were obtained [Figure 2.8 (a)]: forward pumping current I^+ = 400 A, duration t^+ = 440 ns, reverse pumping current I^- = 1.3 kA and reverse pumping time t^- = 90 ns while the cut-off time t_0 is 32 ns. The voltage pulse generated on the resistive load has an amplitude of 58 kV with a rise time of 19 ns, and a pulse duration of 55 ns (FWHM). The overvoltage coefficient k_{ov} of the SOS-180-4 diode is 1.2.

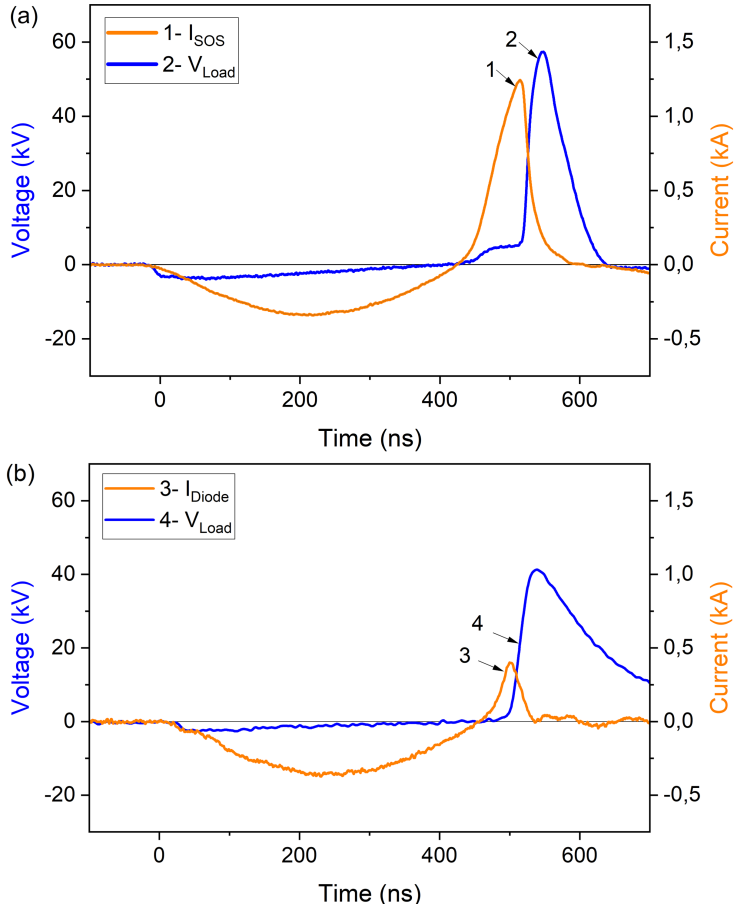

Figure 2.8: Waveforms of the current through the diode D (1, 3), and the voltage across the load R = 70 Ω (2, 4), at V_{C1} = 6 kV for (a) SOS-180-4 and (b) OTS-100.

Second, the current and voltage pulse parameters obtained using the OTS-100 operated under the same condition as the SOS-180-4 are as follows [Figure 2.8 (b)]: forward pumping current $I^+ = 370$ A, duration $t^+ = 440$ ns, reverse pumping current $I^- = 0.4$ kA and reverse pumping time $t^- = 45$ ns. The cut-off time t_0 was 23 ns. The load voltage pulse has an amplitude of 42 kV, a rise time of 22 ns, and a pulse duration of 108 ns (FWHM). The overvoltage coefficient of OTS-100 is $k_{ov} = 0.85$.

Both SOS-180-4 and OTS-100 have practically the same forward pumping parameters I^+, t^+ and voltage drop (Figure 2.8). However, the behavior of OTS-100 during reverse pumping is changing dramatically: its reverse pumping time t^- is two times less when compared to the SOS-180-4 diode. Eventually, this leads to the threefold decrease of the reverse current I^-, which prevents storing energy in IES (secondary winding inductance together with L2 and parasitic inductance). While the reverse-to-forward current ratio (I^-/I^+) of the SOS-180-4 is 3.2, this ratio is only 1.1 for the OTS-100. Hence, in the latter case, one part of the energy still remains stored in C2 at the current cut-off phase. Then both parts of the energy are switched into the load. As a consequence, the voltage pulse across the load has two clearly distinguished stages (Figure 2.9). The first high-voltage stage could be driven by the energy stored in the IES; the second low-voltage stage could be driven by the discharge of the remaining energy in C2. Since the time constant of the capacitor discharge is increasing, this effect is accentuated for high-impedance loads. For a 1 kΩ load, for example, the complete discharge of the capacitor into the load occurs after a few µs (Figure 2.9).

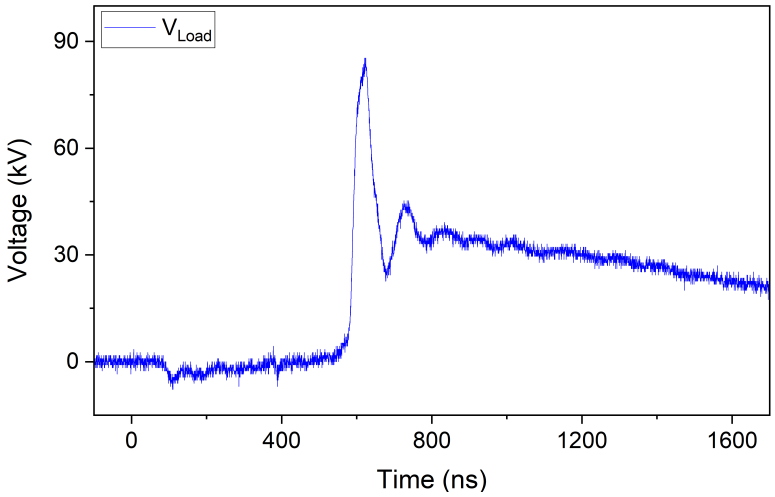

Figure 2.9: Waveform of the voltage across the load R = 1 kΩ at $V_{C1} = 6$ kV.

2.2.3.4 Optimization of the OTS-100 operating mode

This section is dedicated to an examination of the main factors affecting the reverse pumping parameters of OTS-100 when operating as an opening switch. An experimental study was undertaken to find ways to increase the reverse pumping time, the inductive stored energy, and, therefore, all the output pulse parameters.

First, the amplitude and duration of the forward and reverse pumping currents were varied, by changing V_{C1} (Figure 2.7) from 3 kV to 10 kV. During these tests, by changing V_{C1} and simultaneously adjusting the bias current, the voltage V_R across the 70 Ω load was adjusted almost linearly from 10 kV to 70 kV [Figure 2.10 (a)]. This demonstrates the possibility of building an adjustable pulse power generator based on an opening switch combined with an SPT.

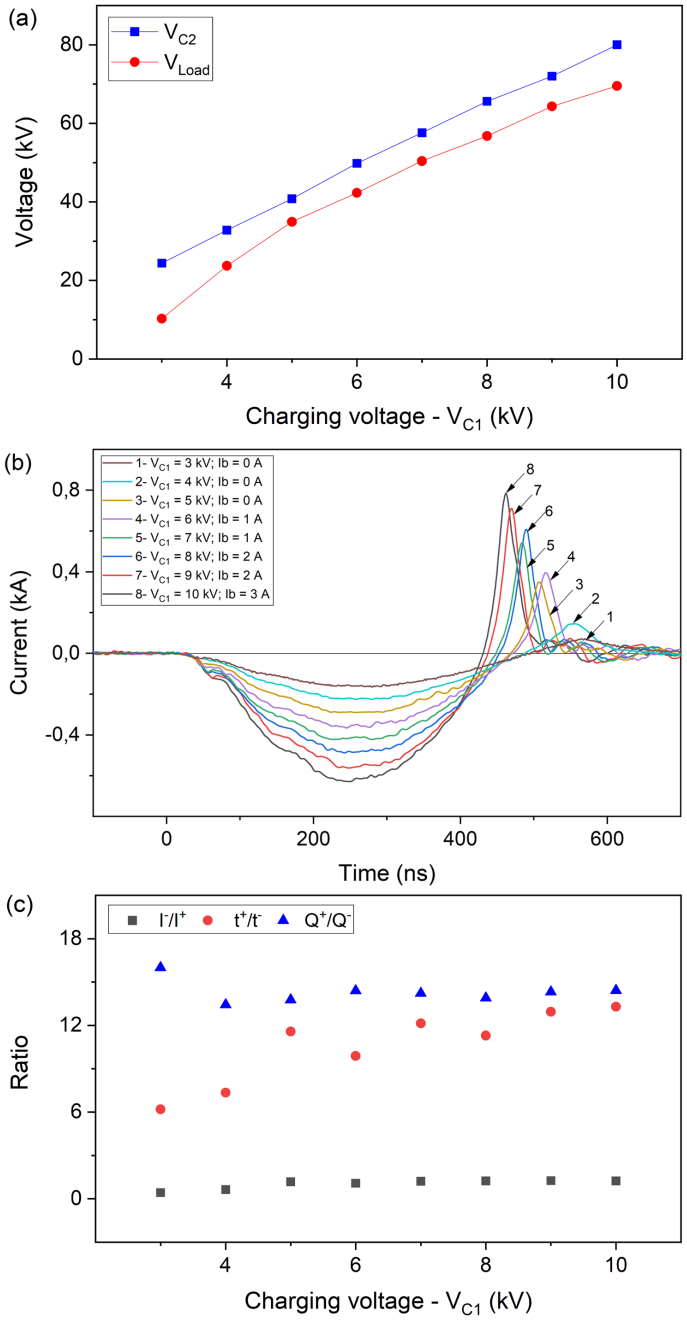

Figure 2.10: Evolution of (a) voltages across C2 (square) and load (round); (b) current through the diode; and (c) ratios of the pumping currents (square), pumping times (round), and electric charges (triangle), as a function of the charging voltage V_{C1} and time using the OTS-100 diode and the resistive load R = 70 Ω.

The maximum output voltage V_R = 70 kV with a rise time of 23 ns and duration of 100 ns (FWHM) was obtained for a 70 Ω load and for a charging voltage V_{C1} = 10 kV, which corresponds to 10 J energy stored in C1 [Figure 2.10 (a)]. The corresponding forward and reverse currents through the OTS-100 diode are I^+ = 0.6 kA and I^- = 0.8 kA, respectively. The load current reaches 1 kA, resulting in a load peak power of 70 MW.

The influence of V_{C1} on the diode pumping currents is presented in Figure 2.10 (b) and Figure 2.10 (c). When V_{C1} increases, both I^+ and I^- increase, respectively, from 160 A to 650 A, and from 70 A to 800 A. At the same time, t^+ slightly decreases from 480 ns to 400 ns while t^- decreases from 80 ns to 30 ns. Consequently, the ratio of the forward to reverse current duration t^+/t^- also increases. In addition, the ratio I^-/I^+ increases from 0.4 to 1.3 without approaching the SOS-180-4 diode current ratio of 3.2. It is worth mentioning a constant ratio of the forward and reverse electric charges Q^+/Q^- calculated as $Q = \int i(t)dt$ during diode forward and reverse pumping. For this experiment, the bias current [Ib in Figure 2.10 (b)] was fixed at zero for V_{C1} from 3 kV to 5 kV; at 1 A for V_{C1} from 6 kV to 7 kV; at 2 A for V_{C1} from 8 kV to 9 kV; and 3 A for V_{C1} = 10 kV.

To examine the impact of I^- magnitude on OTS-100 switching, an additional inductance L1 has been added in series with the capacitor C1, shown in Figure 2.7. Figure 2.11 summarizes the results. The inductance L1 was varied from 0 to 8.6 µH, causing the variation in I^- from 0.4 kA to 0.1 kA. During these experiments, I^+ and t^+ were changing as well, while t^- remained constant. For this experiment, a 50 Ω TVO less-inductive resistor load is used. The charging voltage V_{C1} was fixed at 6 kV. It was noted that increasing L1 causes the forward current duration to increase and the forward and reverse current amplitudes to decrease, while the reverse current duration remains about the same. This results in an increase in the ratio I^-/I^+ to 2.4. The t^+/t^- ratio obviously increases, as well as the forward to reverse electric charges.

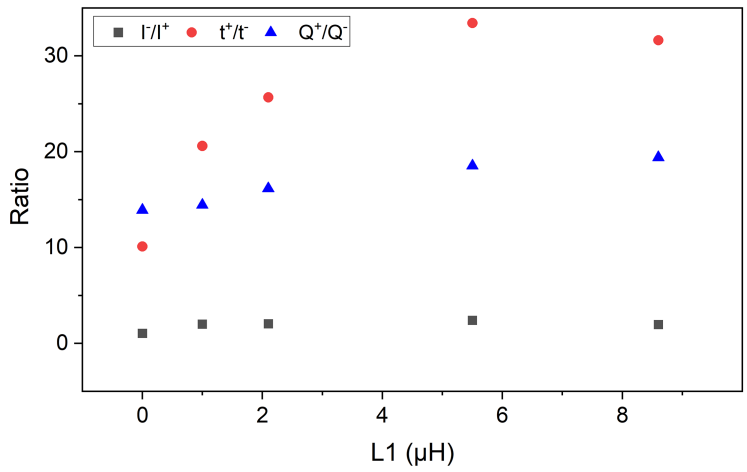

Figure 2.11: Ratios of the pumping currents (square), pumping times (round), and electric charges (triangle), as a function of the inductance L1 obtained for OTS-100 on the resistive load R = 50 Ω and charging voltage V_{C1} = 6 kV.

High values of inductance L1 lead to a decrease in the maximum voltage at C2 and, therefore, lower voltage across the load. Although the current ratio I^-/I^+ is improved by adding L1, the load current and voltage amplitudes drop, thus the use of a less inductive primary circuit is recommended.

According to the literature [10], a nanosecond current cut-off in semiconductor diodes with a switching power from megawatts to gigawatts can be realized using the DSRD or SOS. However, it seems that the results obtained in this work cannot be fully explained by these two mechanisms. While the limit of DSRD is 200–300 A/cm^2 [10], in the present work the OTS-100 diode operates at a current density of more than 1 kA/cm^2, which is usually considered as a threshold of the SOS mode [14]. Furthermore, even though OTS-100 was tested at the forward pumping mode required for the SOS mechanism, reverse pumping mode parameters were dramatically different from those expected from an SOS diode.

In particular, reverse pumping time t^-, which was limited by the reverse conductivity of the diode, was two times less compared to the SOS-180-4 diode. What is more important, t^- is almost insensitive to the forward pumping parameters such as t^+ and I^+. However, the cut-off time of the OTS-100 diode (tens of nanoseconds) is close to an SOS diode cut-off time at comparable voltage and power levels at the load. These facts probably require another mechanism of current interruption to be considered. At this moment, it is assumed that a specific diode structure – engineered for a fast recovery – could be a reason for the fast current cut-off. However, to shed light on this question, one needs to know the exact doping profile of the diode, which is usually a trade secret of the manufacturer.

Finally, the inductance L2 (Figure 2.7) was installed to investigate its impact on the shape of the output voltage and on the energy transferred to the load. An experiment was performed on 50 Ω and 1 kΩ loads with L1 = 0. The results are presented in Figure 2.12 (a) and Figure 2.12 (b); and Table 2.2 summarizes the parameters of the output voltage pulse and the energy efficiency as a function of the inductance L2. The energy delivered into the load is numerically estimated as the integral of the load power. The stored energy in the capacitor is calculated as the half product of the capacitance and the square of the voltage ($E_{C1} = \frac{C_1 V_{C1}^2}{2}$).

As shown in Figure 2.12 (a) for the low-impedance load, the inductance L2 reduces the amplitude of the load voltage pulse and increases pulse duration. The rise time is also extended and the input-to-output energy efficiency is not improved (Table 2.2). On the contrary, for high-impedance loads [Figure 2.12 (b)], L2 improves, in the first instance, the high-voltage part of the voltage pulse. The amplitude and duration of the high-voltage part are probably increased due to an increase in the energy stored in L2, which changes from 80 mJ to 260 mJ for L2 equal to 1 µH and 8.6 µH, respectively. In addition, the energy efficiency is slightly improved, though the rise time is increased (Table 2.2).

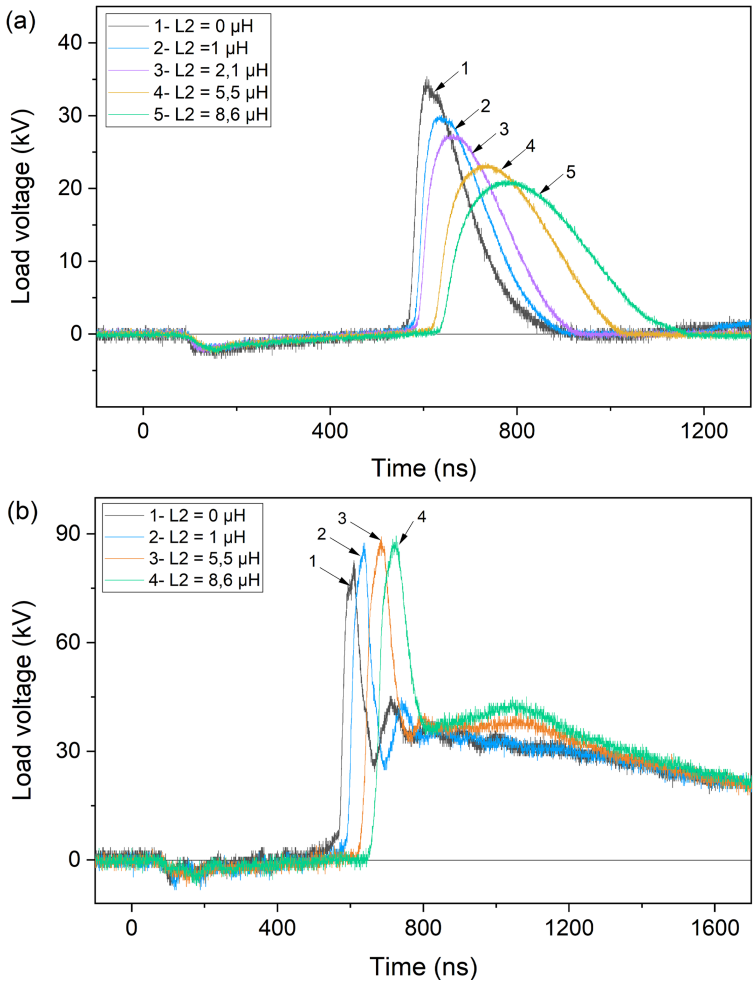

Figure 2.12: Load voltage at different L2 across (a) 50 Ω load, and (b) 1 kΩ load, using the OTS-100 diode at a charging voltage V_{C1} = 6 kV.

Table 2.2: Load voltage amplitude, rise time, FWHM, and energy efficiency at different L2 across 50 Ω and 1 kΩ ($\eta = \frac{E_R}{E_{C1}}$)

$\boldsymbol{R}$ (Ω)	$L2$ (µH)	V_R (kV)	t_r (ns)	$FWHM$ (ns)	η (%)
50	0	35	23	116	58
	0.3	32	26	130	55
	1.0	30	29	150	56
	5.5	24	53	250	55
	8.6	21	71	290	55
1000	0	83	21	63	44
	0.3	84	24	64	43
	1.0	86	28	65	42
	5.5	88	33	85	46
	8.6	87	34	105	48

2.2.4 Conclusion

The use of OTS diodes as SOSs has been investigated. Among the 25 OTS diodes tested with the low-energy test bench, the TVS diodes showed the best results in terms of switching time. The switching power of the OTS diodes was increased by series-parallel connections. Series connection of the OTS diodes increased the voltage capability of the switch, whereas parallel connection reduced its energy losses. It was shown that the output voltage can be linearly adjustable using a variable primary charging voltage combined with an appropriate resetting current. In order to optimize the energy efficiency of the circuit, the inductance of the primary circuit of the transformer should be minimized, while an appropriate secondary inductance should be determined depending on the load. The OTS diodes have shown good stability in voltage switching after a large number of shots, with no degradation of the diodes being observed during experimentation. When combined with a solid-state primary switch and the implementation of efficient cooling, the OTS diode assemblies represent a serious candidate to become a major asset in the development of high repetition rate nanosecond pulsed power systems.

2.3 Summary and outlook

In this chapter, the successful operation of OTS diodes as nanosecond high-voltage opening switches has been demonstrated. Promising results have been achieved with the following diode types: rectifier, fast recovery, avalanche, and TVS. Moreover, the study proves the possibility of combining multiple OTS diodes in series and parallel arrangement to increase the high-power capability of the switch. However, using such configurations with encapsulated diodes would significantly increase parasitic inductances and capacitances of the diode assembly, thus reducing output pulse performance.

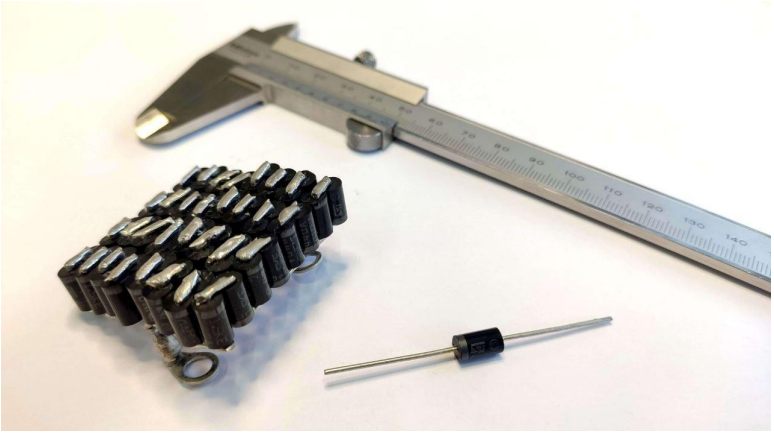

Figure 2.13: Assembly of sixty-four TVS diodes (8 series x 8 parallel).

Figure 2.13 shows an assembly of sixty-four 0.5 kV TVS diodes (eight in series and eight in parallel) that can withstand 4 kV at a switching current of about 1 kA. Using this as an example, it can be concluded that a series connection of at least a thousand diodes would be required to generate a 500 kV pulse. Such an arrangement would take up a considerable volume, not to mention the additional parallel connections necessary to limit the voltage drop and pre-pulse of the load voltage. For this reason, the development of the generator must be based on bare die diodes, as the OTS-100 introduced in Section 2.2.3.

Although the operation of OTS diodes has been verified on low- and medium-energy test benches (25 mJ and 10 J), their application on a higher-energy level ($>$ 10 J) for a system capable of generating up to 500 kV requires further validation. Thus, the design of a 40 J test bench has been undertaken to investigate OTS diodes at the high-energy level. This test bench, as previous ones, is based on the SPT described in Chapter 1. To optimize the transformer's energy efficiency, a study of nanocrystalline magnetic cores is carried out on the 10 J test bench. Chapter 3 provides an in-depth look at the investigation of the cores, exploring the importance of the main magnetic material properties such as hysteresis for the SPT.

2.4 References

[1] Y. A. Kotov, G. A. Mesyats, S. N. Rukin, A. L. Filatov, and S. K. Lyubutin, "Novel nanosecond semiconductor opening switch for megavolt repetitive pulsed power technology: Experiment and applications," *IEEE International Pulsed Power Conference - Digest of Technical Papers*, vol. 1, pp. 134–139, 1993, ISSN: 1996756X. DOI: 10.1117/12.204997.

[2] Y. Teramoto, H. Urakami, S. Katsuki, T. Namihira, and H. Akiyama, "Semiconductor opening switch based repetitive pulsed power generator," in *Conference Record of the Twenty-Fifth International Power Modulator Symposium, 2002 and 2002 High-Voltage Workshop.*, IEEE, 2002, pp. 210–213, ISBN: 0-7803-7540-8. DOI: 10.1109/MODSYM.2002.1189453.

[3] J. Lutz, H. Schlangenotto, U. Scheuermann, and R. De Doncker, *Semiconductor Power Devices*. Berlin, Heidelberg: Springer Berlin Heidelberg, 2011, ISBN: 978-3-642-11124-2. DOI: 10.1007/978-3-642-11125-9.

[4] RCA Corporation, *Solid-state Power Circuits: Designer's Handbook* (RCA designer's handbook: Echnical series). RCA. Solid State Division, 1971.

[5] S. M. Sze and K. K. Ng, *Physics of Semiconductor Devices*. Wiley, Oct. 2006, ISBN: 9780471143239. DOI: 10.1002/0470068329.

[6] B. J. Baliga, *Fundamentals of power semiconductor devices, Second edition*. 2018, pp. 1–1086, ISBN: 9783319939889. DOI: 10.1007/978-3-319-93988-9.

[7] A. S. Kesar, A. Raizman, G. Atar, *et al.*, "A fast avalanche Si diode with a 517 µm low-doped region," *Applied Physics Letters*, vol. 117, no. 1, 2020, ISSN: 00036951. DOI: 10.1063/5.0016228.

[8] H. Bluhm, *Pulsed Power Systems*. 2003, pp. 277–285, ISBN: 9783540261377. DOI: 10.1007/3-540-34662-7.

[9] S. N. Rukin, "Pulsed power technology based on semiconductor opening switches: A review," *Review of Scientific Instruments*, vol. 91, no. 1, p. 011 501, Jan. 2020, ISSN: 0034-6748. DOI: 10.1063/1.5128297.

[10] I. V. Grekhov and G. A. Mesyats, "Nanosecond semiconductor diodes for pulsed power switching," *Physics-Uspekhi*, vol. 48, no. 7, pp. 703–712, Jul. 2005, ISSN: 1063-7869. DOI: 10.1070/PU2005v048n07ABEH002471.

[11] S. Scharnholz, V. Brommer, G. Buderer, and E. Spahn, "High-power MOSFETs and fast-switching thyristors utilized as opening switches for inductive storage systems," *IEEE Transactions on Magnetics*, vol. 39, no. 1, pp. 437–441, Jan. 2003, ISSN: 0018-9464. DOI: 10.1109/TMAG.2002.806395.

[12] W. Jiang, K. Yatsui, K. Takayama, *et al.*, "Compact solid-state switched pulsed power and its applications," *Proceedings of the IEEE*, vol. 92, no. 7, pp. 1180–1195, 2004, ISSN: 00189219. DOI: 10.1109/JPROC.2004.829003.

[13] I. V. Grekhov and G. A. Mesyats, "Physical basis for high-power semiconductor nanosecond opening switches," *IEEE Transactions on Plasma Science*, vol. 28, no. 5, pp. 1540–1544, 2000, ISSN: 00933813. DOI: 10.1109/27.901229.

[14] G. A. Mesyats, S. N. Rukin, S. K. Lyubutin, *et al.*, "Semiconductor opening switch research at iep," *Proceedings of the 10th IEEE International Pulsed Power Conference, Albuquerque, New Mexico, USA*, pp. 298–305, 1995.

[15] S. A. Darznek, G. A. Mesyats, S. N. Rukin, and S. N. Tsiranov, "Theoretical model of the SOS effect," *1996 11th International Conference on High-Power Particle Beams*, pp. 1241–1244, 1996.

[16] S. N. Rukin, G. Mesyats, S. Darznek, *et al.*, "SOS-based pulsed power: development and applications," in *Digest of Technical Papers. 12th IEEE International Pulsed Power Conference. (Cat. No.99CH36358)*, vol. 1, IEEE, 1999, pp. 153–156, ISBN: 0-7803-5498-2. DOI: 10.1109/PPC.1999.825435.

[17] G. Wang, J. Su, Z. Ding, X. Yuan, and Y. Pan, "A semiconductor opening switch based generator with pulse repetitive frequency of 4 MHz," *Review of Scientific Instruments*, vol. 84, no. 12, p. 125 102, Dec. 2013, ISSN: 0034-6748. DOI: 10.1063/1.4833683.

[18] S. K. Lyubutin, M. Pedos, A. Ponomarev, *et al.*, "High efficiency nanosecond generator based on semiconductor opening switch," *IEEE Transactions on Dielectrics and Electrical Insulation*, vol. 18, no. 4, pp. 1221–1227, Aug. 2011, ISSN: 1070-9878. DOI: 10.1109/TDEI.2011.5976119.

[19] S. Y. Sokovnin and M. E. Balezin, "Improving the operating characteristics of an YPT-0.5 accelerator," *Instruments and Experimental Techniques*, vol. 48, no. 3, pp. 392–396, 2005, ISSN: 00204412. DOI: 10.1007/s10786-005-0068-0.

[20] S. Y. Sokovnin and M. E. Balezin, "Repetitive nanosecond electron accelerators type URT-1 for radiation technology," *Radiation Physics and Chemistry*, vol. 144, no. August 2017, pp. 265–270, Mar. 2018, ISSN: 0969806X. DOI: 10.1016/j.radphyschem.2017.08.023.

[21] T. Tang, F. Wang, A. Kuthi, and M. A. Gundersen, "Diode opening switch based nanosecond high voltage pulse generators for biological and medical applications," *IEEE Transactions on Dielectrics and Electrical Insulation*, vol. 14, no. 4, pp. 878–883, 2007, ISSN: 10709878. DOI: 10.1109/TDEI.2007.4286519.

[22] T. Sugai, W. Liu, A. Tokuchi, W. Jiang, and Y. Minamitani, "Influence of a Circuit Parameter for Plasma Water Treatment by an Inductive Energy Storage Circuit Using Semiconductor Opening Switch," *IEEE Transactions on Plasma Science*, vol. 41, no. 4, pp. 967–974, Apr. 2013, ISSN: 0093-3813. DOI: 10.1109/TPS.2013.2251359.

[23] T. Sugai, A. Tokuchi, and W. Jiang, "Experimental characteristics of semiconductor opening switch diode," *Proceedings of the 2014 IEEE International Power Modulator and High Voltage Conference, IPMHVC 2014*, pp. 105–107, 2015. DOI: 10.1109/IPMHVC.2014.7287218.

[24] K. Takaki, I. Yagi, S. Mukaigawa, T. Fujiwara, and T. Go, "Ozone synthesis using streamer discharge produced by nanoseconds pulse voltage under atmospheric pressure," *PPC2009 - 17th IEEE International Pulsed Power Conference*, no. December 2015, pp. 989–993, 2009. DOI: 10.1109/PPC.2009.5386169.

[25] A. I. Gusev, S. K. Lyubutin, A. V. Ponomarev, S. N. Rukin, and B. G. Slovikovsky, "Semiconductor opening switch generator with a primary thyristor switch triggered in impact-ionization wave mode," *Review of Scientific Instruments*, vol. 89, no. 11, p. 114 702, Nov. 2018, ISSN: 0034-6748. DOI: 10.1063/1.5052530.

[26] Vacuumschmelze, *Nanocrystalline material*. [Online]. Available: https://vacuumschmelze.com/products/soft-magnetic-materials-and-stamped-parts/nanocrystalline-material-vitroperm (visited on 05/14/2021).

[27] J. Choi, "Introduction of the Magnetic Pulse Compressor (MPC) - Fundamental Review and Practical Application," *Journal of Electrical Engineering and Technology*, vol. 5, no. 3, pp. 484–492, Sep. 2010, ISSN: 1975-0102. DOI: 10.5370/JEET.2010.5.3.484.

[28] A. V. Ponomarev, S. N. Rukin, and S. N. Tsyranov, "Investigation of the process of voltage distribution over elements of a high-power semiconductor current interrupter," *Technical Physics Letters*, vol. 27, no. 10, pp. 857–859, 2001, ISSN: 10637850. DOI: 10.1134/1.1414555.

[29] J. Holma and M. J. Barnes, "Prototype Inductive Adders With Extremely Flat-Top Output Pulses for the Compact Linear Collider at CERN," *IEEE Transactions on Plasma Science*, vol. 46, no. 10, pp. 3348–3358, Oct. 2018, ISSN: 0093-3813. DOI: 10.1109/TPS.2018.2836310. [Online]. Available: https://ieeexplore.ieee.org/document/8384315.

CHAPTER 3

Investigation of magnetic materials for a Saturable Pulse Transformer (SPT)

Chapter 3

Investigation of magnetic materials for a Saturable Pulse Transformer (SPT)

In this chapter, magnetic materials suitable for SPT in SOS generators are studied. As pointed out in Chapter 1, the circuit using a single magnetic element offers the highest energy efficiency in SOS systems. However, achieving high efficiency requires a magnetic core with minimal losses, particularly under fast pulse magnetization of about 500 ns needed to pump the opening switch. Since the performance of core materials depends on the magnetization time and the shape of the excitation pulse [1], [2], specific tests under operational conditions must be carried out to ensure the core's performance in the experiment setup.

To find a suitable magnetic material for SPT, several step-up transformers based on amorphous nanocrystalline magnetic cores are designed and tested at energies of up to 10 J. The investigation focuses on examining the energy efficiency and voltage/current output characteristics of the transformers under test. It is important to recall that the transformer in the SOS generator circuit is designed to saturate, thus providing a low inductance during the diode reverse pumping stage. Consequently, it also functions as a magnetic switch. Therefore, the switching performance of the transformers is also examined.

3.1 Introduction to magnetic material

The flow of an electric current through a conductor generates a magnetic field around it, as discovered by Orsted in 1820. When a magnetic material is placed near this conductor, it confines, channels, and guides the magnetic field, producing a magnetic flux whose direction depends on the polarity of the initial current. According to Faraday's law, any change in the magnetic field induces an electromotive force in the surrounding conductors. This forms the foundation of transformers.

Magnetic flux intensity depends on the core dimensions and material properties. According to [3], when a material is intended to operate as a magnetic switch, four main parameters have to be considered. First, the relative permeability μ_r of the material should be large in the unsaturated state and conversely minimal in the saturated state, thus ensuring a significant reduction of the inductance at saturation. Second, the core should feature a narrow hysteresis loop, i.e. low coercivity H_c, to minimize hysteresis losses as the enclosed area of the loop represents the energy lost in the core material during a cycle [4]. Next, to mitigate the eddy current losses, the core must have a high electrical resistivity ρ, which means the core should be wound using a thin tape. Last but not least, a high saturation induction B_{sat} is necessary to increase the magnetic swing ΔB (Figure 1.23 in Chapter 1), thereby reducing the cross-section of the core required for energy transfer.

The comparison of the magnetic materials illustrated in Figure 3.1 and summarized in Table 3.1 puts nanocrystalline materials in first place in terms of the desired material properties described above. Nanocrystalline cores are soft materials composed of small "nano-order" crystal grains obtained through the annealing processing of an amorphous alloy ribbon [5]. They feature high saturation induction, high permeability, relatively high resistivity, and good temperature resistance. Given their superior qualities compared with other materials,

the study focuses on the nanocrystalline material, investigating its properties and suitability for transformers used in SOS generators, where short energy transfer time and high rate of magnetization are required.

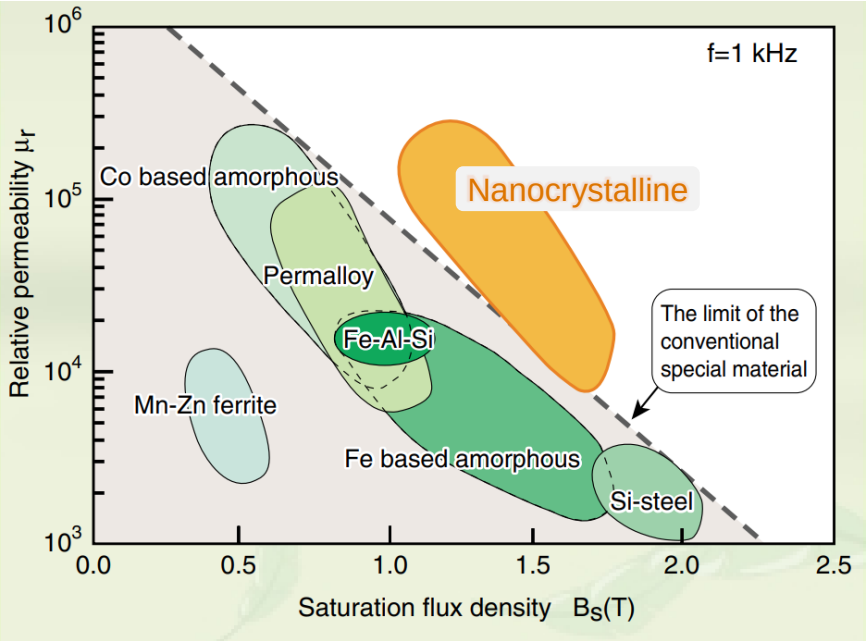

Figure 3.1: Comparison of different magnetic material properties [5].

Table 3.1: Parameters of different magnetic materials [3]

Category	B_s (T)	H_C (A/m)	μ_u	ρ ($\mu\Omega \times$ cm)	T (°C)
Silicon steel	1.8–2.2	<30	800–1500	45–80	690–730
Ferrite	0.4–0.6	<20	600–2500	10^5–10^9	150–250
Permalloy	0.6–1	<0.8	50 000–100 000	120–140	400–600
Co-based amorphous alloy	0.55–0.8	<0.8	30 000–100 000	40–60	350–500
Nanocrystalline	1.2–1.6	<1.6	50 000–100 000	80–130	550–600

The results of this study are detailed in the article:

M. R. Degnon, A. I. Gusev, A. Silvestre de Ferron, L. Pécastaing, A. Baranov, C. Mielot, S. Boisne, M. J. Barnes, V. Senaj, T. Kramer, and B. M. Novac, *"A Saturable Pulse Transformer Based on Nanocrystalline Magnetic Cores for an Adjustable Nanosecond High-Voltage Generator,"* in IEEE Transactions on Plasma Science, vol. 51, no. 10, pp. 2849-2857, Oct. 2023, DOI: 10.1109/TPS.2023.3284657.

3.2 A SPT based on nanocrystalline magnetic cores for an adjustable nanosecond high-voltage generator

Abstract: This article is devoted to SPTs, combining the functions of a pulse transformer and a magnetic switch. Two nanocrystalline magnetic cores are investigated in the SPT of an IES pulsed power system based on an SOS diode. The first magnetic core has a square hysteresis loop ($B_r/B_{sat} > 90\%$), while the second core has a flat hysteresis loop ($B_r/B_{sat} \sim 4\%$). A test bench with an initially stored energy of 10 J is developed. The circuit design is discussed, and the magnetic materials are compared. Based on the features of the hysteresis loops, two nanosecond high-voltage SOS generators are tested, with the output voltage adjusted by tuning the input voltage and controlling the bias magnetic field. The influence of the optimal core saturation on the operation of the SOS diode is studied. An adjustable output voltage impulse of more than 200 kV amplitude with a 16 ns rise time is demonstrated on a 1 kΩ resistive load.

3.2.1 Introduction

The advent of SOSs discovered in the 1990s [6] has opened the gate for solid-state pulsed power based on the IES technique. Recently, high-voltage nanosecond generators based on SOS diodes, so-called SOS generators, are becoming increasingly attractive for repetitive pulsed power applications. These systems have many advantages, such as high PRF, high reliability, and long lifetime, and are mainly used both in basic research and in major industrial applications such as high-power microwaves, pulsed HV gas, vacuum and underwater plasma electrical discharges, particle acceleration, X-ray devices, and many others [7]–[11].

From a structural viewpoint, the SOS generators usually involve magnetic elements, used in voltage-boosting pulse transformers and MPCs [7], [12]–[15]. The robustness, stability, high-frequency operation, and long lifetime of magnetic elements [3], [16]–[25], make these items suitable for use in solid-state generators. A noteworthy illustration is their utilization in the injection and extraction systems employed in state-of-the-art particle accelerator facilities [25], [26]. In addition, the use of multiple MPC stages enables reducing the stress on the primary solid-state switch while keeping a high voltage output, although the efficiency might be compromised [3], [17], [18], [21]. It is well known that the material of the magnetic element strongly affects the efficiency of the generator, especially at the fast magnetization that is particularly required for SOS generators.

Furthermore, adjustment of the output voltage level is often required in pulsed power applications including X-ray, e-beam, excimer lasers, generation of ozone, and others [17], [27]. In [22] and [27], the output voltage was adjusted by varying the input voltage, while using either an Fe-based amorphous or a permalloy magnetic core pulse transformer, respectively. However, the absence of a pre-magnetizing circuit introduces limits on the voltage regulation range and energy efficiency.

The work [23] proposed a method to regulate the peak voltage, the saturation time, and the pulse compression ratio, using different connection points of the magnetic switch winding to adjust the number of turns. However, this approach appears to be complex when a large number of connection points is required. A novel topology was suggested by [13] in which an additional primary circuit connected to the primary winding is used to reset the core. In this configuration though, the input voltage remains unchanged, which may lower the efficiency.

This work studies an SPT with a controlled time to saturation, as part of a high-efficiency adjustable SOS generator. A circuit containing a single magnetic element, an SPT, is used to ensure high efficiency.

In a single magnetic element SOS generator, an SPT combines two functions: 1) a step-up transformer with an energy transfer time of about 500 ns and 2) a magnetic switch with a current compression ratio of about 2.5. Nanocrystalline soft magnetic materials, presenting a high saturation induction, low magnetic losses, high permeability, and high resistivity, meet all the requirements for a highly efficient SPT [3], [28], [29]. Nanocrystalline MPCs were used in our recently published study [30] (Chapter 1), where OTS diodes were examined as high-voltage solid-state opening switches. The current article is centered on the SPT-based system in general, while also using an SOS diode. It is therefore focused on two types of nanocrystalline magnetic cores with different shapes of the hysteresis loop (i.e., B–H curve). The first type has a flat loop (i.e., a low remanent induction), which is traditionally used in transformers. The second type has a square hysteresis loop (i.e., a high remanent induction), which is a well-known characteristic of magnetic materials used in pulsed power magnetic switches. These magnetic materials are investigated when used in a single-core transformer topology, to compare their efficiency and suitability for the SPT of the SOS generator. To this end, a test bench with an initially stored energy of 10 J, is developed.

The article is structured as follows. In Section 3.2.2, the design of the pulse transformer, the operating principle of the SOS generator, and the characteristics of the nanocrystalline magnetic cores are described. In Section 3.2.3, the results obtained using the two different magnetic materials are compared and discussed. In the same section, two high-voltage SOS generators are presented. The article ends with the Conclusion and the suggested way ahead.

3.2.2 Circuit principle and system design

3.2.2.1 General layout and operating principle of the circuit

The general layout of the test bench is presented in Figure 3.2. The arrangement consists of a triggered spark gap switch SG and a film capacitor C1, connected to the primary winding of the SPT. The secondary winding of the transformer is connected to the low inductive ceramic capacitor C2, followed by the SOS diode and the resistive load R in parallel. The current viewing resistors R_{Sh1} and R_{Sh2} made in-house from carbon composition resistors, are used for the SOS current and load voltage measurements. The measurement of V_{C1} and V_{C2} is performed using North Star high-voltage probes type PVM-12 and PVM-100, respectively. A

pre-magnetizing circuit (magnetic bias circuit) is used to reset the core before each pulse. This circuit comprises a direct current (dc) source (IPS 303A, 0–3 A, 0–30 V) and an in-house made choke, which protects this current source from the main high-voltage pulse. The specifications of the circuit components are described in Table 3.2.

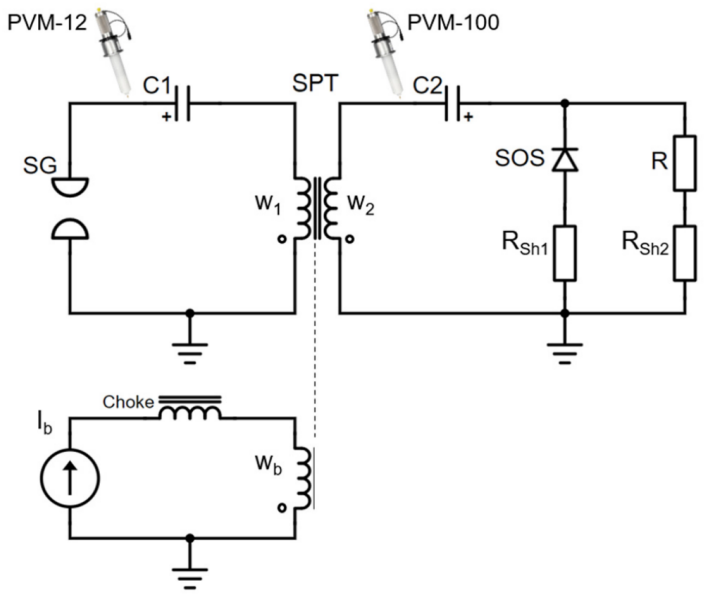

Figure 3.2: Circuit diagram of the experimental arrangement.

Table 3.2: Specifications of circuit components for the study of magnetic cores

	C1	C2	SOS	R	R_{Sh1}	R_{Sh2}
Value	200 nF	2 nF	180 kV / 4 kA	0.05 − 1 kΩ	0.15 Ω	0.5 Ω
Type	SPT-02QI	UHV-9A	SOS-180-4	TVO-20	RCC050	

The operating principle of the experimental setup (Figure 3.2) is as follows. C1 is charged by an external power supply (for simplicity, this is not shown). When SG closes, the energy stored in C1 is transferred to the capacitor C2 through the transformer SPT. The current of amplitude I^+ and duration t^+, termed "forward pumping current", flows through the SOS diode in a forward direction, charging C2. Subsequently, when the voltage across C2 reaches its maximum value, the SPT is designed to saturate. As a result, the secondary winding is decoupled from the primary winding. In addition, the inductance of the secondary winding of the saturated core significantly decreases due to the low permeability of the core in its saturated state. Hence, the discharge current of C2 of higher amplitude I^-, termed "reverse pumping current," flows through the SOS for the duration t^-. In order to reach the reversed current density of several to tens of kA/cm^2 that is required for the SOS-mode current cut-off [7], a high value of I^- is necessary to be generated. Finally, the high-value reverse current is interrupted by the SOS within the current cut-off time t_0, then the energy is transferred to

the load R, generating a nanosecond rise time high-voltage pulse.

The typical waveforms of the SOS current, the charging voltages V_{C1}, V_{C2}, and the load voltage V_R are presented in Figure 3.3. A non-zero resistance of the SOS in the conductive state causes negative and positive pre-pulses on the load voltage (V_R). This can be suppressed by two oppositely connected diodes in series with the load as described in [31]. However, this topic is beyond the scope of this work.

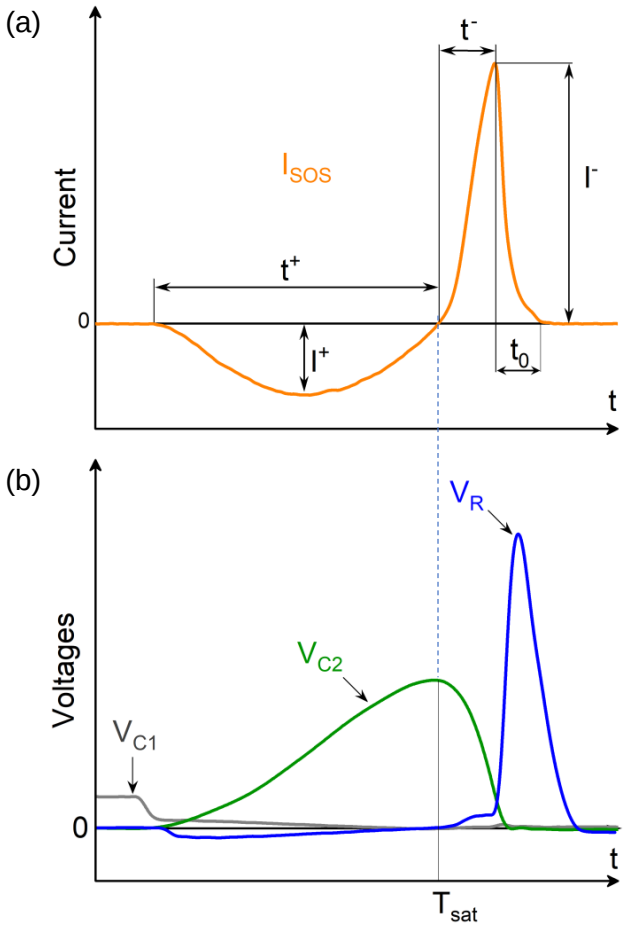

Figure 3.3: Typical waveforms of (a) current flowing through the SOS diode, and (b) voltages V_{C1}, V_{C2} (reversed for clarity), and V_R.

3.2.2.2 Design of the 100 kV SPT

The 10 kV capacitor C1 sets the input energy to 10 J maximum. A toroidal shape of the core is adopted, and the transformation ratio n is fixed to 10. To improve energy transfer efficiency, the primary and secondary capacitors are matched as follows:

$$C1 = n^2 \times C2 \tag{3.1}$$

According to the requirement for an SOS diode pumping as stated in [7] and based on preliminary studies, the forward and reverse pumping durations of the diode were defined respectively as $t^+ = 500\ ns$ and $t^- = 100\ ns$. Therefore, the equivalent capacitance C_{eq} and self-inductance L_{eq} of the transformer, when referring to the primary side, can be estimated as:

$$C_{eq} = \frac{C1 \times n^2 C2}{C1 + n^2 C2} = \frac{C1}{2} \tag{3.2}$$

$$L_{eq} = \frac{(t^+)^2}{\pi^2 \times C_{eq}} \tag{3.3}$$

where t^+ is the forward pumping time of the SOS. For an ideal energy transfer, t^+ must correspond to the time required for the peak voltage of C2 to be reached and to the saturation time T_{sat} of the transformer (Figure 3.3). In this condition, the size of the core is determined using the simplified form of the Faraday law termed the volt-second product:

$$2\Delta B \times S_c \times w_2 = V_{max} \times T_{sat} \tag{3.4}$$

where ΔB is the magnetic induction swing, S_c is the effective cross-section area of the material without the interlaminar insulating layers, w_2 is the number of turns of the secondary winding, and V_{max} is the peak voltage of C2. S_c is determined by multiplying the geometrical cross-section of the core S_g [Figure 3.4, Sg] by the packing factor k = 0.73, as indicated by the manufacturer. The packing factor represents the ratio of the effective to the geometrical cross-section area of the core, and due to the interlaminar insulation of the wound cores, it is always less than 1.

The magnetic induction swing ΔB, representing the change in the magnetic induction, is one of the most crucial parameters to consider when choosing the core material. Indeed, for the same core size, a material with a higher induction swing will lead to a higher energy transfer. In other words, a high saturation flux density implies a low magnetic core volume for the same voltage amplitude across the secondary winding.

As the transformer is operating in the air, proper attention should be paid to the electrical insulation. Hence, to prevent an electrical breakdown between the winding and the core, plastic insulating supports are designed [Figure 3.4, (2)]. The plastic supports were 3-D printed using polylactic acid (PLA) filaments. These supports, designed by considering the air dielectric strength as 30 kV/cm, ensure a minimum distance between the winding and the core of 12 mm in all directions. To extend the current path and prevent any surface breakdown, ripples are applied at the two ends of the support sleeves [Figure 3.4, (3)]. The transformer windings comprise a single-turn primary ($w_1 = 1$) and a 10-turn secondary ($w_2 = 10$) windings. The primary winding is made up of a metallic cylinder with a diameter of 100 mm, which is placed in the center of the transformer. The top part of the cylinder is connected to the primary capacitor C1 through a metallic plate. The base of the cylinder is directly connected to the grounded plate underneath the transformer. The secondary winding consists of two

parallel sections covering the entire surface of the core. To regulate the induction swing, an additional 5-turn winding is applied, as a part of the pre-magnetizing circuit.

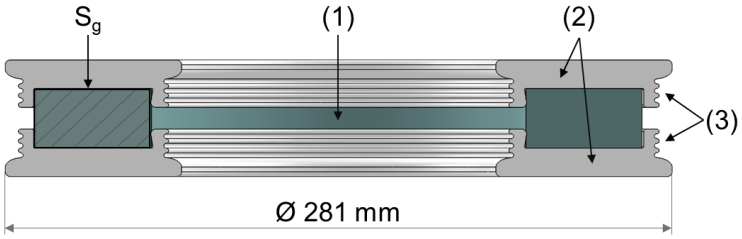

Figure 3.4: Sectional view of the SPT showing the cross-section Sg, the core (1), the PLA supports (2), and the rippled sleeves (3).

The link between the pre-magnetizing current and the induction is expressed, respectively by the following equations:

$$H = \frac{I_b \times w_b}{l_m} \tag{3.5}$$

$$B = \mu H \tag{3.6}$$

where H is the bias magnetic field, I_b is the pre-magnetizing current, w_b is the number of turns of the pre-magnetizing winding, l_m is the mean magnetic path length of the core, B is the induction flux, and μ is the magnetic permeability.

3.2.2.3 Overview of the tested cores

Two nanocrystalline Fe-based soft magnetic materials were investigated as SPTs. The nanocrystalline cores provide high saturation flux density, high relative permeability, low core loss, and excellent temperature characteristics for a wide frequency range [5]. The characteristics of the cores, including the saturation induction B_{sat}, the remanent induction B_r, the coercive force H_c, the magnetic material cross-section S_c, and the core size are all provided in Table 3.3, and their corresponding B–H loops are presented in Figure 3.5.

Table 3.3: Parameters of the pulse transformer cores

	B_{sat} (T)	B_r/B_{sat}	H_c (A/m)	S_c (cm^2)	$Size$ $(mm^3)^*$
Finemet FT-3H	1.23	>90%	0.6	8.29	256 x 165 x 25
Finemet FT-3L	1.23	4%	0.6	8.29	256 x 165 x 25

* Outer diameter (OD) x inner diameter (ID) x height (h) (see Figure 1.25 in Chapter 1).

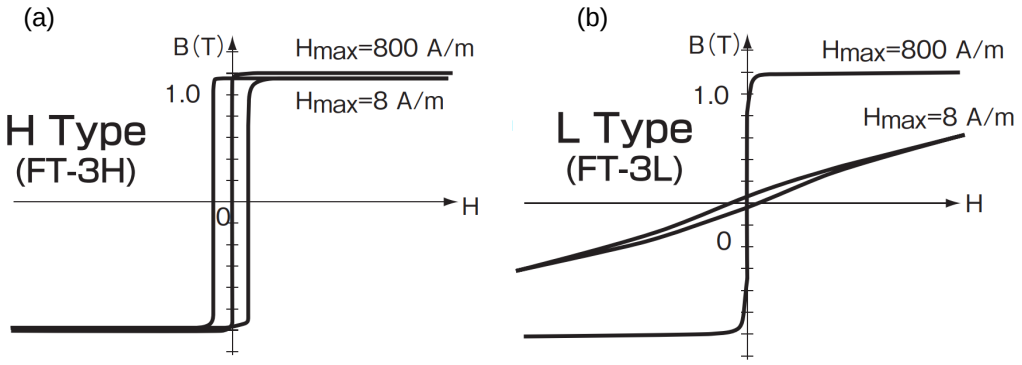

Figure 3.5: B–H loops of (a) Finemet FT-3H and (b) Finemet FT-3L [5].

3.2.3 Test and results

3.2.3.1 Investigation of the nanocrystalline magnetic cores

As described in Section 3.2.2.2, the parameters of the magnetic core, and particularly the effective induction swing, are critical to minimize the size of the core. However, the static characteristics provided in the manufacturer's datasheet may differ from dynamic characteristics, especially under fast pulse magnetization [3], [32]. Hence, in these experiments, the effective induction swings of the two cores are determined and compared. To this end, at a fixed input voltage, the bias magnetic field H_0 is continuously applied using the pre-magnetizing circuit, to set the initial induction to B_0. Thus, the total induction swing ΔB can be defined by:

$$\Delta B = B_{sat} - B_0 \leq 2B_{sat} \tag{3.7}$$

where the induction swing is obtained using the volt-second product defined in Equation 3.4. The peak voltage V_{max} of C2 is measured, and the saturation time T_{sat} is graphically determined using the SOS current and the V_{C2} waveforms (Figure 3.3). In these experiments, the input voltage is fixed at 6 kV and the magnetic field H_0 is varied from 0 to 23 A/m, to regulate the induction swing. H_0 is applied in the opposite direction compared to the main pulse, to increase the effective induction swing. The results obtained are plotted in Figure 3.6. The error bar corresponds to the inaccuracy in the measurement of the saturation time T_{sat}.

The induction swings obtained when operating the materials under fast pulse magnetization are in good agreement with the datasheet specifications. For the square B–H loop core (i.e., Finemet FT-3H), a maximum induction swing of 2 ± 0.2 T is achieved by applying a low magnetic field of absolute value H_0 about 5 A/m. The further increase in the bias magnetic field does not lead to the increase of the ΔB, which confirms the operation at the maximum induction swing. Hence, the maximum flux density, inducing the highest voltage across the secondary of the transformer (V_{C2}), can be achieved by applying a relatively low bias magnetic field using the square B–H loop core. However, the steep slope of the induction in the area between 0 and 2 A/m [Figure 3.6, (1)] seriously reduces the possibility of tuning the ΔB.

On the contrary, at the maximum bias magnetic field of 23 A/m, the maximum induction swing obtained while using the flat B–H loop core (i.e., Finemet FT-3L) is 1.75 ± 0.2 T. Even though the remanent induction of the Finemet FT-3L is low (∼0.05 T), the continuously applied H_0 makes it possible to achieve a substantial induction swing, close to $2B_{sat}$. Due to the limit of the pre-magnetizing circuit – limited current source and number of turns – the induction swing could not be further increased for this arrangement. However, the smooth slope of the induction curve [Figure 3.6, (2)] provides the excellent advantage of regulating the induction swing.

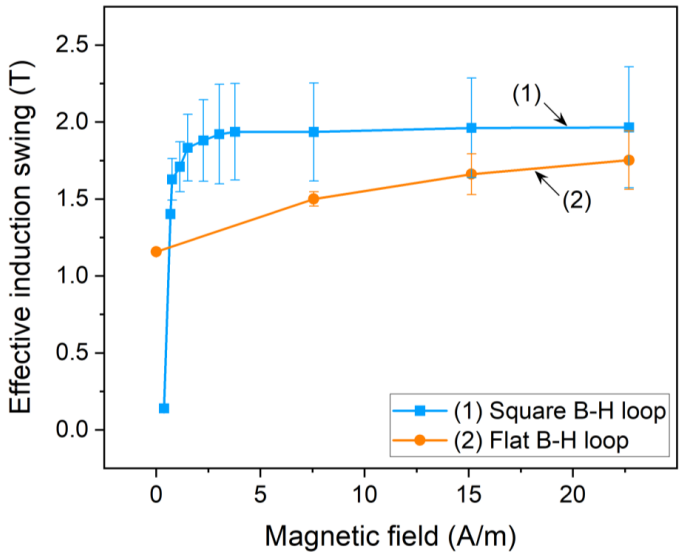

Figure 3.6: Effective induction swing of the SPT cores as a function of the bias magnetizing field H_0 for Finemet FT-3H (1) and Finemet FT-3L (2).

3.2.3.2 Adjustable nanosecond high-voltage generator based on SOS-180-4 and Finement FT-3L

The advantage of the flat B–H loop core is harnessed in the development of an adjustable high-voltage SOS generator. The adjustment of the output voltage is performed by changing the input voltage (i.e., the C1 charging voltage V_{C1}). However, to maintain high efficiency, an optimal pre-magnetizing H_0 should be applied to achieve an optimum saturation. The optimum saturation corresponds to the situation where the core is saturated at the precise moment when the charging voltage of the secondary capacitor V_{C2} reaches its peak amplitude, and the SOS current is zero (Figure 3.3). If saturation occurs too early, it prevents the transmission of all the energy stored in the primary capacitor C1. If saturation occurs too late, part of the energy transmitted to the secondary capacitor C2 is transferred back to the primary circuit. Therefore, a transformer designed to saturate at the optimum moment ensures an efficient and complete energy transfer from C1 to C2.

A preliminary study was carried out to determine the optimal pre-magnetizing H_0 for each V_{C1}. In this preliminary study, the diode is short-circuited and the secondary of the transformer consists of the secondary winding in series with C2. The input voltage V_{C1} is varied from 3 kV to 10 kV. For each input voltage, the magnetic field is tuned to obtain the optimum saturation.

Figure 3.7 presents the three different states of early, optimum, and late saturation. It is shown that the reverse current is at its maximum when the saturation time is optimal. Consequently, the reverse pumping current density required for the SOS effect is improved when operating at the optimum saturation. For the input voltage of 7 kV, the optimum magnetic field applied is 7.5 A/m for which a maximum reversed current amplitude of 1.9 kA is obtained [Figure 3.7, (2)].

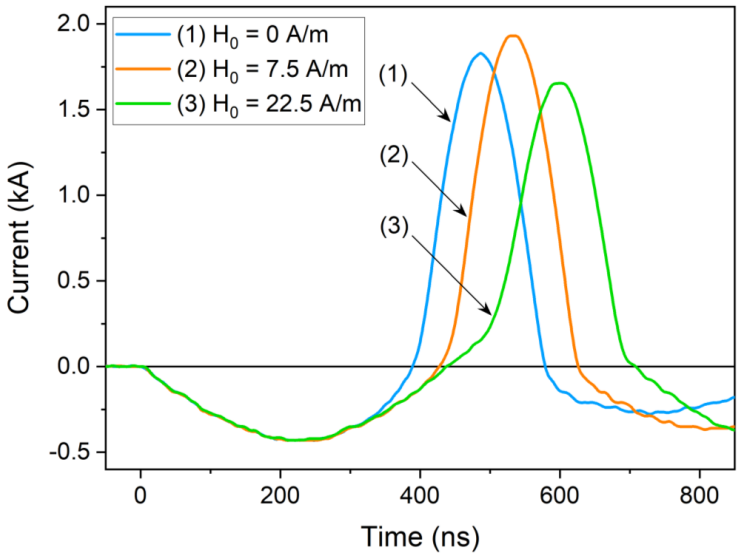

Figure 3.7: Waveforms of the current through C2 at different saturation states of the SPT, depending on the bias magnetic fields H_0: early saturation (1), optimum saturation (2), and late saturation (3).

Based on this preliminary study, an adjustable SOS generator, having an electrical circuit shown in Figure 3.2, was designed and manufactured. The generator components are the same as described in Table 3.2. A single core of Finemet FT-3L is used for the SPT, whose design parameters are as described in Section 3.2.2.2. The resistive load is set to 50 Ω as an example. For insulation considerations, both the diode and the load are immersed in oil. The typical waveforms of V_{C2} and V_R are shown in Figure 3.8 for different values of V_{C1} and H_0.

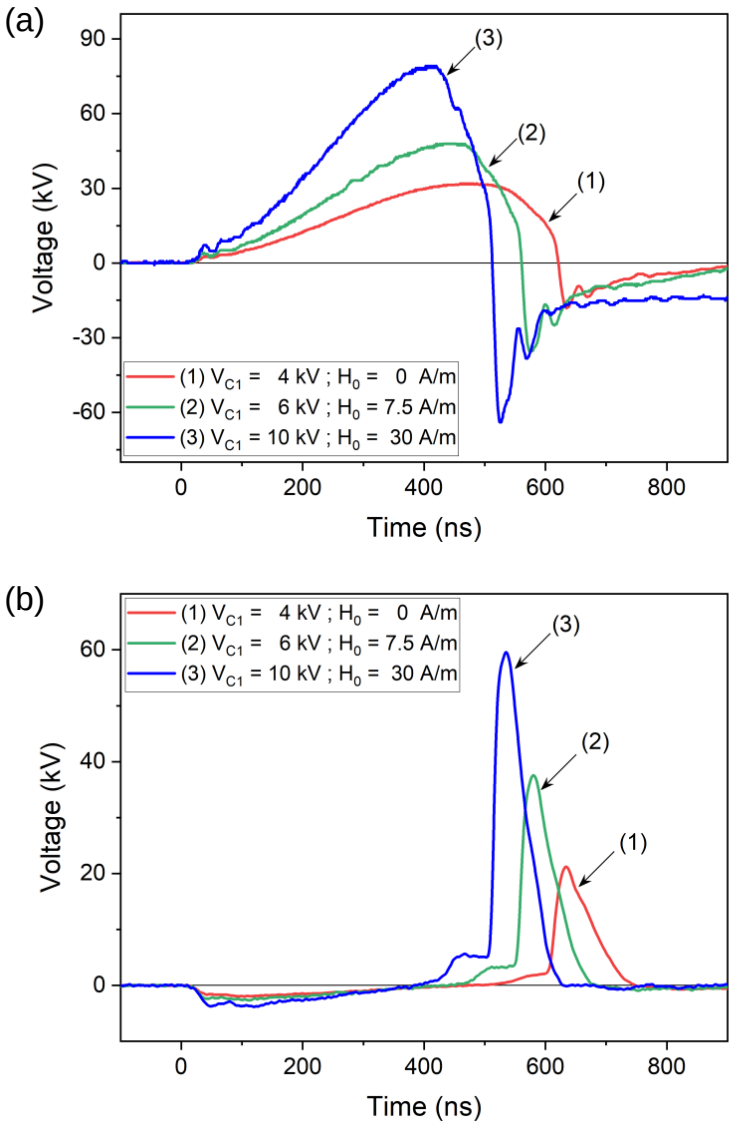

Figure 3.8: Typical waveforms of (a) secondary capacitor voltage V_{C2} (reversed for clarity), and (b) load voltage V_R, when the primary capacitor is charged to 4 kV, 6 kV, and 10 kV.

Figure 3.9 presents the voltage amplitudes of the V_{C2} and V_R as a function of V_{C1}. By varying the input voltage from 3 kV to 10 kV, V_{C2} is changed from 24 kV to 80 kV and the output load voltage is adjusted almost linearly from 10 kV to 60 kV. The proper bias magnetic field is also applied, to ensure the optimum saturation is reached at each operation point. Although the rise time and duration of the load voltage are shortened with the voltage increase, these parameters are hardly tunable in this circuit. Therefore, the adjustment described in this article is only related to the amplitude of the output voltage.

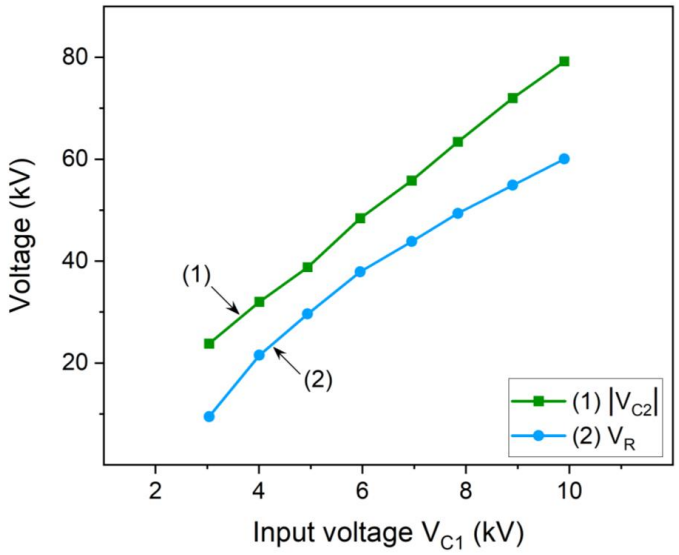

Figure 3.9: Evolution of the amplitude of secondary charging voltage V_{C2} (1), and output load voltage V_R (2), both as a function of the input voltage V_{C1}.

The main characteristics of the adjustable high-voltage generator working on 50 Ω load are summarized in Table 3.4, including the load voltage pulse parameters: peak amplitude V_{C1}, rise time t_r, and FWHM. The transformer efficiency η_{PT} is evaluated as the ratio of primary and secondary stored energy as follows:

$$\eta_{PT} = \frac{E_{C2}}{E_{C1}} \tag{3.8}$$

It is worth noting that this efficiency includes SG losses. Therefore, the ultimate efficiency of the transformer itself is likely to be higher than the calculated η_{PT}.

Table 3.4: Parameters of the adjustable high-voltage generator

V_{C1} (kV)	3	4	5	6	7	8	9	10
H_0 (A/m)	-	-	-	7.5	7.5	15	15	22.5
V_{C2} (kV)	24	32	40	48	56	63	72	80
V_R (kV)	10	22	30	38	44	50	55	60
$t_{r\ (0.1-0.9)}$ (ns)	39	25	22	21	19	18	16	16
$FWHM$ (ns)	85	63	60	57	55	55	54	53
η_{PT} (%)	65	67	66	70	68	69	70	68

Thanks to the regulation of the induction swing, the transformer efficiency remains almost constant for all the output voltages (Table 3.4); its value of up to 70% was calculated using Equation 3.8. For an input voltage in the range from 3 kV to 5 kV, no magnetic field H_0 is applied since the induction swing is higher than required for obtaining an efficient transfer

of the energy from the primary to the secondary capacitor. This causes the SPT to operate in the late saturation state and, consequently, part of the energy is transferred back to the primary. A magnetic field of the same direction as the main pulse could have been applied to regulate the induction swing in order to optimize the overall energy efficiency of the generator at these operation points (from 3 kV to 5 kV). The range of adjustment can also be extended by increasing the voltage capability of the primary capacitor C1.

3.2.3.3 Nanosecond high-voltage generator based on SOS-180-4 and Finemet FT-3H

For this generator, the electrical circuit and parameters are the same as presented in Figure 3.2 and Table 3.2. The SPT of transformation ratio 10 is based on the Finemet FT-3H core (Table 3.3). The generator is designed to operate at a fixed input voltage V_{C1} of 10 kV. The bias field H_0 of 1.5 A/m is required for an operation at the optimum saturation of the core. This applied magnetic field is only 2.5 times higher than the coercive force, but is strong enough to properly bias the square B–H loop core. In such conditions, the effective induction swing of the core is evaluated as ∼2.2 T.

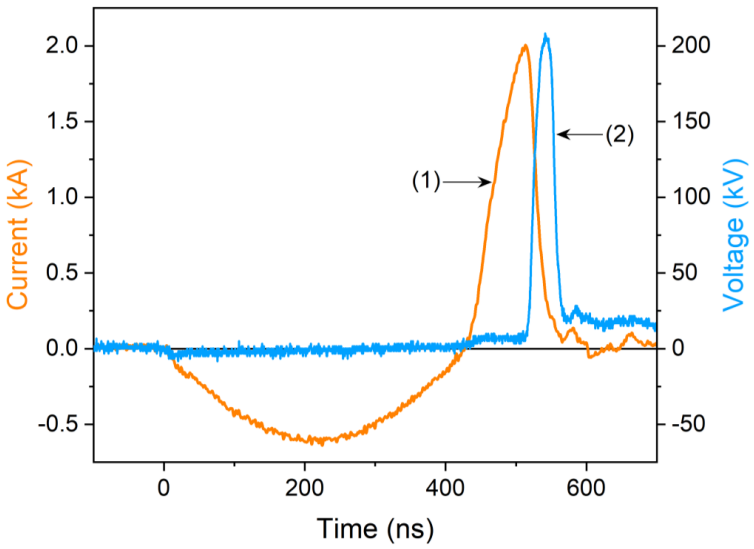

Figure 3.10: Waveforms of the current flowing through the SOS diode I_{SOS} (1), and voltage V_R across R = 1 kΩ (2), for the generator based on the Finemet FT-3H core.

Figure 3.10 illustrates the SOS current and the load voltage impulse obtained for 1 kΩ load. To prevent breakdown, both the diode and the load are immersed in oil. The amplitude and duration of the forward current are 620 A and 430 ns, respectively. The reverse current has a duration of 86 ns and an amplitude of 2 kA. A diode cut-off time of 22 ns is measured. The transformer compression ratio, defined as the ratio of the SOS forward pumping current duration to twice the reverse pumping time ($t^+/2t^-$), is evaluated as 2.5. The ratio of the

reverse-to-forward current amplitude (I^-/I^+) is more than 3.
A load voltage pulse is generated, having an amplitude of 210 kV, a rise time of 16 ns, and an FWHM of 32 ns. The charging voltage V_{C2} of the secondary capacitor is measured as 85 kV. The overvoltage coefficient k_{ov} of the SOS, defined as the ratio of the output voltage V_R to the charging voltage of C2 (V_{C2}), is 2.5.

The influence of the load upon the operation of the generator was also studied for resistive loads varied between 50 Ω and 1 kΩ. In what follows, the energy switching efficiency of the SOS diode is defined as the ratio of the energy transmitted to the load R to the energy stored in the secondary capacitor C2 ($\eta_{SOS} = E_R/E_{C2}$). The load peak power is calculated from the load voltage V_R measured experimentally.

The main results are presented in Figure 3.11. A peak output power P_R of ∼100 MW is obtained with a load of 250 Ω while the maximum voltage of ∼210 kV is obtained for a 1 kΩ load. The change in the load does not influence the transformer efficiency η_{PT}, which is superior to 70% for each load (up to 77% at 1 kΩ). The diode energy switching efficiency reaches its maximum of 54% with a load of 50 Ω and its minimum of only 16% for a load of 1 kΩ (Figure 3.11). Considering that the energy efficiency is highest when the source and load impedances are matched, a higher efficiency should be reached by matching the source impedance, estimated as 32 Ω. On the contrary, the overvoltage coefficient is maximum ($k_{ov} = 2.5$) for 1 kΩ and minimum ($k_{ov} = 0.8$) for the 50 Ω load. This result is in agreement with [7], which reports that the switching efficiency of SOS decreases with the increase of the overvoltage coefficient.

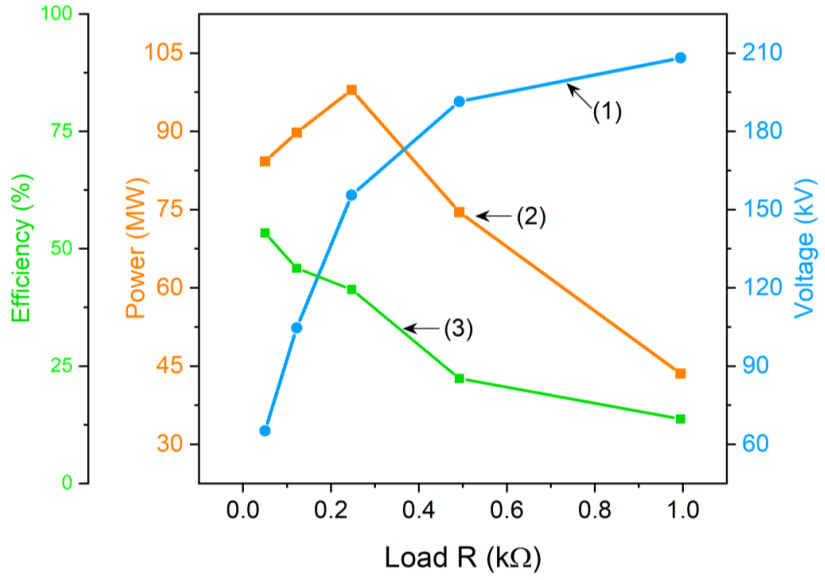

Figure 3.11: Load characteristic of the generator based on the Finemet FT-3H core: load voltage V_R (1), peak power P_R (2), and diode energy switching efficiency η_{SOS} (3), for different values of resistive load ranging from 50 Ω to 1 kΩ.

3.2.4 Conclusion

This article describes the studies related to optimizing the operation of an SPT when used as part of a pulsed-power high-voltage SOS generator. It was found that the saturation flux density is one of the most critical parameters when designing an SPT. The SPT was studied using nanocrystalline magnetic cores of both flat and square hysteresis loops. The comparison of results obtained with these cores reveals the most important features of a hysteresis loop. Thus, it was found that the core presenting the square hysteresis loop, due to the low magnetic field required for the maximum induction swing, is suitable for an operation at a fixed voltage. On the other hand, when using a flat hysteresis loop core, the generator output voltage can be adjusted almost linearly, by tuning the input voltage and by applying the adequate bias magnetic field. It was also demonstrated that a relatively high dc current amplitude is necessary to generate the required magnetic field for higher voltages while using the flat hysteresis loop core. In such a case, proper cooling of the choke must be considered. Two SOS generators based on the aforementioned cores were designed, manufactured, and tested. The control of the bias magnetic field enabled these generators to be operated with a high transformer efficiency of more than 70%. Future research will focus on using a solid-state switch in the primary circuit to improve the overall energy efficiency and address the high PRF operation of these generators. Applying the proposed voltage regulation method to more energetic (>10 J) SOS generators will also be considered.

3.3 Nanocrystalline magnetic cores for SPT

The study of magnetic materials was extended beyond the Finemet FT-3H and Finemet FT-3L nanocrystalline cores described in Section 3.2.2.3 above. A second phase of the study involves two other nanocrystalline materials: Vitroperm 500F (VAC V066) and Vitroperm 500 (VAC W160). The purpose is to evaluate the efficiency of these materials in comparison with Finemet, in order to select the most appropriate option for the design of the 500 kV pulse generator. The experimental setup is identical to the one described in Section 3.2.3.2 where the diode is short-circuited. For clarity, the circuit is shown in Figure 3.12.

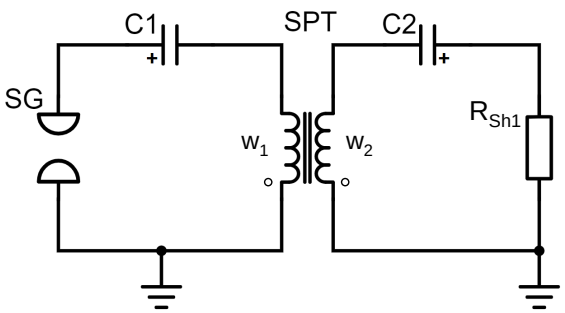

Figure 3.12: Circuit diagram of the short circuit experiment for magnetic cores investigation: C1 = 200 nF, V_{C1} = 3–10 kV, and C2 = 2 nF.

The pulse transformers based on the cores under study are shown in Figure 3.13. The main characteristics of the cores are presented in Table 3.5. To ensure an almost identical material cross-sectional area of about 8 cm^2, SPT-1 comprises three cores, each with nominal dimensions of 160 x 130 x 25 mm^3. In addition, SPT-2 is made up of two U-shape cores, which are tightly joined together. The primary, secondary, and magnetic bias windings of each SPT comprised 1, 10, and 5 turns, respectively.

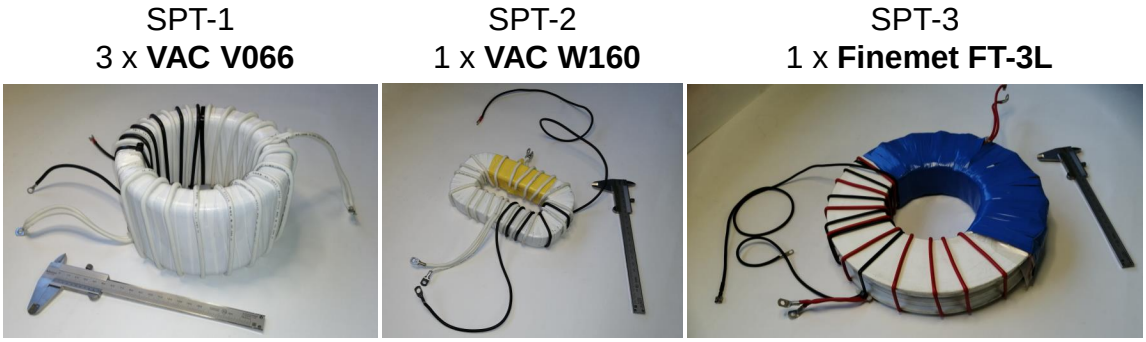

Figure 3.13: Picture of the three SPTs under investigation.

Table 3.5: Parameters of the nanocrystalline materials under investigation

Magnetic cores (SPT-1 | SPT-2 | SPT-3)	VAC V066	VAC W160	FT-3L
Type of nanocrystalline material	Vitroperm 500 F	Vitroperm 500	Finemet FT-3L
Material cross-sectional area S_c (cm^2)	8.22	7.95	8.29
Mean magnetic path length l_m (cm)	45.6	43.2	66.1
Maximum flux density $\Delta B = 2Bs$ (T)	2.4	2.4	2.46
Coercitivity H_c (A/m)	< 0.5	< 0.5	0.6
Thickness of the tape (μm)	18	18	18
Resistivity $\mu\Omega$)	1.15	1.15	1.2
Permeability [μ_{max} $(\times 10^3)$]	20 - 200 (at 50 Hz)	20 - 200 (at 50 Hz)	23 (at 1 kHz)

The main result of the transformer energy efficiency (n_{PT}) (Equation 3.8) is illustrated in Figure 3.14. As mentioned in Section 3.2.3.2, this efficiency also includes the losses of the spark gap switch used as the primary switch. However, as all three transformers were tested under the same conditions, this efficiency can be used as a means of comparison.

All cores show maximum energy efficiency of over 60%, with the Finemet FT-3L core performing better, reaching an efficiency of up to 76%. It should be noted that the reverse current following after core saturation reaches almost 1.6 kA for the Finemet FT-3L while with the two other cores, it was limited to 1.2 kA, even though the forward current was almost the same for the three cores. This difference can be attributed to the greater magnetic path length of the Finemet core, leading to a lower self-inductance of the secondary winding at saturation.

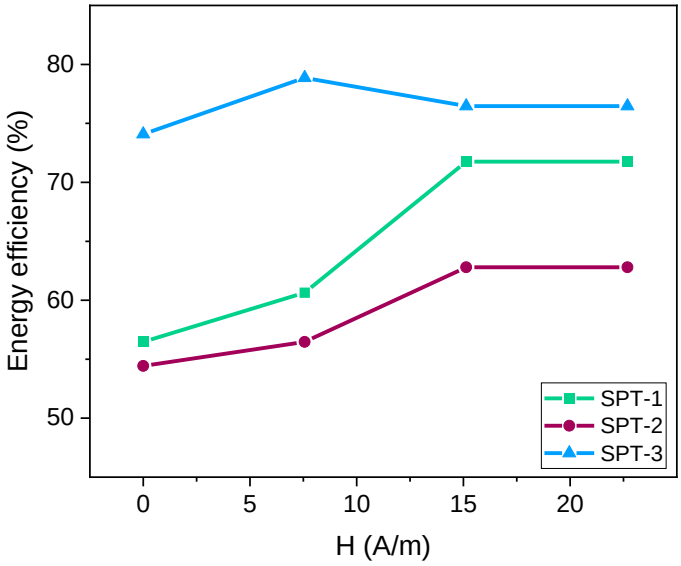

Figure 3.14: Efficiency of the SPTs under different bias magnetic field H_0 when C1 energy is set to 3.6 J.

3.4 Summary and outlook

This study of magnetic cores not only advanced our understanding of the adaptability of magnetic properties, especially hysteresis, to the requirements of pulsed power systems but has also permitted to improve the design of the 40 J test bench. The latter is based on the Finemet FT-3L core, which has shown superior performance among the cores studied and provides better saturation control thanks to its flat hysteresis loop. This test bench will serve for testing OTS diodes at a high-energy level, eventually leading to a 500 kV pulsed power generator prototype based on OTS diodes. The diodes' investigation on the 40 J test bench as well as the generator prototype and its main components are discussed in Chapter 4.

3.5 References

[1] A. F. Colomo, M. J. Barnes, A del Barrio Montañes, T Kramer, and J Ruf, "Measurement and Characterization of a Toroidal Tape Wound Nano-Crystalline Core for the 40Kv Inductive Adder Development At Cern," pp. 4356–4359, 2023. DOI: 10.18429/JACoW-IPAC2023-THPA165. [Online]. Available: https://accelconf.web.cern.ch/ipac2023/doi_per_institute/thpa165/index.html.

[2] N. D. Kallas, R. D. Curry, A. B. Howard, and R. A. Burdt, "Square-Pulse Excitation Characteristics of Vitroperm," *IEEE Transactions on Magnetics*, vol. 53, no. 5, pp. 4–8, 2017, ISSN: 00189464. DOI: 10.1109/TMAG.2016.2601293.

[3] Q. Yuan, Z. Deng, W. Ding, Y. Wang, and J. Wu, "New advances in solid-state pulse generator based on magnetic switches," *Review of Scientific Instruments*, vol. 93, no. 5, p. 051 501, May 2022, ISSN: 0034-6748. DOI: 10.1063/5.0079583.

[4] Colonel Wm. T. McLyman, *Design Handbook Transformer and Inductor Design Handbook Fourth Edition*. 2011, p. xi, ISBN: 9781439836880.

[5] Hitachi Metals Ltd, "Nanocrystalline soft magnetic material FINEMET®," Tech. Rep., 2005. [Online]. Available: http://www.hilltech.com/pdf/hl-fm10-cFinemetIntro.pdf (visited on 05/25/2022).

[6] S. K. Lyubutin, G. Mesyats, S. Rukin, B. Slovikovskii, and A. Turov, "New solid state opening switches for repetitive pulsed power technology," in *11th International Conference on High-Power Particle Beams*, 1996, pp. 135–138.

[7] S. N. Rukin, "Pulsed power technology based on semiconductor opening switches: A review," *Review of Scientific Instruments*, vol. 91, no. 1, p. 011 501, Jan. 2020, ISSN: 0034-6748. DOI: 10.1063/1.5128297.

[8] S. Y. Sokovnin and M. E. Balezin, "Surface irradiation installation for eggs based on URT-0,5M accelerator," *Radiation Physics and Chemistry*, vol. 196, p. 110 137, Apr. 2022, ISSN: 0969806X. DOI: 10.1016/j.radphyschem.2022.110137.

[9] S. Y. Sokovnin and M. E. Balezin, "Repetitive nanosecond electron accelerators type URT-1 for radiation technology," *Radiation Physics and Chemistry*, vol. 144, no. August 2017, pp. 265–270, Mar. 2018, ISSN: 0969806X. DOI: 10.1016/j.radphyschem.2017.08.023.

[10] T. Sugai, W. Liu, A. Tokuchi, W. Jiang, and Y. Minamitani, "Influence of a Circuit Parameter for Plasma Water Treatment by an Inductive Energy Storage Circuit Using Semiconductor Opening Switch," *IEEE Transactions on Plasma Science*, vol. 41, no. 4, pp. 967–974, Apr. 2013, ISSN: 0093-3813. DOI: 10.1109/TPS.2013.2251359.

[11] G. Wang, J. Su, Z. Ding, X. Yuan, and Y. Pan, "A semiconductor opening switch based generator with pulse repetitive frequency of 4 MHz," *Review of Scientific Instruments*, vol. 84, no. 12, p. 125 102, Dec. 2013, ISSN: 0034-6748. DOI: 10.1063/1.4833683.

[12] G. H. Rim, B. D. Min, E Pavlov, and J. H. Kim, "Repetitive Nanosecond All-Solid-State Pulse Generator Using Magnetic Switch and SOS Diodes," in *2005 IEEE Pulsed Power Conference*, IEEE, Jun. 2005, pp. 1069–1072, ISBN: 0-7803-9189-6. DOI: 10.1109/PPC.2005.300504.

[13] A. B. J. M. Driessen, E. J. M. van Heesch, T. Huiskamp, F. J. C. M. Beckers, and A. J. M. Pemen, "Compact Pulse Topology for Adjustable High-Voltage Pulse Generation Using an SOS Diode," *IEEE Transactions on Plasma Science*, vol. 42, no. 10, pp. 3083–3088, Oct. 2014, ISSN: 0093-3813. DOI: 10.1109/TPS.2014.2314686.

[14] S. K. Lyubutin, M. Pedos, A. Ponomarev, *et al.*, "High efficiency nanosecond generator based on semiconductor opening switch," *IEEE Transactions on Dielectrics and Electrical Insulation*, vol. 18, no. 4, pp. 1221–1227, Aug. 2011, ISSN: 1070-9878. DOI: 10.1109/TDEI.2011.5976119.

[15] A. I. Gusev, S. K. Lyubutin, A. V. Ponomarev, S. N. Rukin, and B. G. Slovikovsky, "Semiconductor opening switch generator with a primary thyristor switch triggered in impact-ionization wave mode," *Review of Scientific Instruments*, vol. 89, no. 11, p. 114 702, Nov. 2018, ISSN: 0034-6748. DOI: 10.1063/1.5052530.

[16] G. A. Mesyats, *Pulsed Power*. Boston, MA: Springer US, 2005, ISBN: 978-0-306-48653-1. DOI: 10.1007/b116932.

[17] T. Sakugawa and H. Akiyama, "An all-solid-state pulsed power generator using a high-speed gate-turn-off thyristor and a saturable transformer," *Electrical Engineering in Japan*, vol. 140, no. 4, pp. 17–26, Sep. 2002, ISSN: 0424-7760. DOI: 10.1002/eej.2006.

[18] D. Zhang, Y. Zhou, J. Wang, and P. Yan, "A compact, high repetition-rate, nanosecond pulse generator based on magnetic pulse compression system," *IEEE Transactions on Dielectrics and Electrical Insulation*, vol. 18, no. 4, pp. 1151–1157, Aug. 2011, ISSN: 1070-9878. DOI: 10.1109/TDEI.2011.5976109.

[19] H. Akiyama, T. Sakugawa, T. Namihira, K. Takaki, Y. Minamitani, and N. Shimomura, "Industrial Applications of Pulsed Power Technology," *IEEE Transactions on Dielectrics and Electrical Insulation*, vol. 14, no. 5, pp. 1051–1064, Oct. 2007, ISSN: 1070-9878. DOI: 10.1109/TDEI.2007.4339465.

[20] Z. Zhang and X. Tan, "Review of High Power Pulse Transformer Design," *Physics Procedia*, vol. 32, pp. 566–574, 2012, ISSN: 18753892. DOI: 10.1016/j.phpro.2012.03.602.

[21] L. Rong and Q. Rong, "Research on pulse power based on saturable pulse transformer and magnetic switch," *The Journal of Engineering*, vol. 2018, no. 10, pp. 1384–1388, Oct. 2018, ISSN: 2051-3305. DOI: 10.1049/joe.2018.5026. [Online]. Available: https://onlinelibrary.wiley.com/doi/10.1049/joe.2018.5026.

[22] L. Pecastaing, M. Rivaletto, A. S. de Ferron, R. Pecquois, and B. M. Novac, "Development of a 0.6-MV Ultracompact Magnetic Core Pulsed Transformer for High-Power Applications," *IEEE Transactions on Plasma Science*, vol. 46, no. 1, pp. 156–166, Jan. 2018, ISSN: 0093-3813. DOI: 10.1109/TPS.2017.2781620.

[23] S. Li, J. Gao, H. Yang, *et al.*, "Investigation on Adjustable Magnetic Pulse Compressor in Power Supply System," *IEEE Transactions on Power Electronics*, vol. 34, no. 2, pp. 1540–1547, Feb. 2019, ISSN: 0885-8993. DOI: 10.1109/TPEL.2018.2830106.

[24] J. Choi, "Introduction of the Magnetic Pulse Compressor (MPC) - Fundamental Review and Practical Application," *Journal of Electrical Engineering and Technology*, vol. 5, no. 3, pp. 484–492, Sep. 2010, ISSN: 1975-0102. DOI: 10.5370/JEET.2010.5.3.484.

[25] J. Holma and M. J. Barnes, "Prototype Inductive Adders With Extremely Flat-Top Output Pulses for the Compact Linear Collider at CERN," *IEEE Transactions on Plasma Science*, vol. 46, no. 10, pp. 3348–3358, Oct. 2018, ISSN: 0093-3813. DOI: 10.1109/TPS.2018.2836310. [Online]. Available: https://ieeexplore.ieee.org/document/8384315.

[26] M. J. Barnes, W. Bartmann, F. Burkart, *et al.*, "Future circular collider injection and extraction kicker topologies and solid state generators," *Physical Review Accelerators and Beams*, vol. 22, no. 7, p. 071 001, Jul. 2019, ISSN: 2469-9888. DOI: 10.1103/PhysRevAccelBeams.22.071001. [Online]. Available: https://link.aps.org/doi/10.1103/PhysRevAccelBeams.22.071001.

[27] S. R. Korzhenevskiy, A. A. Komarskiy, A. S. Chepusov, V. A. Bessonova, and V. N. Titov, "Output voltage adjustment of a pulsed high-voltage nanosecond generator with inductive energy storage and a solid-state switching system," *Instruments and Experimental Techniques*, vol. 60, no. 1, pp. 46–49, Jan. 2017, ISSN: 0020-4412. DOI: 10.1134/S0020441217010213.

[28] R. Burdt, R. D. Curry, K. F. McDonald, P. Melcher, R. Ness, and C. Huang, "Evaluation of nanocrystalline materials, amorphous metal alloys, and ferrites for magnetic pulse compression applications," *Journal of Applied Physics*, vol. 99, no. 8, p. 08D911, Apr. 2006, ISSN: 0021-8979. DOI: 10.1063/1.2173214.

[29] T. Filchev, F. Carastro, P. Wheeler, and J. Clare, "High voltage high frequency power transformer for pulsed power application," in *Proceedings of 14th International Power Electronics and Motion Control Conference EPE-PEMC 2010*, IEEE, Sep. 2010, pp. 165–170, ISBN: 978-1-4244-7856-9. DOI: 10.1109/EPEPEMC.2010.5606517.

[30] M. R. Degnon, A. I. Gusev, A. S. de Ferron, *et al.*, "Off-the-Shelf Diodes as High-Voltage Opening Switches," *IEEE Transactions on Plasma Science*, vol. 50, no. 10, pp. 3384–3392, Oct. 2022, ISSN: 0093-3813. DOI: 10.1109/TPS.2022.3177702.

[31] E. A. Alichkin, S. K. Lyubutin, A. V. Ponomarev, S. N. Rukin, and B. G. Slovikovskii, "Formation of Short Pulses with a Subnanosecond Rise Time and a Peak Power of Up to 1 GW by a Semiconductor Avalanche Sharpener," *Instruments and Experimental Techniques*, vol. 45, no. 4, pp. 535–539, 2002. DOI: 10.1023/A:1019798805905.

[32] S. Nakajima, S. Arakawa, Y. Yamashita, and M. Shiho, "Fe-based nanocrystalline FINEMET cores for induction accelerators," *Nuclear Instruments and Methods in Physics Research Section A: Accelerators, Spectrometers, Detectors and Associated Equipment*, vol. 331, no. 1-3, pp. 318–322, Jul. 1993, ISSN: 01689002. DOI: 10.1016/0168-9002(93)90066-Q.

Chapter 4

Design and characterization of the 500 kV generator prototype (GO-SSOS)

Chapter 4

Design and characterization of the 500 kV generator prototype (GO-SSOS)

The prototype of the 500 kV Generator based on an Off-the-shelf Solid-State Opening Switch (GO-SSOS) is the main focus of this chapter. Following the methodology described in Chapter 1, the design has been implemented, based on a single magnetic element. The design considerations and generator-associated systems are discussed in this chapter, which is divided into two parts. The first part gives an overview of the system and its various auxiliary components essential to its operation. The description of the system's important components, including the Current Viewing Resistor (CVR) employed as diagnostics and the choke used to protect the magnetic bias circuit, is presented. The first part essentially gathers complementary information to the second part based on our recently published article. This article is devoted to the design and characterization of the generator prototype, giving an insight into its development process and the performance evaluation of an OTS opening switch. Moreover, an example of the generator application such as corona discharge is demonstrated in the article.

4.1 General presentation of the system

A schematic diagram of the complete system is presented in Figure 4.1. This system can be divided into three sub-systems. The first one consists of the main components including the primary thyratron closing switch S1, the SPT, the primary and secondary capacitor banks C1 and C2, the secondary opening switch SOS, and the load R_L. The operation of this sub-system is described in Section 4.2.2.

The second sub-system comprises the auxiliary components, essentially. It encompasses a capacitor charger (CCR50KV-4J) and a magnetic bias circuit including the choke CK. The bias circuit provides a continuous magnetic field to pre-magnetize the cores of SPT for its optimum saturation, as described in Chapter 2. Additionally, this second sub-system includes an RD-circuit (D1 and R1) to protect the thyratron. The choke CK of the magnetic bias circuit as well as R1 and D1 protective elements are described in Section 4.1.3.

The third sub-system is dedicated to the diagnostics and control of the system units. First, the diagnostics include two current shunts (or CVRs) R_{Sh1} and R_{Sh2} (described in Section 4.1.2), and additional current monitor and voltage probes which are described in Section 4.2.2. Second, the control system encompasses the Thyratron Driving System (TDS), which supplies the thyratron's cathode and reservoir heating currents (CH and RH in Figure 4.1). TDS also provides the thyratron trigger pulses into G1 and G2 grids using a standard North Star TT-G1/G2 Driver Board (DB) [1]. The latter incorporates an optical fiber receiver for remote control. Last but not least, a Trigger Generator (TG) is used to generate DB optical triggering signal, and to drive the charger, setting its operating rate.

The whole system operation is controlled using two 16 MHz Atmega 328P microcontroller-based Arduino boards. The first board, integrated into TDS, monitors the thyratron's heating currents and the readiness of the thyratron driver DB. The second board is embedded into TG, which controls both the capacitor charger and DB.

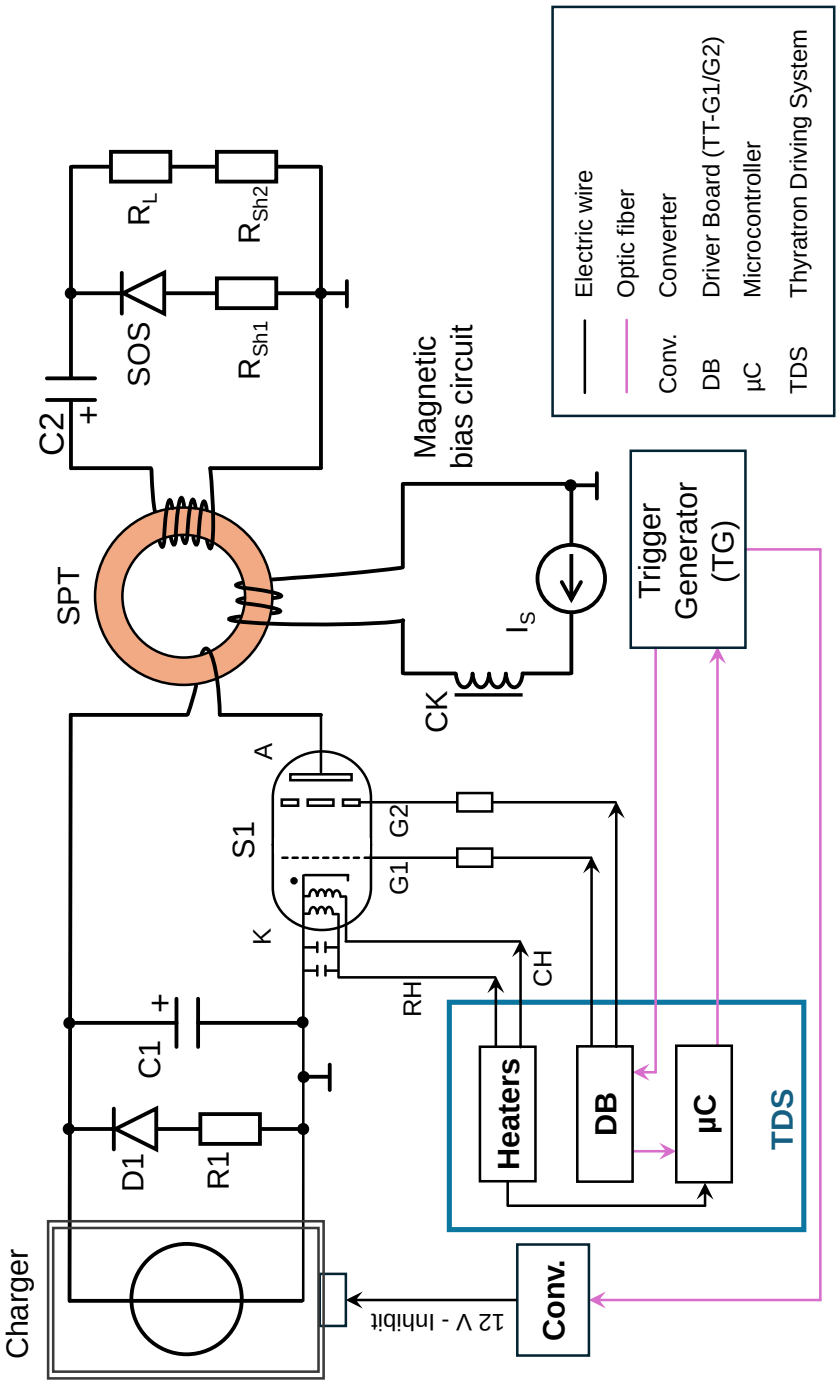

Figure 4.1: Schematic diagram of the 500 kV GO-SSOS.

4.1.1 Operating process description

Figure 4.2 provides a simplified flow chart of the generator operation. The process begins by powering up the thyratron driving system to preheat the thyratron reservoir and cathode. This crucial step takes 15 minutes. This preheating phase ensures optimum gas pressure and efficient electron emission from the thermionic cathode [2].

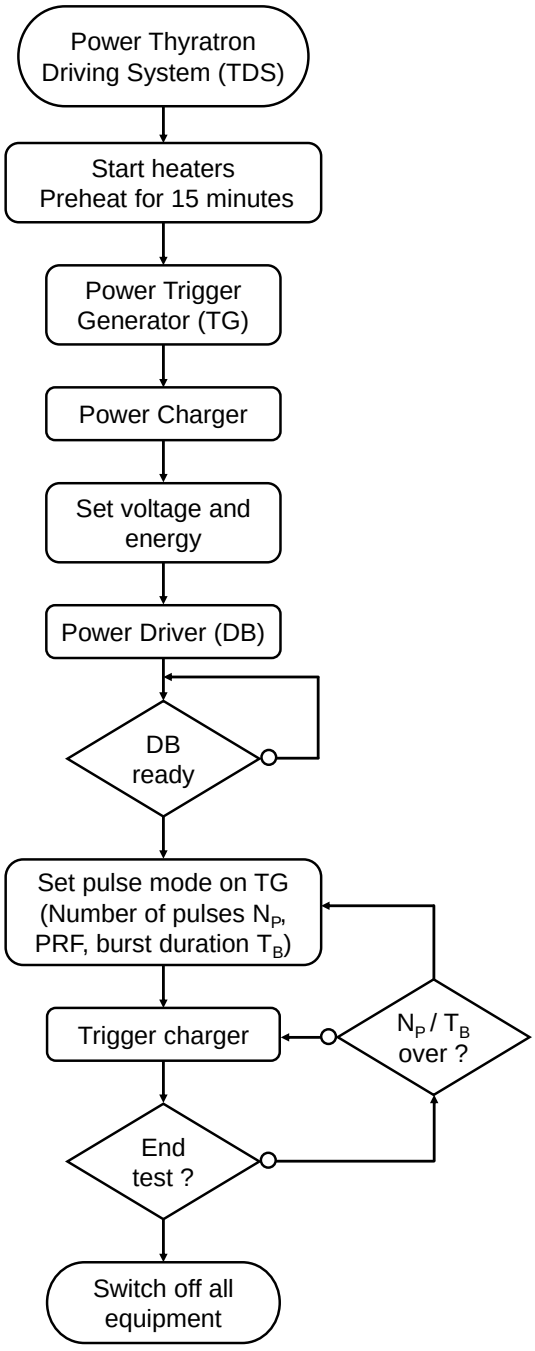

Figure 4.2: Simplified flow chart of the system operation.

Next, TG is switched on to provide an inhibition signal enabling remote control of the capacitor charger. In this inhibition mode, the charger no longer supplies high voltage as long as the inhibition signal remains active, i.e. $V_{inh} = 12\ V$ (high state). The user then sets the charger output voltage, defining the energy to be stored in C1. DB is further switched on and, once its embedded main capacitors [1] are charged, a ready optical signal is automatically transmitted to TG which thereafter enables the user to set the operating mode.

TG shown in Figure 4.3 is designed to provide three different modes of operation: single, burst, and continuous. In the main menu, users can set parameters such as number of pulses, burst duration, and/or PRF. Once the pulse parameters have been set, the user can trigger the system, delivering high-voltage pulses into the load. Thyratron heating currents and DB readiness are continuously monitored to prevent generator failure.

Figure 4.3: Picture of the trigger generator TG.

The time sequence from the user command to the triggering of the thyratron is shown in Figure 4.4. When the user runs TG (at t_0), the first output of TG (TG-Out1 optical signal) responsible for controlling the charger, changes its state from 1 to 0. This change causes the charger's inhibition voltage to fall from 12 V to 0 V after a delay $t_1 = 25$ µs. Then, once the inhibition voltage reaches 0, the charger delivers energy to capacitor C1 for the duration t_2, which is defined in the program of the microcontroller inside TG.

On completion of C1 charging, an optical pulse of duration t_4 is initiated from the second output of TG (TG-Out2) after a delay $t_3 = 500$ ns. This pulse activates the generation of the G1 and G2 voltage pulses by DB. The resulting double pulse triggers the thyratron, which switches, enabling energy transfer from the primary capacitor C1 to the secondary capacitor C2 via SPT. The subsequent processes in the high-voltage section of the generator automatically proceed as described further in Section 4.2.2.

The total delay between the user command and the thyratron triggering is about 15 ms. This duration is limited by the time required to charge the primary capacitor C1 to its specified energy of about 40 J. Consequently, the capacitor charger appears to be one of the main elements limiting the PRF of the system.

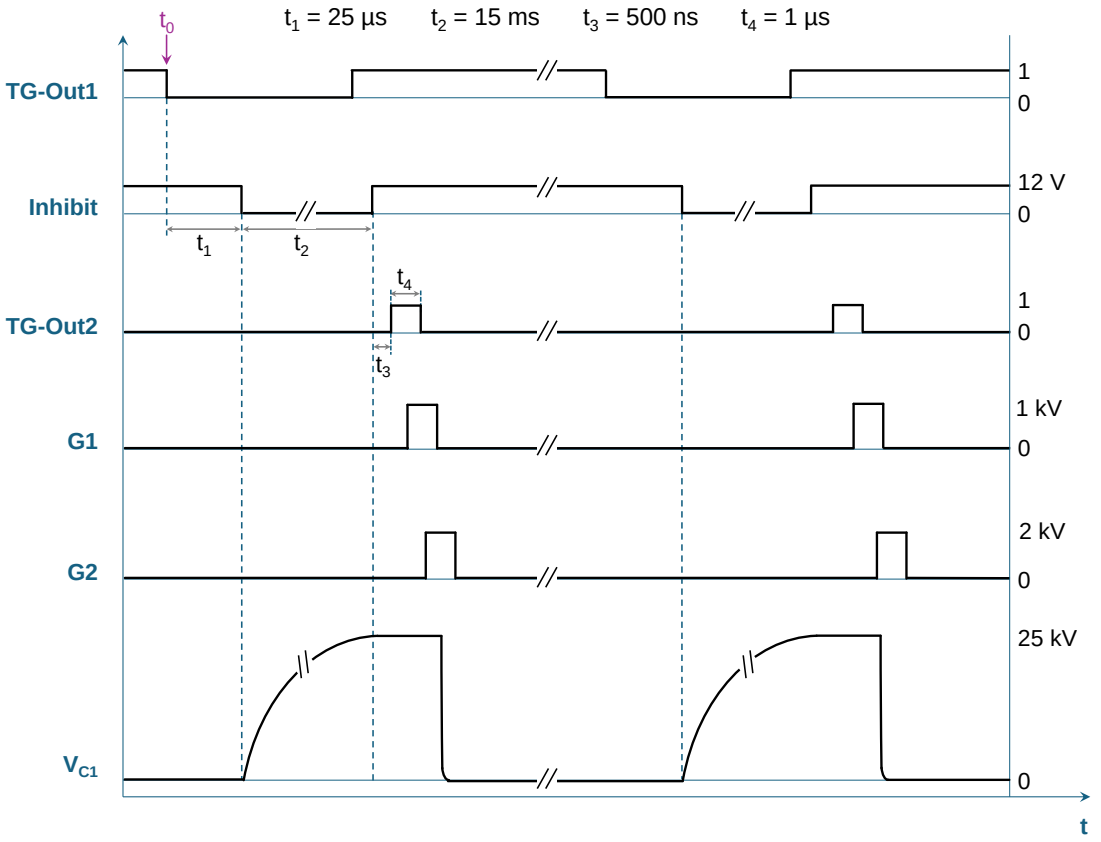

Figure 4.4: System trigger sequence showing two successive triggerings.

4.1.2 Current Viewing Resistor (CVR)

In pulsed power systems, the challenge is not only to generate high-voltage pulses over a short period of time, but also to measure accurately these pulses. To meet this need, CVR, a.k.a. current shunts, were built and tested as a part of this thesis. The CVR is a low-inductive resistor with well-known and stable resistance used to sense current by measuring the voltage drop across it. For accurate measurements, the CVR must exhibit a stable resistance value, negligible inductance, and good thermal stability according to [3], [4].

Two CVRs of 0.5 Ω and 0.15 Ω have been made to independently measure the current flowing through the diode and the load. The design of these CVRs is inspired by [5], who originally developed this type of shunt capable of measuring rise times of less than one nanosecond. Figure 4.5 shows a visual representation of these CVRs. A coaxial shape is adopted to minimize inductance. Each CVR consists of eighteen RCC050 carbon composition resistors (0.5 W ±5%) connected in parallel. One terminal of the resistors is connected to the high-voltage connector HV, and the other to the grounded CVR outer body in brass (main support in Figure 4.5). An N-type connector integrated into the CVR allows connection via a coaxial cable for measurement on an oscilloscope, using high-voltage and high-bandwidth attenuators.

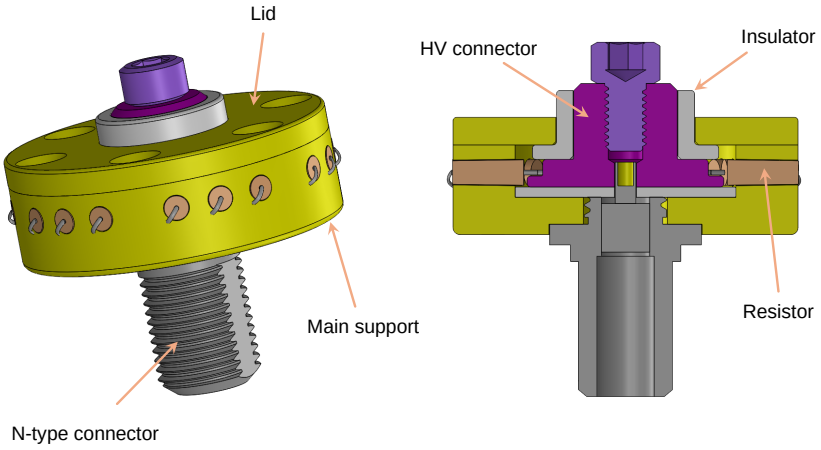

Figure 4.5: Appearance of the CVR designed for nanosecond current measurements.

According to the RCC050 data sheet, these carbon resistors are non-inductive and are designed for high energy dissipation with excellent pulse characteristics and stability. The combined nominal power dissipation of the eighteen resistors in the CVR is 9 W for a nominal dc applied voltage. If this voltage is applied for 1 s, the energy absorbed by the resistors would be 9 J. However in pulsed mode, as the duration is reduced to hundreds of nanoseconds in our case, the power capability of the resistors increases. For instance, in our previous study, a single 10 Ω RCC050 resistor demonstrated its ability to conduct a current with a peak amplitude of 800 A with an FWHM of about 700 ns and withstand an 8 kV applied voltage pulse. The peak power dissipated and the energy absorbed by the single resistor were 6.4 MW and about 6 J, respectively.

Based on these results, the energy rating of the CVR with eighteen RCC050 can rise to more than 100 J in pulsed mode. It is relevant to highlight that the expected maximum amplitude and duration of the current through the load, are less than 3 kA and about 100 ns, respectively. Therefore, the maximum energy to be absorbed by the CVR in this work is less than 1 J.

The CVR bandwidth is another key factor to consider for an accurate measurement. In general, the main parameter limiting the bandwidth in CVRs are their parasitic inductance and capacitance. The latter are minimized in our CVRs due to their compact coaxial geometry and the use of low-inductive resistors.

In this work, the CVR has been calibrated using an FID pulse generator (FPG 5-1PM1) providing a voltage pulse with a sub-nanosecond rise time (∼0.5 ns), and a duration of about 1 ns. The diagram of the calibration experiment is shown in Figure 4.6.

To validate the CVR measurements, a capacitive voltage line divider LGE-8 [6] made in-house (VP in Figure 4.6) is used. VP features an attenuation of -46 dB and a measurement bandwidth of up to 4 GHz. The transmission coefficient S21 of VP is shown in Figure 4.7.

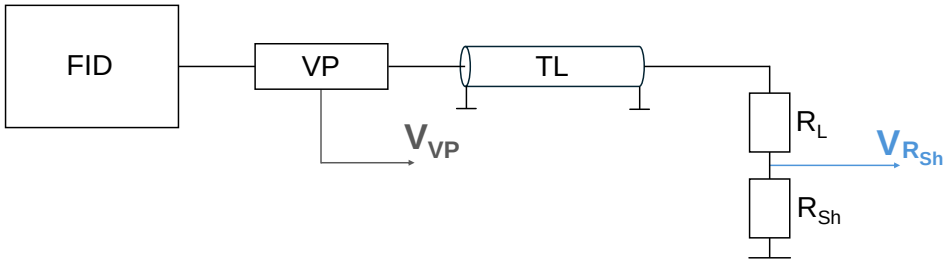

Figure 4.6: Diagram of the CVR calibration experiment showing FID generator, homemade voltage probe VP (-46 dB, 4 GHz), transmission line TL (50 Ω, 3 m), dummy load (R_L = 55 Ω), and CVR or shunt (R_{Sh} = 0.5 Ω).

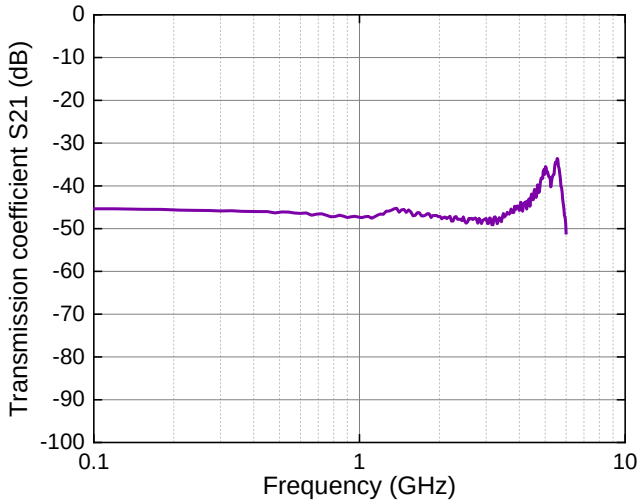

Figure 4.7: Transmission coefficient S21 for the capacitive divider VP [7].

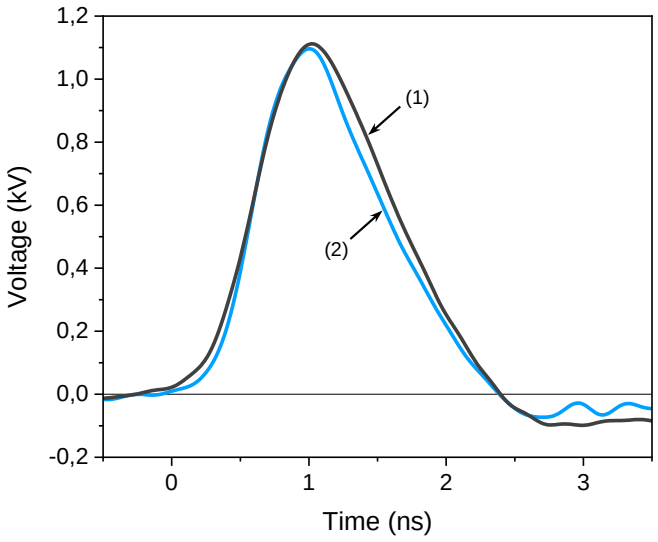

Figure 4.8: FID generator output voltage waveform measured using VP (1) and R_{Sh} (2).

Figure 4.8 shows the FID generator output voltage measured using VP, and the load voltage obtained from CVR (R_{Sh}) current measurement in the calibration experiment of Figure 4.6. The difference in voltage amplitude is around 1% and the time difference is about 10%. Based on these measurements, the operational bandwidth of the CVR is estimated to be at least 700 MHz. Thus, the usable rise time of 0.5 ns is verified for the CVRs employed in this work to measure output voltage pulses with a rise time of about twenty nanoseconds.

4.1.3 Protection components

The generator prototype is equipped with protection systems which are described in the current section. An RD-circuit (D1 and R1 in Figure 4.1) is connected in parallel with the primary capacitor C1, providing a direct path to the reverse current, and preventing reverse current from flowing through the thyratron switch in case of a circuit failure or mismatched load. D1 consists of four series-connected diodes (D1481N), each in parallel with a 5 MΩ resistor. The blocking voltage of the diode stack is about 30 kV. A ceramic resistor of about 3 Ω is inserted in series to the diode.

Furthermore, the magnetic bias circuit includes the choke CK, whose main function is to protect the IPS 303A current source used to generate the bias magnetic field. The choke, consisting of a magnetic core featuring a single winding of multiple turns, is used to block or decouple high-frequency current while passing dc. The purpose of CK is to block the high voltage induced across the bias winding during the energy transfer. For instance, when C1 is charged to 25 kV, a voltage reaching up to 125 kV can be induced across the 5-turn bias winding after the thyratron is triggered, risking damage to the power supply in the absence of CK. The ideal choke should permanently have a high inductance to block the high-frequency current pulse, thus its magnetic material should not saturate. Choke parameters, including the number of turns, cross-sectional area of the core, and saturated induction of the magnetic material, must therefore be maximized. The VAC W160 cut core (described in Chapter 3) is used for CK which features as many turns as one can put on the core length. The choke inductance is measured to be about 300 mH.

With the generator prototype and its main components introduced, the next section focuses on characterizing the generator as well as examining the operation of an OTS diode at an energy of up to 40 J. This work is the logical culmination of the thesis, addressing the main challenge of developing a 500 kV nanosecond generator based on OTS components. The material presented in this section is based on our article:

M. R. Degnon, A. I. Gusev, A. Silvestre de Ferron, L. Pécastaing, A. Piaser, F. Bayol, and B. M. Novac, *"A 500-kV Nanosecond Pulse Generator Based on an Off-the-Shelf Solid-State Opening Switch,"* accepted in May 2024, for inclusion in a future issue of IEEE Transactions on Plasma Science, DOI: 10.1109/TPS.2024.3403379.

4.2 A 500 kV nanosecond pulse generator based on an OTS solid-state opening switch

Abstract: This article investigates the use of OTS diodes as opening switches in a 500 kV nanosecond pulsed power generator. A 40 J test bench based on an SPT and on a primary thyratron switch is designed to evaluate the performance of the OTS diodes in comparison with standard SOS diodes. A distinguishing feature of the proposed circuit is the adjustability of the output pulse energy, which is achieved using flat hysteresis loop magnetic cores and variable reset magnetic field. The study confirms the operation of OTS diodes as an opening switch, although highlighting differences in the reverse current conduction that affect the generated voltage pulse characteristics. Based on the successful operation of the OTS diodes, a 500 kV pulsed power GO-SSOS was developed. The GO-SSOS provides output voltages of 100–500 kV across a 50–1000 Ω resistive load, with a pulse width of about 100 ns and a rise time of less than 40 ns. The generator achieves a peak power of 335 MW and demonstrates an overall energy efficiency in the range of 30% to 70% depending on the load. Operation at a PRF of 60 Hz is presented, showing a good reproducibility of the pulses with an amplitude and duration deviation of about 2% and 10%, respectively. No degradation of the OTS diodes has been observed after the tests (more than 1000 pulses). As an example of the possible applications of the GO-SSOS, corona discharge in the air was performed, also proving the stability of all the systems under conditions of strong electromagnetic interference.

4.2.1 Introduction

Interest in the field of pulsed power is constantly growing, mainly due to its wide range of potential applications across various fields. While historically concentrated within the military sector [8], recent decades have witnessed a notable expansion into civilian domains. The versatility of pulsed power systems is highlighted by their utility in numerous applications including gas and liquid treatment [9], exploration of electrophysical properties of semiconductors and dielectrics [10], electron beams and radiation techniques for sterilization and food processing [11], [12], as well as the electropermeabilization of biological cells using pulsed electric field techniques [13]. This expanding scope of application has made pulsed power generators increasingly attractive to industry. In particular, the use of electrical energy instead of chemical processes in sterilization technology [14] motivates this work.

In industrial settings, pulsed power generators have to comply with stringent requirements, including high reliability, long lifetime, maintenance-free operation, high PRF, and adjustable output parameters, to suit specific needs. Semiconductor devices perfectly match these criteria. However, when it comes to generating repetitive high-voltage pulses of several hundred kilovolts, only a few solid-state solutions are capable of doing so. Among these are the SOS [15], solid-state Marx [16], and magnetic switch-based [17] pulsed power generators. SOS generators stand out, in particular, for their ability to produce nanosecond megavolt

voltage impulses, generate gigawatt peak powers, and operate at a PRF of several kilohertz [18]. These generators use IES, which has a higher energy density compared to CES systems according to [19].

The heart of SOS generators is the SOS diode, which consists of a stack of silicon diodes designed to interrupt high currents with densities superior to 1 kA/cm^2 in nanosecond duration [18]. Compared to standard rectifying diodes, SOS diodes have a specific "$p^+ - p - n - n^+$" doping profile, characterized by a deep $p-n$ junction of about 200 µm depth [20]. The number of $p-n$ junctions in an SOS stack determines the rated voltage of the switch, hence it must be increased to block high voltages. Moreover, the energy capacity of SOS diodes can be enhanced by parallel connections of the diodes to avoid thermal breakdown, which can occur at current densities close to 100 kA/cm^2 [18], [21]. Additionally, appropriate diode cooling enables operation at high PRF, increasing the average power, which is crucial for industrial applications.

Although SOS generators are an ideal candidate for repetitive nanosecond high-voltage generation, the lack of SOS diode manufacturers prevents their widespread use. Therefore, the present study investigates the feasibility of using OTS diodes as an opening switch in pulsed power systems. Our previous study [22] has revealed the potential of OTS diodes to operate in the opening switch mode at switching energy below 10 J. Diodes with blocking voltages of a few kilovolts, maximum forward surge currents of up to a few kiloamperes, and recovery times reaching several microseconds were of interest. In this work, avalanche, fast recovery, rectifier, and TVS diodes were tested. The results indicate that the most promising OTS diodes are TVS and fast recovery diodes. The OTS-100 (100 kV max) diode assembled using fast recovery diodes has succeeded in generating a voltage pulse of amplitude reaching 90 kV with a rise time of 20–35 ns and an FWHM within 60–105 ns.

Building on this work, the present study focuses on switching energies higher than 10 J, with the aim of generating voltage pulses of up to 500 kV at a PRF of several tens of Hz, using the OTS fast recovery diodes. To this end, a 40 J test bench is developed.

This article is organized as follows. An overview of the experimental setup and the design of the components is presented in Section 4.2.2. The comparative analysis of the OTS and SOS diodes across various operation points is given in Section 4.2.3. The 500 kV pulsed power generator prototype based on the OTS diode is presented in the same section. Finally, a summary is provided in Section 4.2.4.

4.2.2 Circuit principle and generator design

4.2.2.1 Circuit layout and operation principle

The high-voltage part of the test bench is illustrated in Figure 4.9. It includes a step-up SPT, which transfers energy from the primary capacitor C1 into the secondary capacitor C2 in resonance mode, providing the forward and reverse pumping of the opening switch diode SOS. When the diode switches, interrupting the current, the energy is delivered to the resistive load

R_L, forming the output voltage pulse.

To be energy-efficient, the circuit uses a single magnetic element – SPT. This approach, however, requires a primary switch S1, capable of withstanding high voltage, high current, and high dI/dt. Although there are solid-state solutions of S1 [23], [24], a thyratron is used in this work for simplicity. The dump resistor R1 and protective diode D1 are installed to prevent the reverse voltage across the thyratron in the event of a circuit failure or mismatched load. In order to ensure efficient transmission of the energy from the primary to the secondary capacitor, the magnetic bias circuit consisting of the current source I_s, choke CK, and bias winding w_b, is used to magnetize the SPT core before each pulse. A detailed analysis of the magnetic bias circuit utility is available in [25].

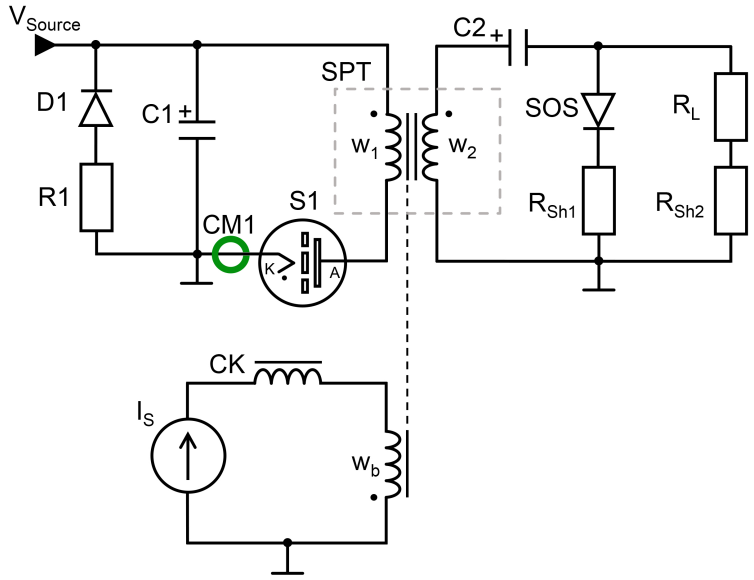

Figure 4.9: Circuit diagram of the high-voltage part of the opening switch test bench with energy stored in C1 of up to 40 J. Description of the components is provided in the text.

The circuit operates as follows. Capacitor C1 is charged using the 9 kW capacitor charger CCR50KV-4J (V_{source}). When S1 is triggered, the stored energy in C1 undergoes discharge through the primary winding w_1 of the SPT and resonantly charges C2. The charging current of C2 flows through the SOS, providing the forward pumping current. The transformer is designed to saturate at the maximum voltage on C2, when the forward current through the SOS diode is zero. At this time, the forward pumping stage is over.

Capacitor C2 then discharges through the SPT secondary winding w_2 and SOS diode, storing energy in inductive storage, which consists of the saturated inductance of the secondary winding and the parasitic inductance of the circuit. During this process, the reverse pumping of the SOS diode takes place. Subsequently, the diode cuts off the reverse current – ideally at its maximum – when all energy has been transferred to the inductive storage. The current is therefore transmitted to the load, resulting in a nanosecond high-voltage pulse with an amplitude V_{R_L} highly dependent on the load.

4.2.2.2 Description of the main components

Capacitors and primary switch

Ceramic high-voltage capacitors TDK UHV-9A (2 nF, 40 kV) are used to assemble C1 (50 in parallel) and C2 (10 in series, 3 in parallel). Their capacitances (C1 = 100 nF and C2 = 620 pF) are matched according to the SPT transformation ratio to maximize the energy transfer efficiency (w_1 = 1 turn and w_2 = 12 turns).

In addition to C1 voltage, the amplitude and dI/dt of the current flowing through the SPT primary winding are essential parameters in the design of the primary switch S1. These current parameters result from a typical SOS forward pumping time of 500 ns. The inductance of the primary side can be calculated as 0.5 µH by applying the Thomson formula expressing the period T of an oscillating LC circuit:

$$T = 2\pi\sqrt{LC} \tag{4.1}$$

where L is the inductance of the circuit and C is the capacitance. The inductance calculation allows estimating the current amplitude (8 kA) and dI/dt (50 kA/µs) that must be handled by the primary switch when C1 is charged to 25 kV. The precise calculation of the inductance is given in Section 4.2.3.

The CX1174 thyratron, rated for 40 kV and 40 kA, meets the requirements of the S1 primary switch. It features two grids that are triggered by a double voltage pulse, to optimize triggering characteristics and switching performance as recommended in [2]. The triggering pulses, along with the reservoir and cathode heating currents, are supplied by an in-house assembled driving system. This system primarily relies on a standard North Star TT-G1/G2 driver [1], which generates the double trigger pulse. The driving system also includes two power supplies providing the heating currents, which are monitored by Hall effect current sensors. The thyratron driver is controlled by an Atmega328p microcontroller-based system (Arduino Uno R3), which communicates with the peripherals via a fiber-optic interface.

Saturable pulse transformer

Considering an optimal overvoltage coefficient of the opening switch of about 2 [18], the maximum voltage on C2 is assumed to be 250 kV to reach a load voltage of 500 kV. With a primary voltage V_{C1} of 25 kV, a transformation ratio n of 12 is determined with some margins, taking into account losses in the primary switch and SPT. The primary winding consists of a single turn to minimize its inductance and energy transfer time. The secondary winding is divided into two parallel sections of 12 turns each, in order to reduce its inductance, mostly in the saturated state. More details on the SPT design technique can be found in [25].

The cross-sectional area of the SPT magnetic core is derived from the voltage-time product [26]:

$$2\Delta B \times S_C \times N = V_{max} \times T_{sat} \tag{4.2}$$

where ΔB is the magnetic induction swing, S_c is the effective material cross-section, N is the number of turns of the secondary winding, V_{max} is the peak voltage across C2, and T_{sat} is the saturation time, which corresponds to the forward pumping duration of about 500 ns. Using the Finemet FT-3L nanocrystalline material of saturation induction Bs = 1.2 T, the required S_c is found to be approximately 22 cm^2. The geometric cross-section of 30 cm^2 is determined, considering the packing factor k = 0.73 due to interlaminar insulation of the tape wound core. Four toroidal cores of 256 x 165.2 x 25 mm^3 (OD x ID x h) have been used instead of a bulky single core, to improve cooling.

The winding supports and insulating spacers are 3D printed using liquid resin. The SPT is designed to operate in transformer oil. Taking into account the volume dielectric strength of 36 kV/mm of the transformer oil (Diala S4), the minimum distance between the winding and the core was chosen to be 13 mm in all directions, ensuring a safety margin of three times. The spacers of 4 mm thickness between two consecutive cores allow better cooling of the cores by oil circulation.

The SPT with its primary, secondary, and bias windings is depicted in Figure 4.10. The primary winding consists of an aluminum rod of 40 mm diameter and 180 mm height. The secondary winding is made of a 10 mm width braiding cable housed in dedicated notches to ensure insulation between turns. Additional grooves on the winding support increase the electrical path between two consecutive turns. The magnetic bias winding of 5 turns is used to reset the core before each pulse.

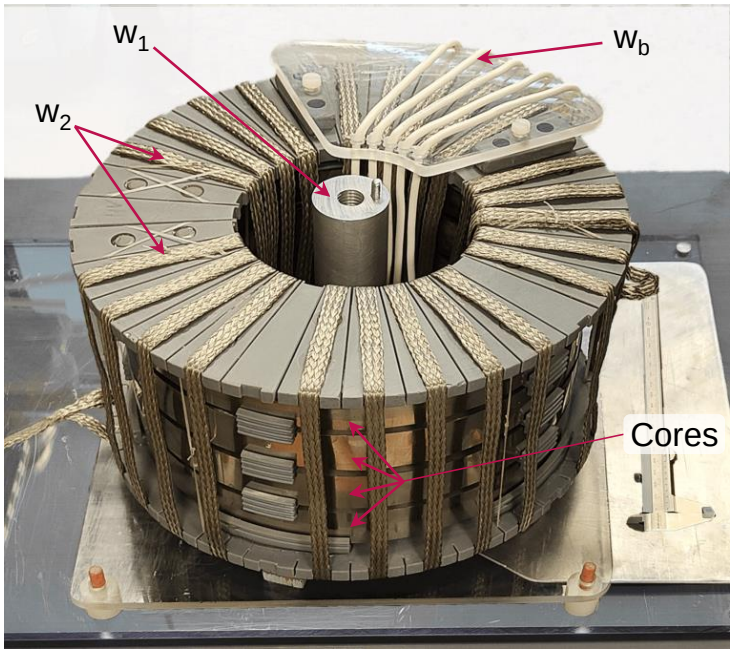

Figure 4.10: Picture of the SPT showing the four nanocrystalline cores with primary, secondary, and bias windings.

Opening switch

Two opening switches have been investigated in the framework of this research: (i) the SOS-180-4 (265 kV max) diode which serves as a reference and (ii) the OTS-150 (150 kV max) diode which is assembled from off-the-shelf rectifier diodes used in [22]. Figure 4.11 shows the assembled diodes, and their typical parameters are listed in Table 4.1.

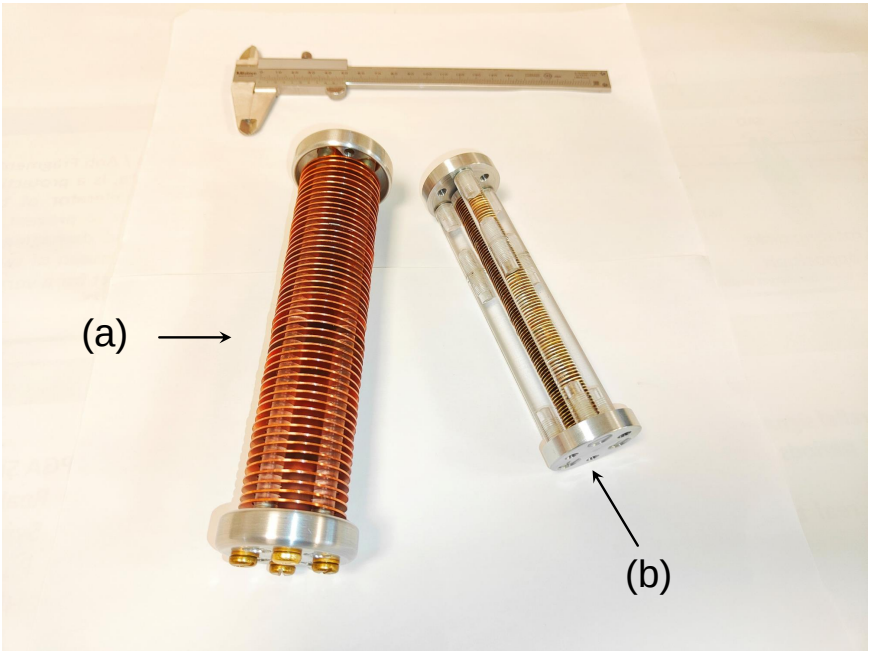

Figure 4.11: Picture of the opening switches showing (a) an SOS-180-4 (265 kV max) and (b) an OTS-150 (150 kV max).

Table 4.1: Parameters of the GO-SSOS circuit components

Component	**Type**	**Parameters**
Capacitor C1	TDK-UHV-9A	*100 nF, 40 kV*
Capacitor C2		*620 pF, 400 kV*
Switch S1	Thyratron CX1174	*40 kV, 40 kA, 150 kA/µs*
Transformer SPT	Finemet FT-3L	$n = 12$, $Bs = 1.2$ *T*, $S_c = 32$ cm^2
Opening switch SOS	SOS-180-4	*265 kV max, 4 kA reverse current*
	OTS-150	*150 kV max*
Load R_L	TVO	*From 50 Ω to 1 kΩ*

Diagnostics

A Pearson current monitor Model 101 (CM1) is used to measure the current through the primary switch S1 (Figure 4.9). Two in-house made current shunts R_{Sh1} = 0.15 Ω and R_{Sh2} = 0.5 Ω are connected in series to the SOS and the load, respectively, to measure their current independently. The North Star PVM100 and the homemade 600 kV Capacitive Divider (CD) described in [27] are employed to validate the load voltage obtained while using R_{Sh2}. The CD features an equivalent capacitance of 12.4 pF, an attenuation of -82 dB, and a bandwidth ranging from 8 Hz to 55 MHz. The primary voltage on C1 is measured using a North Star PVM12 probe. The voltage and current signals are captured using the real-time digital oscilloscopes: Tektronix TDS7704B (7 GHz, 20 Gs/s) and MSO56 (2 GHz, 6.25 Gs/s). The signals are attenuated using 4 GHz RF-LAMBDA attenuators.

The experimental setup is depicted in Figure 4.12, providing an overview of the arrangement. All the components are inserted inside the tank of dimensions 104 x 71 x 55 cm^3 (length x width x height). The tank housing all the components is filled with 300 liters of Diala S4 transformer oil. The entire system has a total mass of less than 350 kg. For practical reasons, this prototype intentionally features a large volume of the tank. Therefore, the size and weight can be decreased for an industrial system. The parameters of the main components are described in Table 4.1.

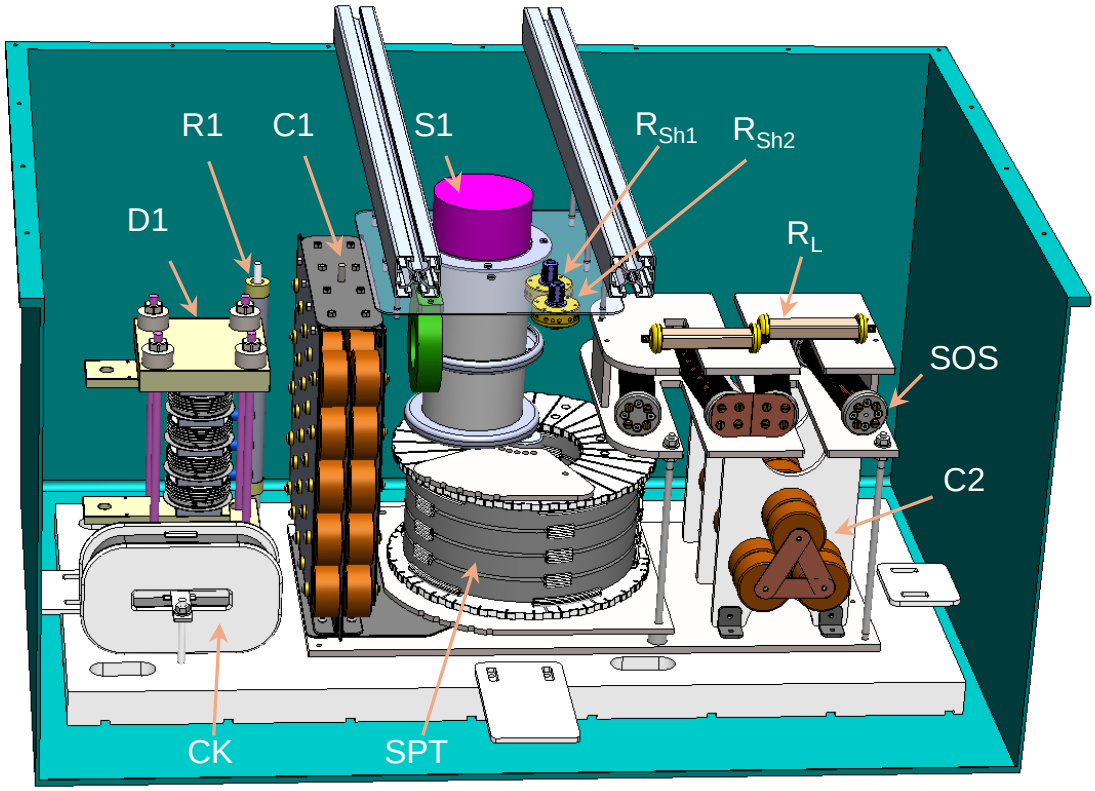

Figure 4.12: Overview of the high-voltage part of the experimental arrangement.

4.2.3 Results and discussion

4.2.3.1 Transformer characterization

To characterize the SPT, a short circuit experiment is performed. In this experiment, the secondary winding is connected in series with C2 and R_{Sh1}. The current through the SPT secondary winding and voltage across C2 is presented in Figure 4.13 when C1 is charged to 10 kV. From these waveforms, it can be seen that the core saturation occurs when C2 voltage reaches its maximum, thanks to the magnetic field applied by the bias circuit (Figure 4.9). The saturation time T_{sat} of about 512 ns is measured at the point where the slope of the current curve changes (Figure 4.13).

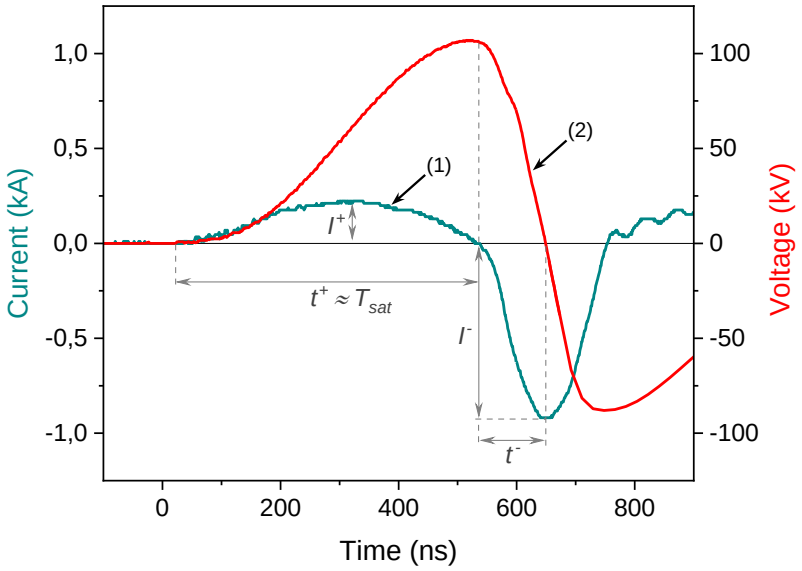

Figure 4.13: Waveforms of the current through the secondary winding (1), and the voltage across C2 (2), during the short circuit experiment when C1 is charged to 10 kV (E_{C1} = 5 J).

The short circuit experiment can be used to determine the actual inductance of the circuit, which is defined by the transformer winding, circuit components, and connections. Using Equation 4.3, these inductances are found to be approximately 0.53 µH and 88 µH for the primary and secondary sides, respectively.

$$L_w = \frac{(T_{sat})^2}{\pi^2 \times C_{eq}} \tag{4.3}$$

where C_{eq} represents the capacitance of the equivalent circuit referring to the primary ($C_{eq} \approx \frac{C1}{2}$) or secondary ($C_{eq} \approx \frac{C2}{2}$) side.

The secondary winding inductance drops to 7 µH when the pulse transformer saturates. Moreover, the saturated transformer decouples the primary and secondary circuits, and, as a result, C_{eq} is equal to C2. Consequently, the amplitude and duration of the reverse current are respectively 4.2 times higher and 2.4 times shorter than the forward current parameters (Figure 4.13).

4.2.3.2 Comparison of SOS and OTS

The investigation of the diodes was performed using the circuit presented in Figure 4.9. In the low-resistance load experiment, C1 was charged to 25 kV, which corresponds to 31.3 J stored in the primary energy storage. The resistive load was measured to be 49 Ω. The opening switches consisted of a single OTS-150 and a single SOS diode stack. The number of diodes in the SOS stack was arranged in order to have the same blocking voltage of about 150 kV in this experiment. The two diodes were tested in almost identical conditions provided by the circuit when the energy is transferred from C1 to C2.

The obtained results are presented in Figure 4.14. In both cases, the charging voltage of C2 is 242 kV. This voltage is determined through the integration of the discharge current of C2 ($I_{C2} = I_{R_{Sh1}} + I_{R_{Sh2}}$). For both diodes, the forward pumping current amplitude I^+ and duration t^+ are about 500 A and 440 ns, respectively. The on-state resistances of the diodes, calculated at the maximum amplitude I^+, are comparable, i.e. 1.2 Ω for the SOS diodes versus 2.8 Ω for the OTS-150.

Despite having similar forward pumping conditions, the two diodes react differently to the reverse current. Whereas the SOS diode allows the reverse current to flow up to its maximum of 2.2 kA, the OTS diode interrupts it earlier, when the reverse current reaches 0.9 kA. With the SOS diode, the voltage pulse across the load comes mainly from the inductive energy storage, since the current is interrupted close to its peak at the reverse pumping time t^- of 71 ns. At this moment, about 93% of the energy stored in C2 ($E_{C2} = 18.2\ J$) is transferred to the intermediate inductive storage L_w of 7 µH. Conversely, the early interruption of the current by the OTS leads to hybrid energy storage, since the energy stored in the capacitor C2 is not fully transferred into inductive storage. Indeed, at the moment of current interruption by the OTS-150, only 16% of the capacitive energy has been transferred to the inductance. This early interruption of the current by the OTS diodes was first observed in [22] where the OTS diode was pumped in similar conditions in a 10 J test bench. Even though the OTS diodes' typical recovery time falls within the range of 0.6 µs to 0.9 µs, according to the data sheet, their operation in the test bench exhibits nanosecond reverse current conduction times as short as 26 ns, when the forward current duration is about 440 ns. This short reverse conduction of the OTS diode may be attributed to the lifetime controlling processes of carriers in silicon power devices, involving methods such as diffusion of impurities like gold and platinum, or the creation of traps in the silicon lattice by high-energy particles [28]. However, since the structure and doping profile of the diodes are not disclosed, further research is required for a thorough understanding of their switching mechanism.

After the OTS diode has interrupted the current, the residual energy in capacitor C2 simply discharges into the load. The RC time constant calculated for the 49 Ω load corresponds to 31 ns. The combination of the inductive and capacitive energy discharges in the load forms the output pulse using the OTS diode. The main parameters of current and voltage amplitudes and durations are summarized in Table 4.2.

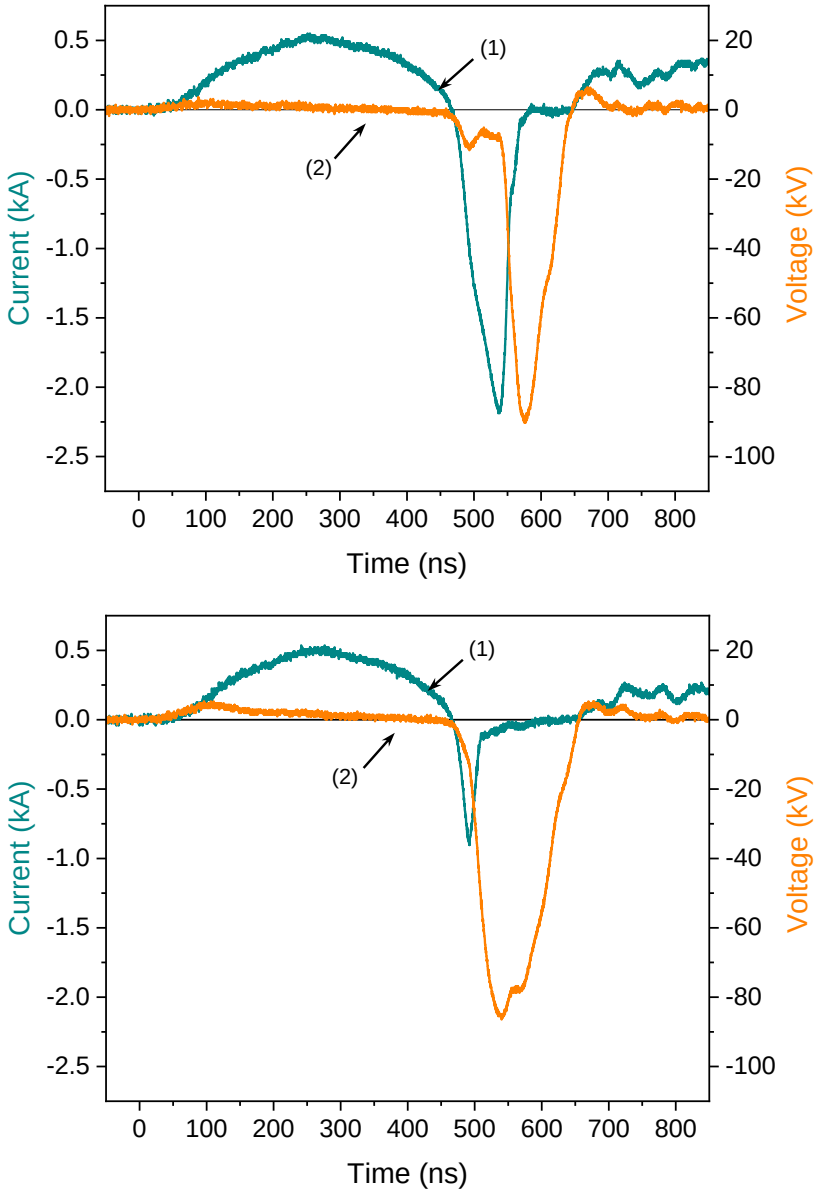

Figure 4.14: Waveforms of the current through the diode (1) and voltage at the 49 Ω load (2) for (a) SOS diode stack (150 kV max) and (b) OTS-150 (150 kV max), with a primary energy E_{C1} of 31.3 J.

Table 4.2: Diode current and load voltage parameters at 50 Ω

	DBV* *(kV)*	I^+ *(kA)*	I^- *(kA)*	t^+ *(ns)*	t^- *(ns)*	V_{R_L} *(kV)*	t_r *(ns)*	FWHM *(ns)*
SOS	150	0.52	2.2	440	71	90	26	63
OTS	150	0.49	0.9	440	26	85	38	105

* Diode Blocking Voltage (DBV).

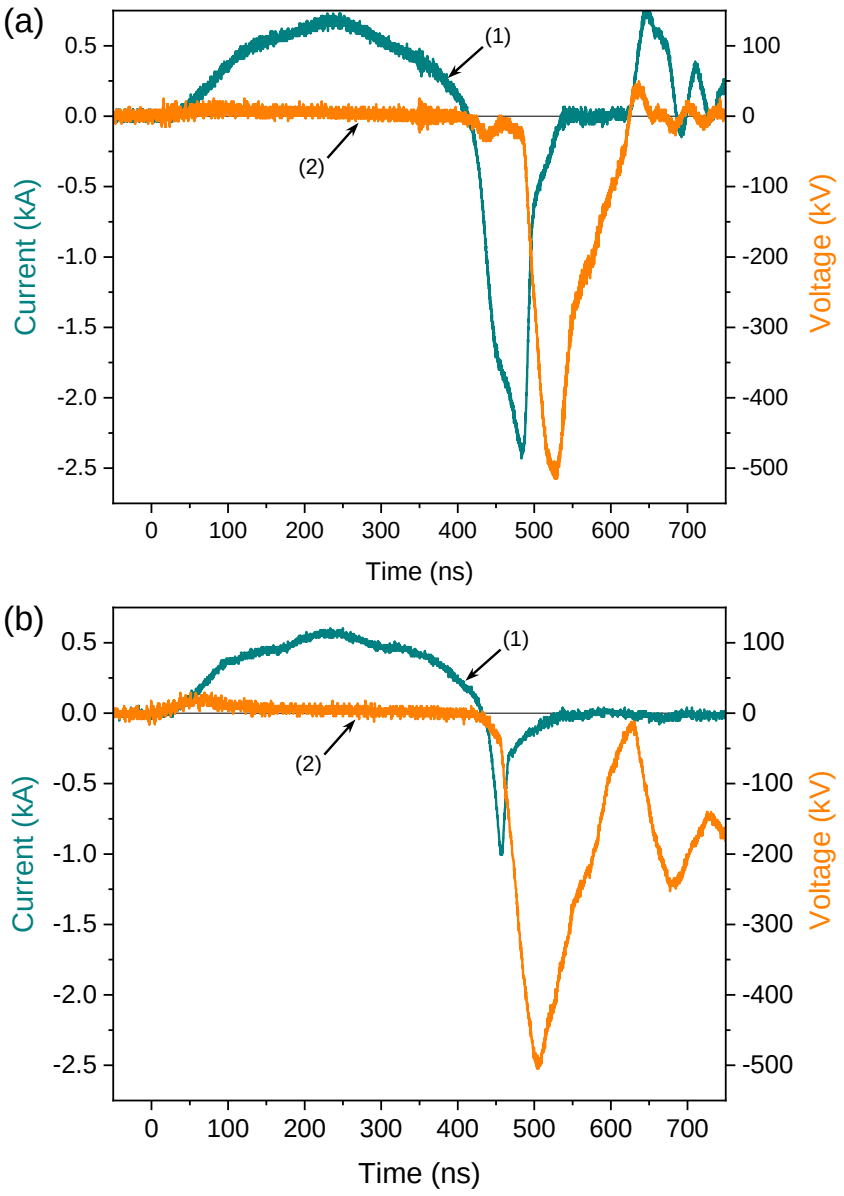

Figure 4.15: Waveforms of the current through the diode (1) and voltage across the load (2) for (a) two SOS-180-4 in series (530 kV max) with R_L = 960 Ω, and (b) four OTS-150 in series (600 kV max) with R_L = 940 Ω, at a primary energy E_{C1} = 36.5 J.

Table 4.3: Diode current and load voltage parameters at 1 kΩ

	DBV (*kV*)	I^+ (*kA*)	I^- (*kA*)	t^+ (*ns*)	t^- (*ns*)	V_{R_L} (*kV*)	t_r (*ns*)	FWHM (*ns*)
SOS	530	0.7	2.4	400	70	509	26	60
OTS	600	0.6	1	425	25	498	38	84

In the high-resistance load experiment, the primary energy stored was increased to 36.5 J, and the load of about 1 kΩ was installed to reach voltages of up to 500 kV. As a single SOS-180-4 diode had proven its ability to withstand pulse voltages of amplitude up to 265 kV in a previous study, the SOS diode assembly consisted of two SOS-180-4 connected in series, while the OTS was assembled using four OTS-150 diodes.

The results are presented in Figure 4.15 and Table 4.3. In this configuration, the inductive energy amounts to 90% with the SOS diode and to 16% with the OTS diode, out of the total energy of 22 J stored in C2. The peak cut-off current I^{-} is 2.4 kA for the SOS diode and the current through the 960 Ω load is 530 A. For the OTS, these parameters are respectively 1 kA and 530 A when the load is 940 Ω. Thus, the targeted output voltage of 500 kV was successfully reached using both opening switches, even though with the OTS diode, the circuit does not operate as an ideal inductive storage system.

Unlike the operation with a low resistive load, at a high load, the voltage pulse obtained with the OTS diode breaks down into a main pulse [from 430 ns to 630 ns in Figure 4.15 (b)] followed by oscillations whose intensity decreases with time. In our opinion, this is due to the oscillation of the residual energy in C2 after the diode interrupts the current, because of the parasitic capacitance which is estimated to be about 50 pF through SPICE simulation. However, the energy of the main pulse obtained with the OTS diode (16 J) is greater than that with the SOS diode (12 J). The reason is likely the lower switching losses of the OTS diodes since the reverse current is interrupted earlier.

As mentioned in Section 4.2.2, additional capacitive probes (PVM100 and CD) are employed to confirm the accuracy of the voltage measurement method using the R_{Sh2} current viewing resistor and the load value. Figure 4.16 (a) shows the voltage pulse measured using the three probes. This comparison at the same time serves for the calibration of the CD using the PVM100 probe, which is rated for a maximum of 150 kV. For higher voltages, the measurement is performed using CD and R_{Sh2} [Figure. 4.16 (b)]. Notably, the voltage amplitude deviation of less than 10% and the time difference of less than 1% confirm the accuracy of the R_{Sh2} measurement.

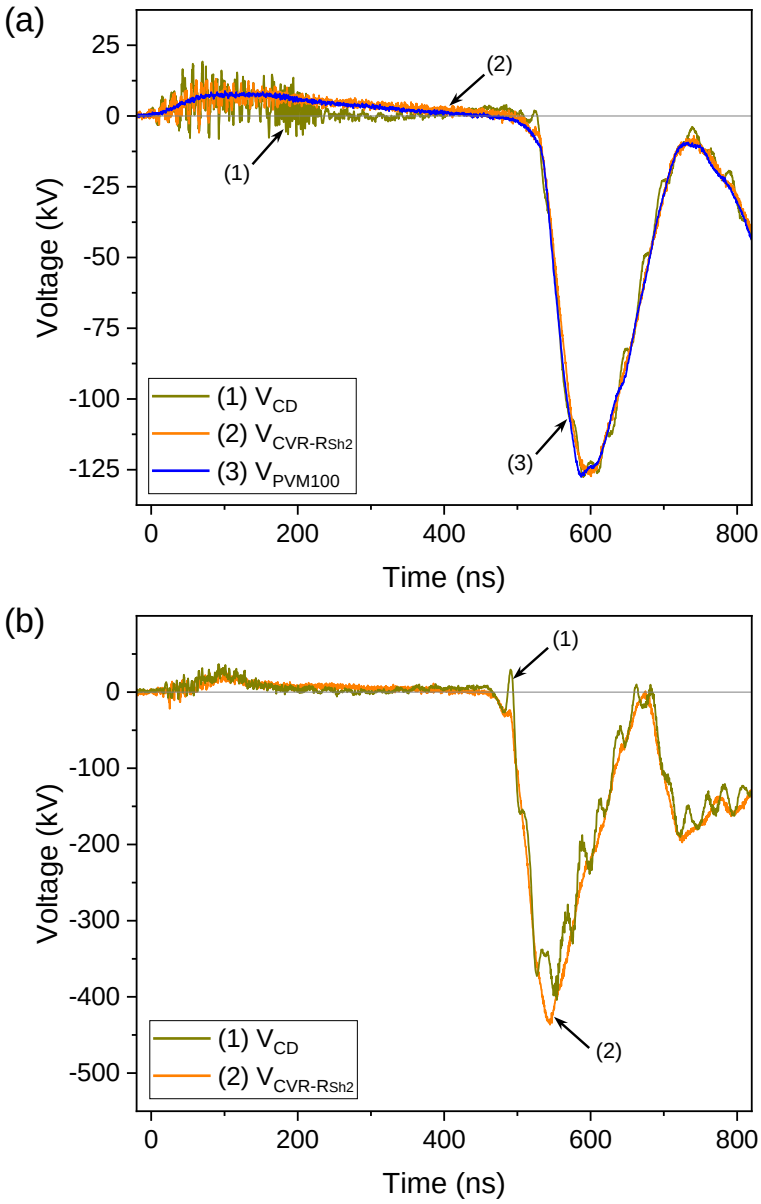

Figure 4.16: Load voltage waveforms obtained at 1 kΩ load, using the capacitive divider CD (1), the current viewing resistor R_{Sh2} (2), and the PVM100 probe (3) for (a) low voltage (E_{C1} = 4 J) and (b) high voltage (E_{C1} = 31.3 J).

4.2.3.3 500 kV generator based on OTS diode

The capability of the OTS diode to generate high-voltage pulses is harnessed in this part of the study. Based on the preceding test bench, the 500 kV generator prototype featuring an OTS switch (GO-SSOS), with a stored energy of up to 40 J, is proposed. In this generator, the OTS diode consists of four OTS-150 connected in series, and the whole stack fits into a volume inferior to 2 liters.

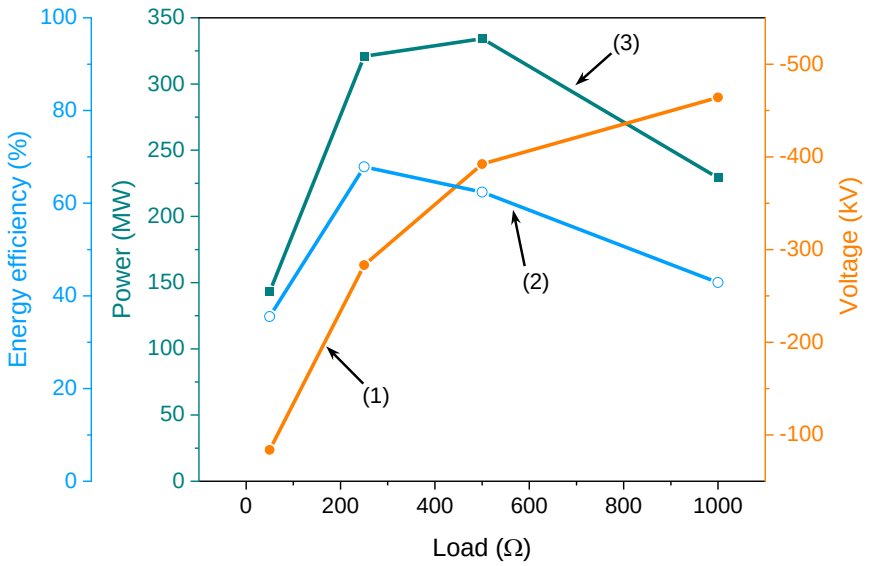

Figure 4.17: Load characteristics of the GO-SSOS showing the load voltage V_{R_L} (1), the overall energy efficiency (2), and the load power (3), for different resistive loads ranging from 50 Ω to 1 kΩ (E_{C1} = 31.3 J).

Figure 4.17 presents the load characteristic of the GO-SSOS on a resistive load varying from 50 Ω to 1 kΩ. Throughout this range, the stored energy remains fixed at 31 J. In this configuration, the system reaches a peak power of 335 MW, when the load was 500 Ω.

The overall energy efficiency (E_{R_L}/E_{C1}) depending on the load is between 36% and 68%. It is important to note that the output energy only reflects the energy concentrated in the effective main pulse. In addition, the highest voltage of 465 kV is obtained across the load of about 1 kΩ.

The maximum generator output voltage amplitude of 515 kV is obtained in single pulse mode when the primary energy was increased to 39.2 J and the load fixed at 940 Ω. The rise time and FWHM of the pulse are 37 ns and 83 ns respectively.

The operation of the GO-SSOS at its maximum PRF of 60 Hz is presented in Figure 4.18. A train of ten pulses with 500 kV amplitude at 60 Hz is shown in Figure 4.18 (a). At this frequency, three sets of ten pulses are acquired in burst mode. The overlay of this burst is plotted in Figure 4.18 (b) showing the excellent reproducibility of the pulses. The overall pulse-to-pulse amplitude and duration deviations are less than 2% and 10%, respectively.

It should be considered that two main components limit the PRF of the generator. The first is the capacitive charger, which requires about 15 ms to charge C1 to its maximum voltage of 28 kV. The second is the CX1174 thyratron, which, according to its datasheet, is capable of operating at a maximum PRF of 60 Hz when the current is 8 kA. Nevertheless, in the described experiment when the GO-SSOS operates at 60 Hz, the primary current is approximately 10 kA, which may reduce the thyratron lifetime.

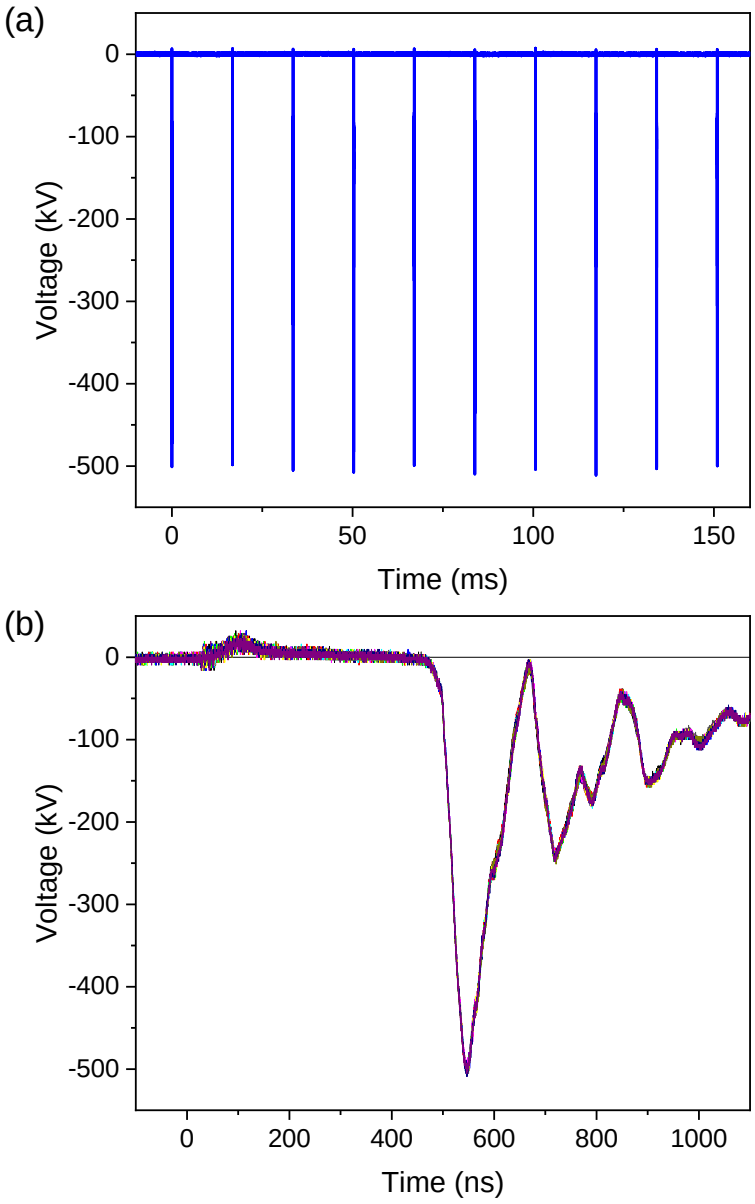

Figure 4.18: Waveforms of the voltage across the load during operation of the GO-SSOS at 60 Hz (E_{C1} = 39.2 J, R_L = 940 Ω): (a) a train of 10 pulses, and (b) overlay of 30 pulses, acquired in the Peak Detection and Fast Frame modes of the oscilloscope.

The use of the GO-SSOS for a common pulsed power application, such as corona discharge, has been explored in this study. For this experiment, a high-voltage cable was connected to the output of the generator inside the oil tank. The other end of the cable was extended outside the oil and terminated in a high-voltage electrode positioned approximately 15 cm from a ground electrode. A needle-needle electrode configuration was adopted for this experiment. With a primary energy of 31.3 J and a PRF of 50 Hz, the corona discharge generated within the 5-second burst is shown in Figure 4.19. The experiments have successfully demonstrated the robustness of the generator control system against strong electromagnetic interference.

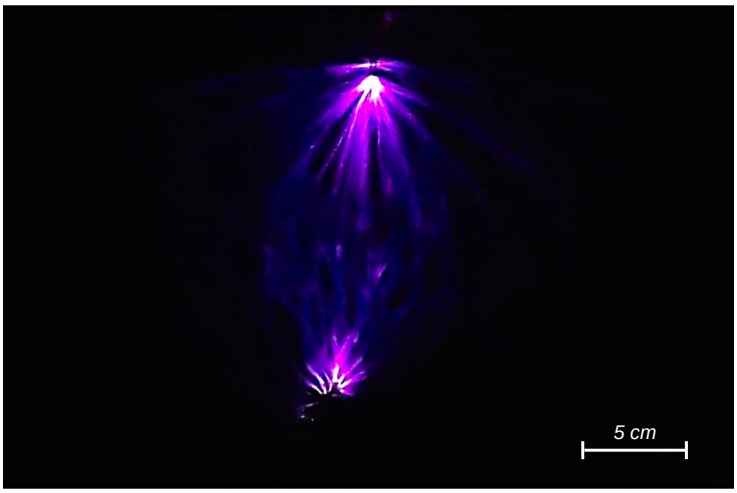

Figure 4.19: Photograph of corona discharge generated by the 500 kV GO-SSOS (E_{C1} = 31.3 J). The picture was taken using a regular mobile phone camera.

4.2.4 Conclusion

This study introduces a nanosecond pulsed power generator based on an OTS solid-state opening switch for pulsed power applications. Despite the short reverse conduction time of the OTS diodes, their ability to produce high-voltage pulses was demonstrated. A voltage pulse having an amplitude of up to 515 kV with a rise time of 35 ns and an FWHM of 80 ns was obtained across a 1 kΩ load. In addition, the operation of the generator at a PRF of up to 60 Hz with high reproducibility of the pulses was shown. The PRF is limited by the primary thyratron switch and the high-voltage capacitor charger. Furthermore, an application of corona discharge was explored in the burst mode at a PRF of 50 Hz and a burst duration of 5 seconds. During testing, no degradation of OTS diodes performance was observed after thousands of generated pulses. Thus, the reliability of the OTS-based pulsed power system has been confirmed. However, there is room for improvement in several parameters of this nanosecond high-voltage generator prototype, including volume reduction to achieve a more compact design and also the use of a solid-state primary switch to increase the frequency range. Pulse shaping and forming can also be considered. Further investigation of the OTS diode's current interruption mechanism is needed to get insights for future optimizations.

This conclusion marks the end of Chapter 4 and the work carried out on the GO-SSOS. A conclusion of the entire work and future prospects are detailed in the next "Conclusion and perspectives" part.

4.3 References

[1] North Star High Voltage, "Thyratron Driver Manual and Application Note," North Star High Voltage, Tech. Rep., 2008. [Online]. Available: https://www.highvoltageprobes.com/wp-content/uploads/2019/11/ThyrDriveManual082908.pdf (visited on 04/25/2023).

[2] e2v Teledyne, *CX1174 Deuterium-Filled Ceramic Thyratron*. [Online]. Available: https://www.teledyne-e2v.com/en-us/Solutions_/Documents/datasheets/Thyratron/cx1174.pdf (visited on 09/25/2023).

[3] J. Lehr and P. Ron, *Foundations of Pulsed Power Technology*. 2017, ISBN: 9781118628393. DOI: 10.1002/9781118886502.

[4] S. Ziegler, R. C. Woodward, H. H. C. Iu, and L. J. Borle, "Current sensing techniques: A review," *IEEE Sensors Journal*, vol. 9, no. 4, pp. 354–376, 2009, ISSN: 1530437X. DOI: 10.1109/JSEN.2009.2013914.

[5] A. V. Ponomarev, Y. I. Mamontov, A. I. Gusev, and M. S. Pedos, "Novel control system of the high-voltage IGBT-switch," *Journal of Physics: Conference Series*, vol. 830, p. 012 006, May 2017, ISSN: 1742-6588. DOI: 10.1088/1742-6596/830/1/012006. [Online]. Available: https://iopscience.iop.org/article/10.1088/1742-6596/830/1/012006.

[6] L. Pecastaing, "Conception et réalisation d' un système de génération d' impulsions haute tension ultra brèves Application aux radars larges bandes," Ph.D. dissertation, Université de Pau et des Pays de l'Adour, 2001. [Online]. Available: https://theses.hal.science/tel-00010696.

[7] N. Ibrahimi, "Subnanosecond pulsed power technology for biomedical and military applications," Génie Électrique, Université de Pau et des Pays de l'Adour., Ph.D. dissertation, 2022.

[8] M. Kristiansen, "Pulsed power applications," in *Ninth IEEE International Pulsed Power Conference*, IEEE, 1993, p. 6, ISBN: 0-7803-1415-8. DOI: 10.1109/PPC.1993.512864.

[9] K. Takaki, I. Yagi, S. Mukaigawa, T. Fujiwara, and T. Go, "Ozone synthesis using streamer discharge produced by nanoseconds pulse voltage under atmospheric pressure," *PPC2009 - 17th IEEE International Pulsed Power Conference*, no. December 2015, pp. 989–993, 2009. DOI: 10.1109/PPC.2009.5386169.

[10] A. I. Gusev, S. K. Lyubutin, V. Patrakov, *et al.*, "GTO Like Thyristors Triggered in Impact-Ionization Wave Mode," in *2019 IEEE Pulsed Power & Plasma Science (PPPS)*, vol. 2019-June, IEEE, Jun. 2019, pp. 1–4, ISBN: 978-1-5386-7969-2. DOI: 10.1109/PPPS34859.2019.9009695.

[11] S. Y. Sokovnin and M. E. Balezin, "Surface irradiation installation for eggs based on URT-0,5M accelerator," *Radiation Physics and Chemistry*, vol. 196, p. 110 137, Apr. 2022, ISSN: 0969806X. DOI: 10.1016/j.radphyschem.2022.110137.

[12] R. A. Vazirov, S. Y. Sokovnin, A. S. Krivonogova, and A. G. Isaeva, "Radiation surface antimicrobial processing of poultry meat and by-products using the nanosecond low-energy electron beam," *Radiation Physics and Chemistry*, vol. 217, p. 111 528, Apr. 2024, ISSN: 0969-806X. DOI: 10.1016/j.radphyschem.2024.111528.

[13] N. Ibrahimi, L. Vallet, F. M. Andre, *et al.*, "A Subnanosecond Pulsed Electric Field System for Studying Cells Electropermeabilization," *IEEE Transactions on Plasma Science*, vol. 48, no. 12, pp. 4242–4249, 2020, ISSN: 19399375. DOI: 10.1109/TPS.2020.3034286.

[14] C. Da Silva, C. Lamarche, C. Pichereaux, *et al.*, "Bacterial eradication by a low-energy pulsed electron beam generator," *Bioelectrochemistry*, vol. 156, no. October 2023, 2024, ISSN: 1878562X. DOI: 10.1016/j.bioelechem.2023.108593.

[15] Y. A. Kotov, G. A. Mesyats, S. N. Rukin, *et al.*, "Megavolt nanosecond 50 kW average power all solid state driver for commercial applications," *Digest of Technical Papers-IEEE International Pulsed Power Conference*, vol. 2, pp. 1227–1230, 1995. DOI: 10.1109/ppc.1995.599782.

[16] J. Gao, S. Li, B. Qian, J. Zhang, J. Zhang, and H. Yang, "Development of a GW-Level solid-state long pulse generator," *IEEE Transactions on Plasma Science*, vol. 47, no. 10, pp. 4512–4517, 2019, ISSN: 19399375. DOI: 10.1109/TPS.2019.2927609.

[17] S. Li, J. Gao, C. Shi, X. Liu, and H. Yang, "Investigation on a fast rise time high voltage pulse transformer," *Review of Scientific Instruments*, vol. 90, no. 12, 2019, ISSN: 10897623. DOI: 10.1063/1.5124981.

[18] S. N. Rukin, "Pulsed power technology based on semiconductor opening switches: A review," *Review of Scientific Instruments*, vol. 91, no. 1, p. 011 501, Jan. 2020, ISSN: 0034-6748. DOI: 10.1063/1.5128297.

[19] G. A. Mesyats, *Pulsed Power*. Boston, MA: Springer US, 2005, ISBN: 978-0-306-48653-1. DOI: 10.1007/b116932.

[20] S. A. Darznek, S. N. Rukin, and S. N. Tsiranov, "Effect of structure doping profile on the current switching-off process in power semiconductor opening switches," *Technical Physics*, vol. 45, no. 4, pp. 436–442, 2000, ISSN: 10637842. DOI: 10.1134/1.1259650.

[21] S. N. Rukin, A. I. Gusev, S. Lyubutin, B. Slovikovsky, and S. Tsyranov, "Operation of a semiconductor opening switch at ultrahigh current density," *Russian Physics Journal*, no. 12, pp. 3–6, 2012.

[22] M. R. Degnon, A. I. Gusev, A. S. de Ferron, *et al.*, "Off-the-Shelf Diodes as High-Voltage Opening Switches," *IEEE Transactions on Plasma Science*, vol. 50, no. 10, pp. 3384–3392, Oct. 2022, ISSN: 0093-3813. DOI: 10.1109/TPS.2022.3177702.

[23] A. I. Gusev, S. K. Lyubutin, S. N. Rukin, B. G. Slovikovsky, and S. N. Tsyranov, "High-current pulse switching by thyristors triggered in the impact-ionization wave mode," *Instruments and Experimental Techniques*, vol. 60, no. 4, pp. 545–550, 2017, ISSN: 00204412. DOI: 10.1134/S0020441217030204.

[24] J. Waldron, K. Brandmier, and V. Temple, "Ultra-fast, high reliability solid state thyratron, ignitron and thyristor replacement," *Digest of Technical Papers-IEEE International Pulsed Power Conference*, vol. 2015-Octob, pp. 676–680, 2015. DOI: 10.1109/PPC.2015.7296986.

[25] M. R. Degnon, A. I. Gusev, A. S. de Ferron, *et al.*, "A Saturable Pulse Transformer Based on Nanocrystalline Magnetic Cores for an Adjustable Nanosecond High-Voltage Generator," *IEEE Transactions on Plasma Science*, pp. 1–9, 2023, ISSN: 19399375. DOI: 10.1109/TPS.2023.3284657.

[26] J. Choi, "Introduction of the Magnetic Pulse Compressor (MPC) - Fundamental Review and Practical Application," *Journal of Electrical Engineering and Technology*, vol. 5, no. 3, pp. 484–492, Sep. 2010, ISSN: 1975-0102. DOI: 10.5370/JEET.2010.5.3.484.

[27] R. Pecquois, L. Pecastaing, A. De Ferron, *et al.*, "Simple and compact capacitive voltage probe for measuring voltage impulses up to 0.5 MV," *Review of Scientific Instruments*, vol. 83, no. 3, 2012, ISSN: 00346748. DOI: 10.1063/1.3690906.

[28] J. Lutz, H. Schlangenotto, U. Scheuermann, and R. De Doncker, *Semiconductor Power Devices*. Berlin, Heidelberg: Springer Berlin Heidelberg, 2011, ISBN: 978-3-642-11124-2. DOI: 10.1007/978-3-642-11125-9.

Conclusion and perspectives

Conclusion and perspectives

Conclusion

The research carried out within this thesis aimed to investigate OTS diodes as opening switches in pulsed power systems. The interest in opening switches is justified by the advantages of IES with higher energy density compared to CES. Yet, only a few solid-state opening switches can efficiently handle nanosecond high-power pulses. SOS diodes take a leading position among them due to their exceptional combination of characteristics. However, since SOS diodes are not available in the market, this work comes up with alternative OTS solutions to generate nanosecond high-voltage pulses of up to 500 kV amplitude.

The work was divided into three main parts. The first part involved the examination of OTS diodes on low- and medium-energy test benches of 25 mJ and 10 J, respectively. In this context, more than twenty-five different types of diodes, including rectifiers, avalanche, fast recovery, and TVS diodes, were studied in the SOS mode on the low-energy test bench. Voltage pulses with an amplitude of 1.8–2.5 kV and a rise time of 13–27 ns are obtained on a 30 Ω resistive load. The TVS diodes emerged as particularly promising opening switches, demonstrating optimal switching-time performance. A set of 64 TVS diodes (8 in series and 8 in parallel) successfully produces a voltage pulse with an amplitude of 3 kV and a rise time of 10 ns on a 100 Ω load. The ability of TVS diodes to operate as a high-voltage nanosecond opening switch has been demonstrated, probably for the first time. OTS rectifier diodes also exhibited promising results when switching reverse currents of hundreds of amperes on the 10 J test bench. A notable outcome obtained using the OTS-100 is the generation of an output voltage approaching 90 kV across the load of 1 kΩ with a rise time of 20 ns.

The second part of the work involved experiments on the 10 J energy test bench, focusing on studies related to nanocrystalline magnetic cores. These experiments highlighted the role of the core material hysteresis in the operation of SPTs. Two SPTs, utilizing nanocrystalline amorphous material "Finemet" and characterized by flat and rectangular hysteresis loops, were examined. The distinctive advantages of these transformers were effectively exploited in the development of two SOS generators, one with an adjustable output voltage and the other with a fixed output setting. The generated output voltages are in the range of 10 kV to 200 kV, with a rise time of 16 ns when the load is 1 kΩ. Furthermore, the experiments on the magnetic cores reveal the high energy efficiency and switching performance of the Finemet over Vitroperm material when operating under fast pulse magnetization. The superior performance of the Finemet FT-3L core justifies its adoption for the 500 kV GO-SSOS design.

The third part was dedicated to the design and characterization of the 500 kV GO-SSOS based on an OTS opening switch. The experience gained during the development of the test benches of the preceding parts was essential in improving the design of the GO-SSOS. This generator has an initially stored energy of up to 40 J and also serves as a test bench for OTS-150 diode investigation. It comprises a 40 kV primary thyratron switch and a step-up SPT designed for 300 kV. The thyratron and the capacitor charger are the main components limiting the PRF of the GO-SSOS. The OTS opening switch consisted of a series-connected arrangement of rectifying diodes (OTS-150). The entire diode stack fits into a volume of less than 2 liters. The whole system is optically triggered using a homemade trigger generator enabling a remote control. A generated voltage of 515 kV was recorded with 37 ns rise time and 83 ns pulse width on a load of about 1 kΩ. Load voltage measurements are obtained using the designed CVR with a bandwidth reaching 700 MHz, and these measurements are confirmed using two independent probes (capacitive voltage dividers). The overall energy efficiency of the system is in the range of 35% to 70% depending on the load and the peak power obtained is greater than 300 MW. The excellent reproducibility of the output voltage at a PRF of 60 Hz is shown, and an application of corona discharge in air has been successfully demonstrated.

In a nutshell, the research findings reveal that with a refined selection of OTS diodes, an operation as an opening switch can successfully be achieved. Even though the performance of the OTS diodes is limited (lower reverse current and longer rise time) in comparison to SOS diodes, they exhibit good stability and reproducibility after thousands of pulses. Moreover, the OTS diodes offer ready-to-use solutions and can be upscaled for different power requirements. We believe that these results open the way for OTS diodes to be employed as high-energy opening switches suitable for pulsed power applications across diverse fields of modern physics and technology.

Perspectives

Several avenues can be explored to complete or improve this work. First, testing the GO-SSOS on a real load – an electron gun – could enable assessing its effectiveness in the application of e-beam sterilization. Since the generator output characteristics such as voltage/current amplitude are strongly dependent on the load, it is difficult to predict the shape and form of the output pulse without an exact load specification. A study of the generator's characteristics on the real load must therefore be carried out.

Second, the use of a more powerful charger is essential to increase the PRF. For instance, to operate the GO-SSOS at a PRF of 100 Hz, the required average power and voltage of the charger are about 4 kW and 30 kV, respectively. High PRF also means replacing the thyratron with a solid-state closing switch. At present, thyristors triggered in impact ionization mode and Solidtron switches appear to be the most suitable solutions for switching the high current and high dI/dt imposed by the circuit containing a single magnetic element.

In [1], nine series-connected thyristors, each with a blocking voltage of 2 kV, a peak surge current of 8 kA, and a critical dI/dt of 0.4 kA/µs (when triggered via the gate electrode), were successfully switched in the impact-ionization wave mode. A fast sub-nanosecond switching was observed, and the measured dI/dt of 134 kA/µs exceeded the data sheet specification by over three hundred times. Moreover, switching of thyristors connected in parallel and/or series in this mode has also been proven in [2], [3], offering the possibility of connecting multiple thyristors as necessary. The main constraint of the impact ionization approach is the high dV/dt of more than 1 kV/ns, which is required to trigger thyristors in this mode. A trigger generator providing this steep dV/dt is therefore needed.

On the other hand, Solidtron switches [4] with permissible dI/dt in excess of 100 kA/µs, are also a promising solution for the primary switch. However, the cost of this type of switch and the possibility of using it in commercial generators need to be carefully considered.

Should none of these options be suitable for the primary switch, an alternative possibility could be the adoption of a circuit with multiple MPCs, thus relieving the requirements of the primary switch, but at the expense of energy efficiency.

Numerical simulations could be conducted to optimize the design of the GO-SSOS. For instance, electrostatic simulation can assist in optimizing the SPT insulation and its winding configuration for improved performance, reliability, and safety. In addition, thermal constraints for continuous-frequency operation need to be studied.

Regarding the OTS diodes, a study of their switching mechanism should be undertaken since the physics of operation is unclear. However, this requires knowledge of the diode's structure and doping profile. These characteristics could be obtained using Nanometric scale Second Ion Mass Spectrometry (NanoSIMS) and Second Ion Mass Spectrometry (SIMS) analysis, which have been explored in this thesis to determine the doping profile of SOS diodes. The results are presented in the Appendix A.

Ultimately, domestic production of SOS diodes would improve their availability on the market and enable large-scale use of IES solid-state generators in pulsed power applications.

References

[1] A. I. Gusev, S. K. Lyubutin, S. N. Rukin, and S. N. Tsyranov, "Superfast Thyristor-Based Switches Operating in Impact-Ionization Wave Mode," *IEEE Transactions on Plasma Science*, vol. 44, no. 10, pp. 1888–1893, 2016, ISSN: 00933813. DOI: 10.1109/TPS.2016.2542343.

[2] E. Shahriari, T. Maysonnave, A. I. Gusev, A. S. de Ferron, L. Pecastaing, and B. M. Novac, "Impact-Ionization Switching of High-Voltage Thyristors Connected in Parallel," *IEEE Transactions on Plasma Science*, vol. 51, no. 10, pp. 2878–2884, Oct. 2023, ISSN: 0093-3813. DOI: 10.1109/TPS.2023.3275315.

[3] E. Shahriari, T. Maysonnave, A. I. Gusev, A. S. de Ferron, and L. Pecastaing, "Series–Parallel Connection of Thyristors Triggered in Impact-Ionization Wave Mode," *IEEE Transactions on Plasma Science*, vol. PP, pp. 1–8, 2024, ISSN: 0093-3813. DOI: 10.1109/TPS.2024.3377898.

[4] J. Waldron and K. Brandmier, "Second Generation High-Voltage, Ultra- Fast, High Reliability Solid State Thyratron Replacements," in *2017 IEEE International Conference on Plasma Science (ICOPS)*, ICOPS, Atlantic City, NJ, Atlantic City, NJ: IEEE, May 2017, pp. 1–1, ISBN: 978-1-5090-5243-1. DOI: 10.1109/PLASMA.2017.8496180. [Online]. Available: http://www.siliconpower.com/datasheets/Ultra-fastThyratronReplacement-JW063017.pdf.

Appendix A

Analysis of an SOS diode doping profile

Chapter A

Analysis of an SOS diode doping profile

Introduction

For many OTS diodes, the doping profile is not disclosed by the manufacturer, preventing the proper understanding of their switching mechanism, particularly in the SOS mode. In this work, a method of analyzing semiconductor doping profiles using NanoSIMS and SIMS imaging is explored. According to [1], this method can be used to determine dopant species and concentrations in Silicon. The analysis is carried out on SOS diode samples with a known doping profile, i.e., available in the literature, for reference and validation purposes. This report discusses the measurement and results of the doping profile obtained using SIMS methods.

A.1 Sample description

A.1.1 Structure and doping profile of SOS diodes

The manufacturing process of a high-voltage semiconductor diode with a $p^+ - p - n - n^+$ structure is described in [2]. A few steps of the process are outlined as follows. On an $n-$type Silicon substrate, a double diffusion of $p-$type dopants is realized on the anode side. An $n-$type diffusion is then conducted on the cathode side, forming the n^+ layer. The silicon structure is subsequently brazed to a molybdenum disc on the anode side using aluminum-based solder alloy. A beveling of the peripheral edge of the silicon structure is performed to limit electric field enhancement during the reverse blocking state. Finally, the device is encapsulated in its final package. The described structure is illustrated in Figure A.1.

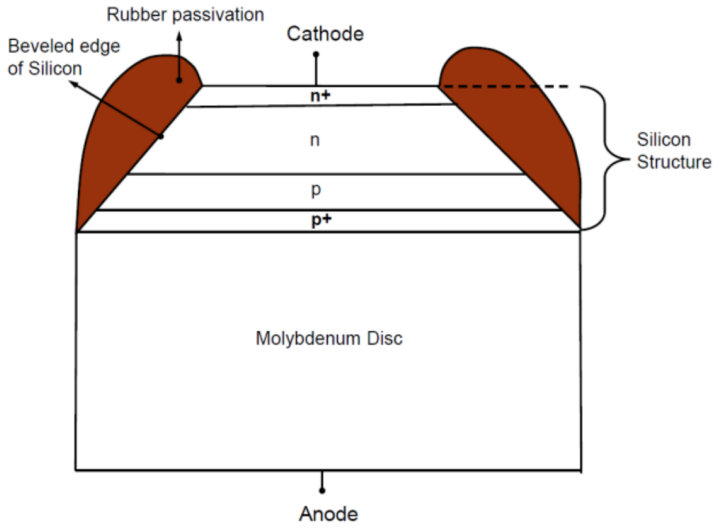

Figure A.1: Structure of a high-voltage diode [2].

The SOS diodes to be analyzed consist of four square (5 mm x 5 mm) silicon structures (Figure A.1) or dies connected in series, and bordered by a molybdenum disc (anode) and a

copper disc (cathode). The four dies of the diode are protected by a white silicone compound [see in Figure 1.15 (b) and (c)].

The doping profile of a single SOS diode die is depicted in Figure 1.10. This profile serves as a reference for validating the measurement to be performed using the SIMS analysis.

A.1.2 Sample preparation

The sample preparation is one of the most critical steps in the SIMS analysis [3]. The sample must be vacuum-compatible, mirror-polished, and flat to perform a reliable measurement. Moreover, the raw sample consisting of four dies with Cu and Mo disks is not directly suitable for the measurement. In addition, each die has a surface area of 0.25 cm^2 and a thickness of about 330 µm which are high sizes for micrometer and, particularly, nanometer scale SIMS instruments. To overcome the limited depth of NanoSIMS, a specific technique has been set up to prepare the sample.

The technique involves making a longitudinal cut through the diode at its center along the axis of the diameter of the disks (Mo or Cu). The obtained cross-section is polished and further analyzed by the instrument. Sample preparation steps include resin embedding, longitudinal cutting, surface polishing, cleaning, and gold deposition, which are described as follows.

First, the white silicone protection is removed [Figure 1.15 (c)], and a plastic holder is machined to maintain the diode. Then, resin embedding is carried out to secure the assembly (Figure A.2).

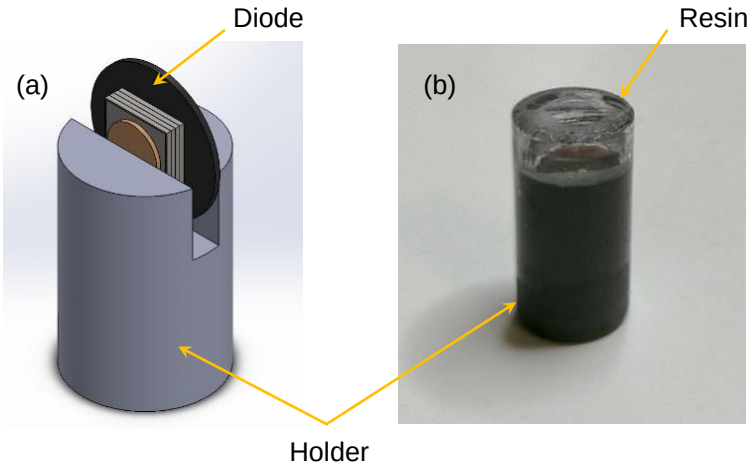

Figure A.2: Illustrations of the sample fixed in its holder: (a) before and (b) after resin embedding.

Once the resin has cured (7–12 hours), the diode is cut using a diamond wire saw 3500 BASE. Further, polishing steps are performed to obtain a mirror-polished surface. Then, an ultrasonic wave bath is used to clean the surface. Figure A.3 shows the results after the cut and polishing. A gold layer of about 50 nm thickness is further deposited on the polished surface to have a conductive surface of the sample.

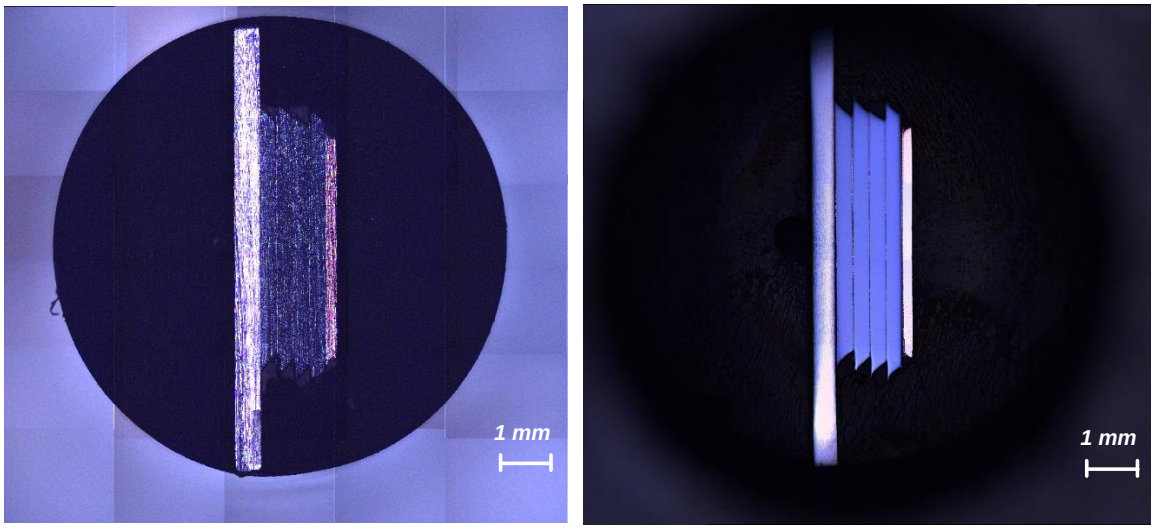

Figure A.3: Pictures of the sample surface: (a) before and (b) after polishing.

A.2 NanoSIMS analysis

A.2.1 Analysis description

NanoSIMS analysis provides access to a chemical map of the surface of a sample with a resolution of up to 50 nm. This technique described in detail in [3] consists of bombarding the surface of the sample located in a high-vacuum (10^{-5}–10^{-10} Torr) chamber with a primary ion beam of energy in the range of hundred of eV to tens of keV. Secondary ions are ejected from the sample surface and are accelerated towards a mass spectrometer, that reveals the elemental or isotopic distribution of the sample surface.

The analyses have been conducted within the Platform "I3" (Inorganic Isotopic Imaging) of the IPREM (Institut des Sciences Analytiques et de Physico-Chimie pour l'Environnement et les Matériaux) of UPPA. The NanoSIMS at IPREM enables obtaining a mapping of the different elements in the sample surface with parallel acquisition of up to seven masses. Figure A.4 depicts the schematic of the CAMECA NanoSIMS 50 L instrument in IPREM.

In this work, the O^- ion source is used to detect the four elements: B (the two isotopes 10B and 11B), Al, Si, and P in five parallel acquisitions. To analyze the elements, a droplet of each of these four elements is placed on a silicon slide and used as a reference (Figure A.5).

A.2.2 Analysis process

To perform the measurement, a line scan sequence is carried out on the sample surface from one electrode to the other (Figure A.6).

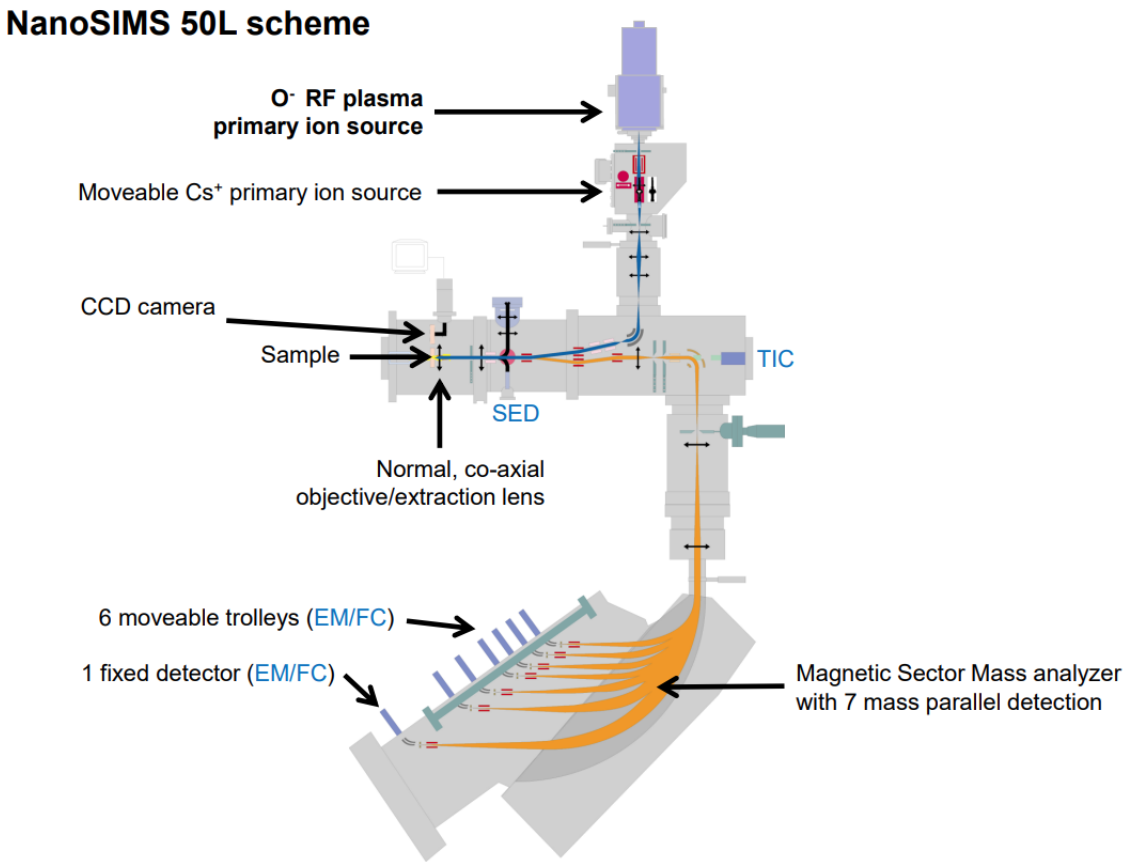

Figure A.4: Schematic of the CAMECA NanoSIMS 50L [4].

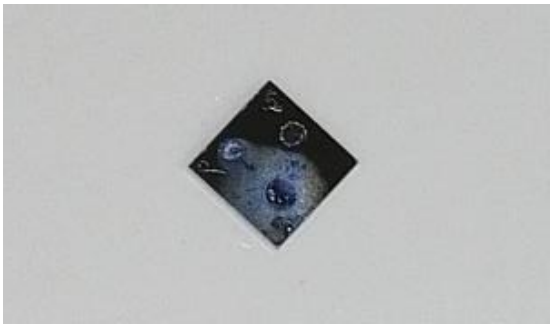

Figure A.5: Silicon slide with droplets of B, Al, and P.

The width of a die can be divided into several pixels of 20x20 µm diameter, for instance. The first measurement region consists of the first pixel on which the primary ion beam is focused to sputter the surface in depth. The secondary ions (of the elements B, Al, P, and Si) ejected from this region are collected and identified at the mass spectrometer. The counts of each element are acquired and processed by the CAMECA software integrated into the instrument giving a pre-map of the region. Several steps of sputtering are conducted to have additional pre-maps (35 pre-maps of depth assumed to be 30 nm each) that are joined together

later in the CAMECA software to form a map of the region.

Subsequently, the focus is shifted to the next pixel to acquire its map. The process continues until the line scan has been completed. Each map depicts the distribution of the elements in the region at a specific depth. It is worth mentioning that before data acquisition, a pre-sputtering step is conducted to clean the surface to avoid contaminated layers.

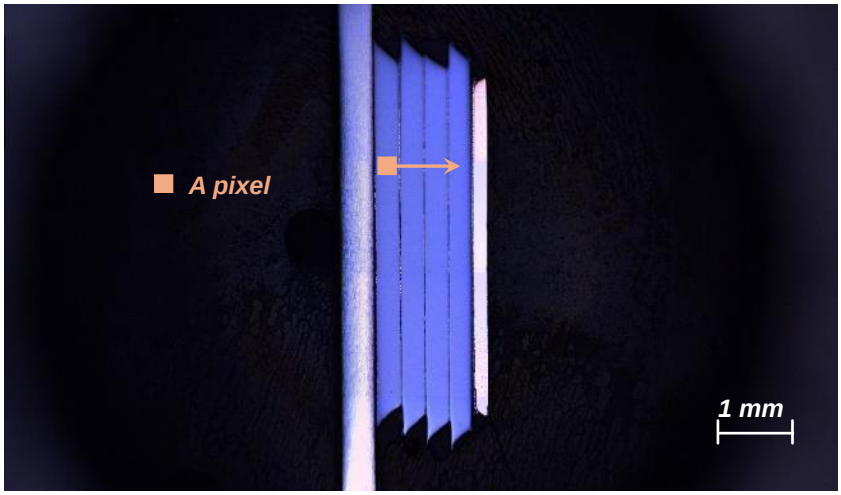

Figure A.6: Line scan sequence representation, showing a pixel and the scan direction.

Thereafter, these maps are numerically processed by the CAMECA software. The pre-maps of the same region are accumulated to increase the total map resolution. Further, a numerical linear scanning is performed to convert the map into numerical quantifiable data enabling to plot the number of elements per unit of distance. After that, the curves of Al, B, and P are normalized to the Si level in Origin software. Figure A.7 shows the simplified steps of the NanoSIMS analysis.

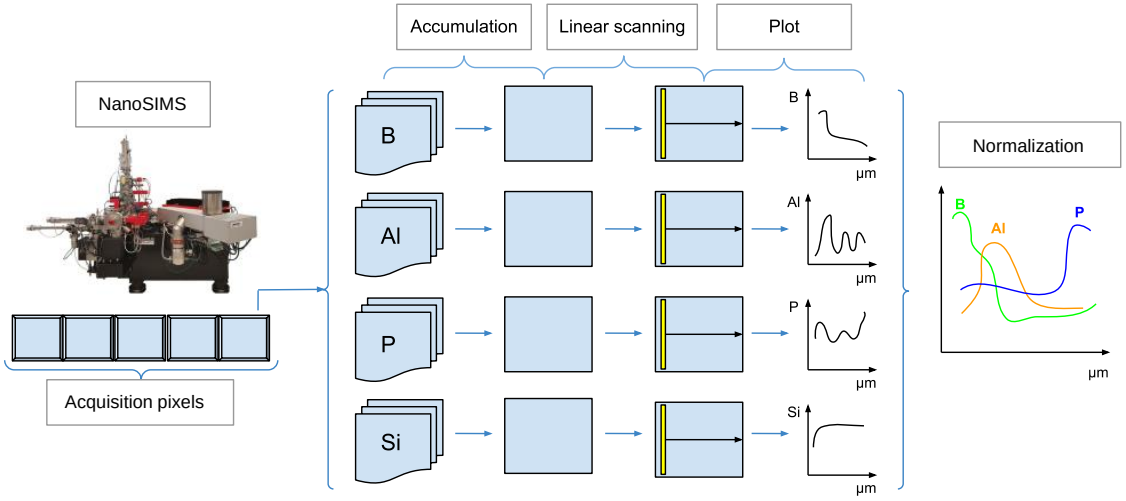

Figure A.7: Simplified diagram of the NanoSIMS analysis process.

Finally, the normalized counts are converted into atom concentrations by multiplying the counts of each element by the density of Si atoms (5 x 10^{22} atoms/cm^3) [5], [6], assuming that the number of counts of Si obtained from the measurement corresponds to this density of Si atoms.

A.2.3 Results and discussion

The acquisition chain for an SOS diode is presented in Figure A.8 showing the different pixels of the line scan. The map of a region is presented in Figure A.9 showing the numerical linear scanning.

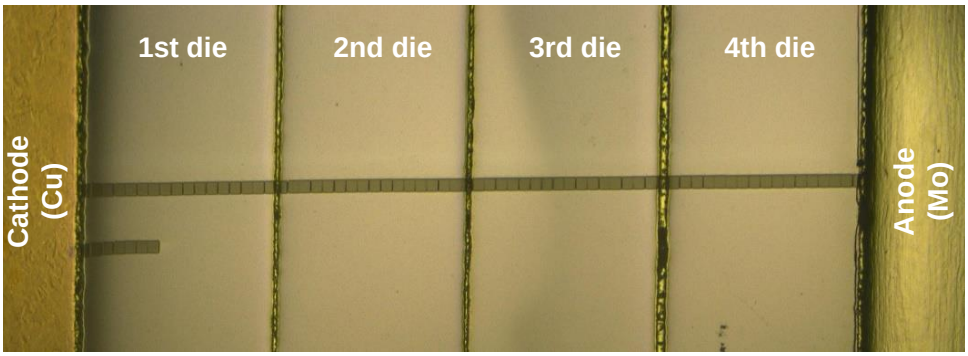

Figure A.8: Picture of the sample showing an acquisition chain.

The measured doping profile plotted from the anode (0 µm) to the cathode (∼330 µm) of an SOS die is shown in Figure A.10. According to the doping profile in Figure A.10, B and Al are prevailing at the anode as expected while P is almost constant in the entire structure, with a little increase at the cathode. The concentrations measured in p^+, p, and n^+ regions are two to three orders of magnitude higher than those found in the literature (Figure 1.10). In addition, the concentration of P atoms in the silicon substrate is measured to be about 10^{20} cm^{-3}. This value is also extremely higher than the literature values of 10^{13} cm^{-3} and 10^{16} cm^{-3}. Such divergences remain unclear and led to the following hypothesis:

- the surface could be contaminated during the polishing phase;
- our conversion method from counts to concentration may not be correct leading to this deviation;
- the brazing alloy used to solder two consecutive dies or between the metallic electrode and the die may influence the results;
- the lower limit of detection of the instrument may be reached, which according to [1] varies with the instrument.

To clarify this divergence, a SIMS analysis is independently carried out. The results are presented in the next section.

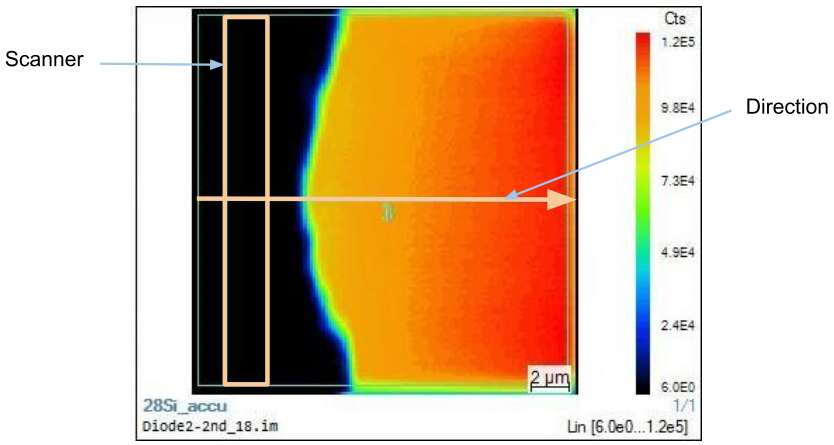

Figure A.9: Illustration of a linear scanning in the CAMECA software.

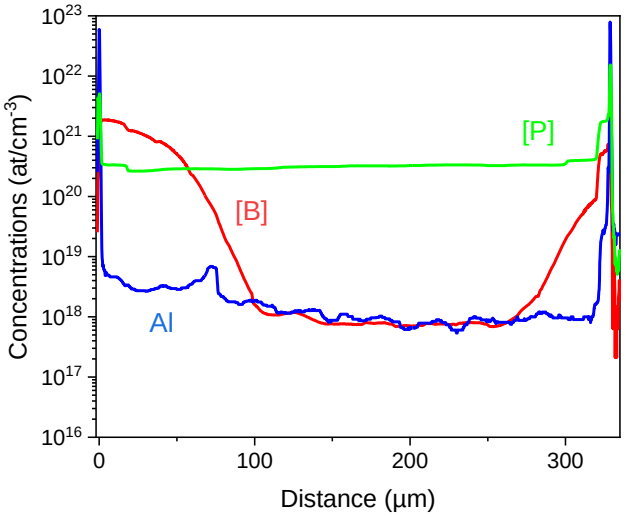

Figure A.10: Measured profile of an SOS diode die using NanoSIMS.

A.3 SIMS analysis

The principle of the SIMS analysis is the same as for the NanoSIMS. An ion source is used to produce the primary ion beam. These primary ions erode the sample surface and produce atomic collisions, some of the collisions resulting in the release of secondary ion particles. These secondary ions are collected by a mass spectrometer, in which their masses are measured for their identification.

The SIMS differs from the NanoSIMS in the spatial resolution which is in the range of micrometers for the SIMS. The SIMS analysis was conducted by the GEMaC (Groupe d'Étude de la Matière Condensée) from Université Paris-Saclay. The analysis is carried out on a sample prepared as described in Section A.1.2. The information presented in this section is based on the report provided by the GEMaC.

For the SIMS experiment, three standard samples of the different elements (Al, B, and P) implanted at high energy in Si are used to quantify the analysis. The standard samples were analyzed under the same conditions as the SOS diode sample. Knowing the implantation doze provided by the implanter and corresponding to the number of atoms introduced in the material, the quantification of the dopants in Si is made possible.

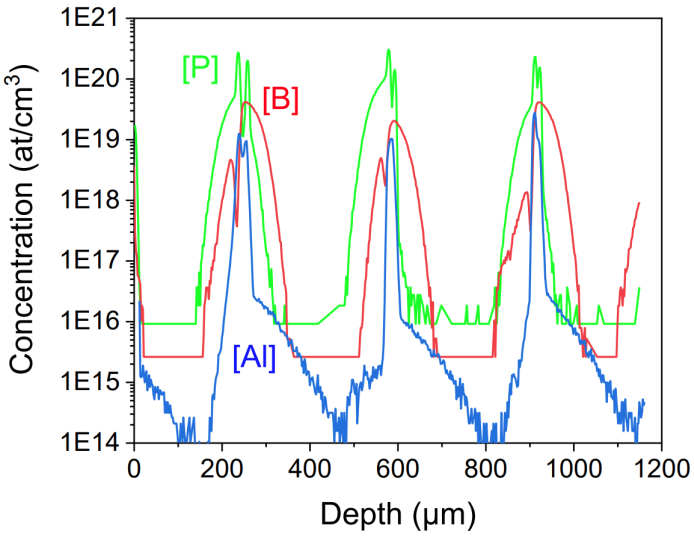

Figure A.11: Quantified profiles of B, Al, and P distributions using SIMS.

The results obtained are presented in Figure A.11 The waveforms show the distribution of Al, B, and P in the four dies connected in series. The first die (from 0 to 250 µm) and the last die (from 910 µm to 1160 µm) are not completely mapped due to defects on the surface near the Cu and Mo junctions (Figure A.12). A picture of the sample after the experiment, showing several SIMS craters of different sizes on the sample surface, is presented in Figure A.12.

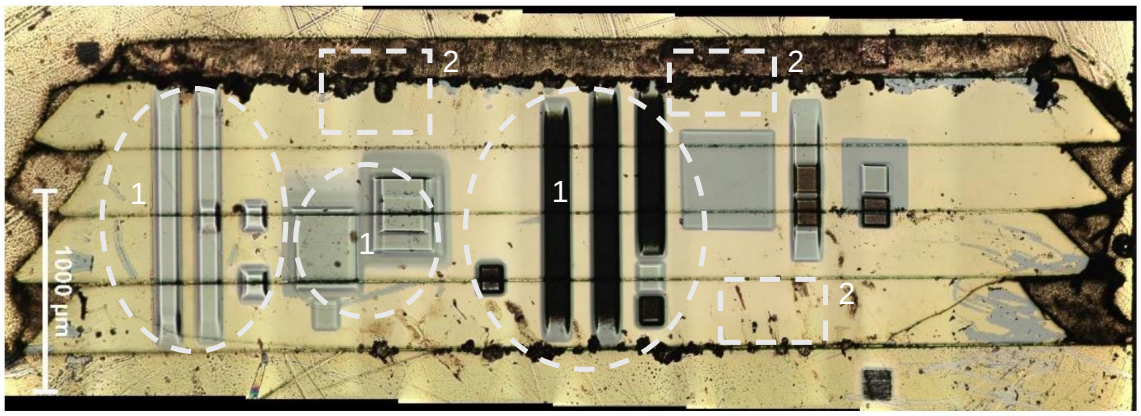

Figure A.12: Picture of the sample surface after SIMS analysis, showing the craters of different sizes and depths (1), and the defects in the sample surface (2).

To facilitate the comparison of the measured doping profile of a die using the SIMS analysis,

the latter is overlaid on the theoretical SOS diode doping profile (Figure A.13).

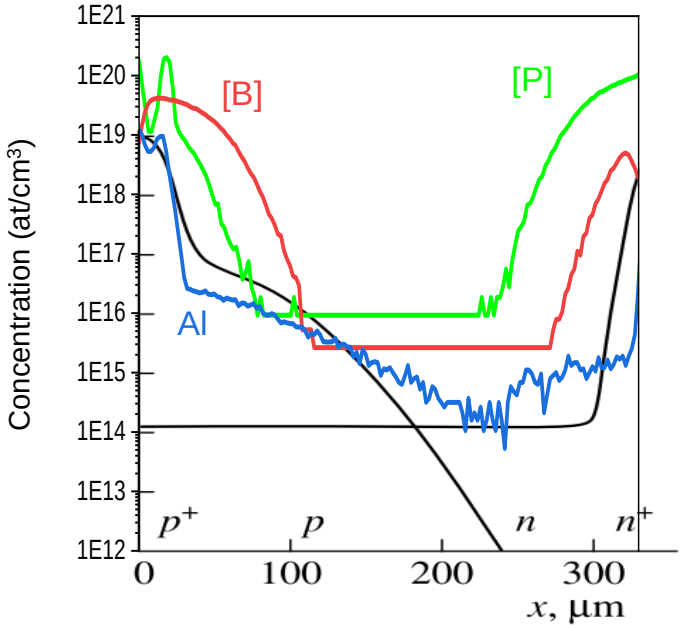

Figure A.13: Measured doping profile (in color) overlaid on theoretical doping profile in black line.

Compared with the NanoSIMS results (Figure A.10), the measured doping profile of Figure A.13 obtained using SIMS appears more consistent with the theoretical profile. The latter shows the dominance of B at the anode and P at the cathode. Additionally, the distribution of Al seems to be in line with the theoretical one at first glance. Nevertheless, the detection limit for these two elements is reached at around 3.5 x 10^{16} cm^{-3} for P and 5 x 10^{15} cm^{-3} for B, therefore measurement below these concentrations is not possible with the instrument used. Moreover, the measured diffusion depths of around 100 µm for B and P dopants (from anode for B and from cathode for P) are greater than expected (around 30 µm according to the theoretical doping profile in Figure 1.10).

However, we note the unexpected presence of elements at opposite electrodes, i.e. B and Al at the cathode, and P at the anode, as previously observed with NanoSIMS. Investigations are currently conducted to better understand these results.

Conclusion

NanoSIMS and SIMS analysis have been conducted on SOS diodes to determine their doping profile. The dopants Al, B, and P are detected along the silicon device in proportions sometimes exceeding the theoretical concentrations. The instrument limit of detection probably prevents full measurement of the profile using the SIMS analysis. This could be a reason for the high concentrations obtained using NanoSIMS, together with the probably non-adapted conversion method used. Following discussions with experts in the field, the probability of contamination

during the polishing process is negligible and is therefore not the cause of the discrepancies in results observed. In addition, it would be more accurate to carry out the measurement directly on a single die to avoid contamination with the alloy elements used to solder the dies together. Although still open to questions, these methods in a nutshell seem promising for identifying the doping profile of diodes.

References

[1] "F1617–98. Standard Test Method for Measuring Surface Sodium, Aluminum, Potassium, and Iron on Silicon and EPI Substrates by Secondary Ion Mass Spectrometry," American Society for Testing and Materials, 100 Barr Harbor Dr., West Conshohocken, PA 19428, Standard, 1995.

[2] N. H. Krishnan, V. K. Yadav, N. Anandarao, *et al.*, "Control of switching characteristics of silicon-based semiconductor diode using high energy linear accelerator," *Journal of Nano- and Electronic Physics*, vol. 5, no. 2, pp. 4–7, 2013, ISSN: 20776772.

[3] J. Nuñez, R. Renslow, J. B. Cliff, and C. R. Anderton, "NanoSIMS for biological applications: Current practices and analyses," *Biointerphases*, vol. 13, no. 3, 2018, ISSN: 1934-8630. DOI: 10.1116/1.4993628.

[4] D. Schaumlöffel, J. Malherbe, É. Gontier, F. Hillion, F. Horréard, and D. Dobritzsch, "A RF plasma oxygen ion source on NanoSIMS for subcellular trace element detection," 2017, The 7th International NanoSIMS user meeting "NanoSIMS & correlative microscopy: exploring physical and biochemical boundaries" Leipzig, Germany, 22-24th of August. [Online]. Available: https://www.ufz.de/export/data/2/152232_NanoSIMS%20Leipzig%20D_Schaumloeffel.pdf.

[5] S. M. Sze and K. K. Ng, *Physics of Semiconductor Devices*. Wiley, Oct. 2006, ISBN: 9780471143239. DOI: 10.1002/0470068329.

[6] S. K. GHANDHI, *VLSI Fabrication principles: Silicon and gallium arsenide*. Newyork: John Wiley & Sons, 1995, pp. 87–88, ISBN: 0-471-58005-8. [Online]. Available: https://banavathvalyaiitmadras.wordpress.com/wp-content/uploads/2015/12/vlsi-fabrication-principles-silicon-and-gallium-arsenide-1994-ghandi-wiley-2e.pdf.

Appendix B

Worldwide recognition

Chapter B

Worldwide recognition

B.1 Journal publications

1. **M. R. Degnon**, A. I. Gusev, A. Silvestre de Ferron, L. Pécastaing, A. Piaser, F. Bayol, and B. M. Novac, *"A 500-kV Nanosecond Pulse Generator Based on an Off-the-Shelf Solid-State Opening Switch,"* accepted in May 2024, for inclusion in a future issue of IEEE Transactions on Plasma Science, DOI: 10.1109/TPS.2024.3403379.

2. **M. R. Degnon**, A. I. Gusev, A. Silvestre de Ferron, L. Pécastaing, A. Baranov, C. Mielot, S. Boisne, M. J. Barnes, V. Senaj, T. Kramer, and B. M. Novac, *"A Saturable Pulse Transformer Based on Nanocrystalline Magnetic Cores for an Adjustable Nanosecond High-Voltage Generator,"* in IEEE Transactions on Plasma Science, vol. 51, no. 10, pp. 2849-2857, Oct. 2023, DOI: 10.1109/TPS.2023.3284657.

3. **M. R. Degnon**, A. I. Gusev, A. Silvestre de Ferron, L. Pécastaing, G. Daulhac, A. Baranov, S. Boisne, and B. M. Novac, *"Off-the-Shelf Diodes as High-Voltage Opening Switches,"* in IEEE Transactions on Plasma Science, vol. 50, no. 10, pp. 3384-3392, Oct. 2022, DOI: 10.1109/TPS.2022.3177702.

B.2 Conferences

1. **M. R. Degnon**, A. I. Gusev, A. Silvestre de Ferron, L. Pécastaing, A. Baranov, C. Mielot, S. Boisne, and B. M. Novac, *"A Comparative Study of Rectifier Diodes in Opening Switch Mode for High-Voltage Nanosecond Pulsed Power System,"* ***Invited talk***, 4th IEEE International Pulsed Power Conference (PPC), Jun 2023, San Antonio, Texas, United States. ⟨hal-04071213⟩

2. **M. R. Degnon**, A. I. Gusev, A. Silvestre de Ferron, L. Pécastaing, A. Baranov, C. Mielot, S. Boisne, B. M. Novac, M. J. Barnes, V. Senaj, and T. Kramer, *"A Saturable Pulse Transformer based on Nanocrystalline Magnetic Cores for an Adjustable High-Voltage Nanosecond Generator,"* ***Oral***, 9th Euro-Asian Pulsed Power Conference (EAPPC), Sep 2022, Seoul, South Korea. ⟨hal-03666200⟩

3. **M. R. Degnon**, A. I. Gusev, A. Silvestre de Ferron, L. Pécastaing, B. M. Novac, G. Daulhac, A. Baranov, S. Boisne, M. J. Barnes, V. Senaj, and T. Kramer, "*Standard Semiconductor Diodes as High-Voltage Opening Switches,"* ***Oral***, IEEE Pulsed Power conference and Symposium on Fusion Engineering (PPC/SOFE), Online, Dec 2021, Denver, Colorado, United States. ⟨hal-03478182⟩

4. **M. R. Degnon**, A. I. Gusev, A. Silvestre de Ferron, L. Pécastaing, G. Daulhac, A. Baranov, S. Boisne, and B. M. Novac, "*A Semiconductor Opening Switch Based on Off-The-Shelf Components,*" ***Oral***, 8th Euro-Asian Pulsed Power Conference (EAPPC), Sep 2021, Biarritz, France. ⟨hal-03469276⟩

5. **M. R. Degnon**, A. I. Gusev, A. Silvestre de Ferron, L. Pécastaing, B. M. Novac, G. Daulhac, A. Baranov, S. Boisne, M. J. Barnes, V. Senaj, and T. Kramer, "*Nanocrystalline Magnetic Cores Under Fast Pulse Magnetization,*" ***Poster***, 8th Euro-Asian Pulsed Power Conference (EAPPC), Sep 2021, Biarritz, France. ⟨hal-03469300⟩

B.3 Workshops

1. **M. R. Degnon**, A. I. Gusev, A. Silvestre de Ferron, L. Pécastaing, A. Piaser, F. Bayol, and B. M. Novac, *"500 kV Pulsed Power Generator Based on a Saturable Pulse Transformer and Off-the-Shelf Semiconductor Opening Switch,"* ***Oral***, ISP workshop on Pulsed Power Technology and Applications, Feb 2024, Hamburg (DESY), Germany. ⟨hal-04494597⟩

2. **M. R. Degnon**, A. I. Gusev, A. Silvestre de Ferron, L. Pécastaing, A. Piaser, F. Bayol, and B. M. Novac, *"Générateur de Puissance Pulsée basé sur un Transformateur Impulsionnel Saturable et un Commutateur Semi-Conducteur à Ouverture,"* ***Oral***, Premières Journées HPP, CEA – Centre de Gramat, Feb 2024, Gramat, France. ⟨hal-04494661⟩

3. **M. R. Degnon**, A. I. Gusev, A. Silvestre de Ferron, L. Pécastaing, A. Baranov, C. Mielot, S. Boisne, B. M. Novac, M. J. Barnes, V. Senaj, and T. Kramer, "*A Saturable Pulse Transformer as a Magnetic Switch for an Adjustable SOS Generator,*" ***Oral***, ISP workshop on Pulsed Power Technology and Applications, Apr 2023, GSI, Darmstadt, Germany. ⟨hal-04071311⟩

4. **M. R. Degnon**, A. I. Gusev, A. Silvestre de Ferron, L. Pécastaing, G. Daulhac, A. Baranov, S. Boisne, B. M. Novac, M. J. Barnes, V. Senaj, and T. Kramer, "*Investigation of Semiconductor Diodes as High-Voltage Opening Switches for a Nanosecond High-Voltage Generator,*" ***Oral***, 3rd ISP PhD Workshop - French-German Research Institute, Nov 2022, Saint-Louis, France. ⟨hal-04403861⟩

5. **M. R. Degnon**, A. I. Gusev, A. Silvestre de Ferron, L. Pécastaing, B. M. Novac, G. Daulhac, A. Baranov, S. Boisne, M. J. Barnes, V. Senaj, and T. Kramer, "*Standard Semiconductor Diodes as High Voltage Opening Switches,*" ***Oral***, ISP Workshop on Pulsed Power Technology and Applications, Mar 2022, ITER, Saint-Paul-Lez-Durance, France. ⟨hal-03666172⟩

B.4 Awards

1. *"Prix de la meilleure présentation orale"* during the « Premières Journées HPP », CEA – Centre de Gramat, Feb 2024, Gramat, France.
2. *"The Best Poster Prize"* during the UNIZAR-UPPA cross-border doctorials, Oct 2022, Jaca, Spain.
3. *"EAPPC Outstanding Young Researcher Award"* for contribution in the research on « A Semiconductor Opening Switch Based on Off-The-Shelf Components », Sept 2021, Biarritz, France.

ITOPP

ALCEN

Contacts :

https://siame.univ-pau.fr/

https://www.itopp-alcen.com